Master Thesis

Development of MDT Muon Trigger with Associative Memory for the ATLAS experiment at HL-LHC

Department of Physics, Tokyo Institute of Technology

Yunjian He

Professor Masahiro Kuze

February 7, 2020

Abstract

Nowadays, the known elementary particles and the fundamental interactions between the particles are well described by the Standard Model of particle physics. The discovery of Higgs boson by the ATLAS experiment and the CMS experiment at the Large Hadron Collider (LHC) at CERN marks the completion of the Standard Model. However, phenomena that can not be explained by the Standard Model indicate the existence of new physics beyond the Standard Model. Therefore, to search for the evidence of new physics such as Super Symmetry (SUSY), the LHC continues to collide protons to acquire data. At the ATLAS experiment, it is impossible to record all the data of collision at a reasonable cost with the current technology. So a multiple level trigger system is used to select collision events that are related to the interesting physic processes. The muon trigger system is used for triggering the events with physics processes that have muons in the final state.

Since the cross-sections of the new physics processes are expected to be very small, a large amount of data is needed for the search of new physics. To get the large statistic of data, CERN plans to upgrade the LHC to the High-Luminosity LHC (HL-LHC). The upgrade installation and commissioning will start from the year 2024 and finish in the year 2026. After the upgrade, the increase of luminosity will result in more particles produced in the proton-proton collision and makes the trigger system hard to select events related to target physics processes. Hence the ATLAS experiment will also upgrade the detectors and TDAQ system to adapt the high luminosity environment. For the muon trigger system, the whole system will be redesigned, and especially for the hardware-based triggers, the introduction of a new muon trigger using the information from the Monitored Drift Tube (MDT) detectors is proposed. The MDT detector is possible to provide more precise information of partial muon trajectory than the detectors used for the current hardware-based trigger. With the information from the MDT detectors, more accurate selection can be achieved, and a reduction of total trigger rate is expected.

The ATLAS Japan group proposed to realise the MDT muon trigger with the Associative Memory (AM). AM is a special memory that can quickly match the input data with the prestored patterns. The AM-MDT muon trigger uses AMChips to reconstruct the partial muon trajectory and then calculates parameters that are correlated with the muon momentum for the selection of muons. Finally, a trigger decision and an estimated momentum of muon will be given by the AM-MDT muon trigger.

The purpose of this research is to develop the algorithm of the AM-MDT muon trigger that can be used online and estimate the performance of the developed algorithm. We developed and implemented all the algorithm of the subsequent steps after the pattern matching in the AMChips. With the developed algorithm, we performed a full chain software-based emulation for the AM-MDT muon trigger and estimated the performance with Monte Carlo test samples and real data samples taken in the ATLAS Run 2. The results of the performance tests show that in the case of p_{T} thresholds of 20 (10) GeV the AM-MDT muon trigger can achieve the trigger rate reduction of 51.3 (40.0)% while maintaining a 97.2 (95.4)% acquisition efficiency of muons with p_{T} larger than 20 (10) GeV, in the barrel region of the ATLAS detector. The AM-MDT muon trigger also provides robustness against the high-luminosity environment.

Contents

Chapter 1

Introduction

1.1 Physical Backgrounds

1.1.1 Standard Model of Particle Physics

Particle Physics, stared at the end of the 19th century when J.J Thomson discovered the electron,the first subatomic particle [1], and has been significantly developed in the past years. Today, all the known elementary particles and the fundamental interactions between them, except the gravity, are well described by the Standard Model of Particle Physics.

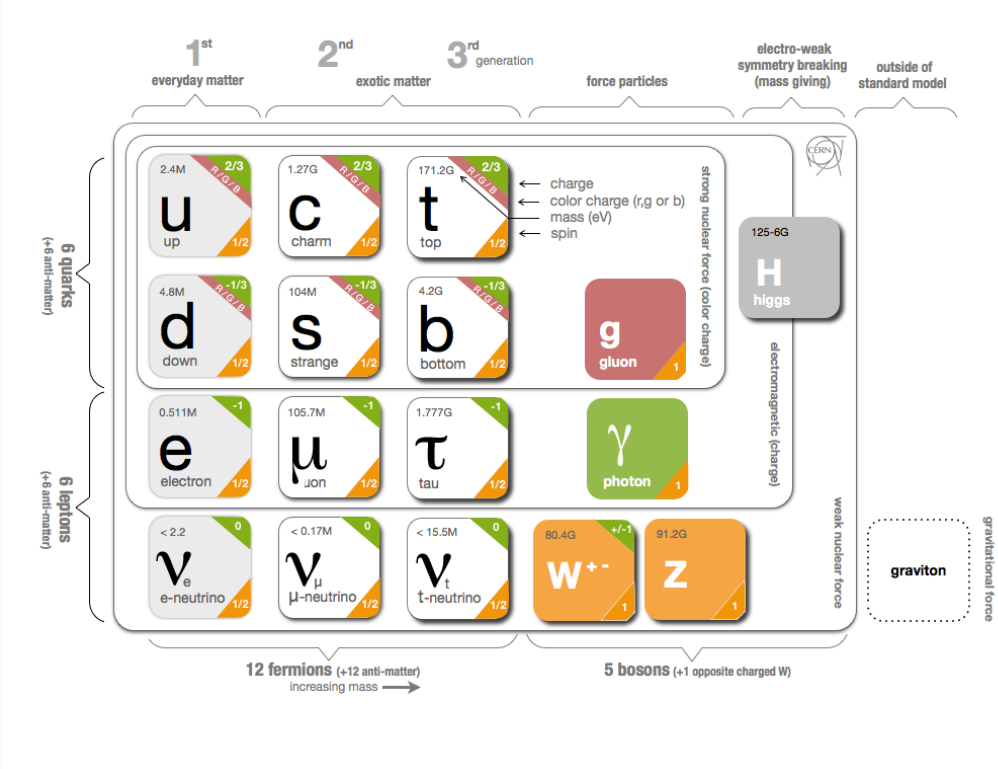

Fig. 1.1 Elementary particles described by the Standard Model of Particle Physics and the basic information of the particles. Graviton is also shown outside of the frame of the Standard Model [2].

All the elementary particles described by the Standard Model are shown in Fig. 1.1 with the basic information of particle name, mass, electric charge, colour charge and spin. All of these particles can be classified into two groups by their spin. The particles with a half-integer

spin $\frac{1}{2}$, are fermions, that follow the Fermi-Dirac statistics. The other particles with integer spin 1 or 0 are bosons, that follow the Bose-Einstein statistics. For all fermions, corresponding anti-particles exist. The anti-particles have opposite charge but same mass and spin with their corresponding normal particles. When particles and anti-particles meet each other, annihilation between the particles will happen and all the masses are transformed to pure energy with the famous equation $E = mc^2$.

The 12 elementary fermions form the normal matter in the universe. The elementary fermions can be further classified as quarks and leptons. The quarks interact through the strong interaction but the leptons do not.

Two types of quarks exist. The up-type quarks have a non-integer electric charge of $+\frac{2}{3}$ that include the up (u) quark, the charm (c) quark, and the top (t) quark. The electric charge of down-type quark is $-\frac{1}{3}$ and the down-type quarks include the down (d) quark, the strange (s) quark, and the bottom (b) quark. The quarks interact through all the fundamental interactions. In the case of the strong interaction, the quarks have colour charges Red, Green and Blue and interact by exchanging colour charges carried by the gluons.

The leptons include charged leptons and neutrinos. The charged leptons have electric charge -1 and interact through both electromagnetic interaction and weak interaction. The neutrinos have no electric charge and interact through the weak interaction only. In the Standard Model, the masses of neutrinos were considered to be exactly zero, but the neutrino oscillations [3–5] indicate that the neutrinos have very small non-zero masses.

Another method classifies the elementary fermions into three generations. Each generation contains an up-type quark, a down-type quark, a charged-lepton and a neutrino. The particles in the same position in each generation have similar properties with each other but different in mass. Massive particles decay into lighter particles through the weak interaction. The particles in the first generation are stable.

The elementary bosons include the gauge bosons that carry the fundamental interactions and the Higgs boson corresponding to the Higgs field that gives masses to other particles.

The electromagnetism is described by the quantum electrodynamic (QED) which is the relativistic quantum field theory version of the classic electrodynamics. The electrodynamic interaction propagates by exchanging photons (γ) between the electrically charged particles. The photon is massless which means the electromagnetic force can propagate to infinity.

The strong interaction is described by the quantum chromodynamics (QCD) and carried by the gluon (g). The gluons are massless and can be described as a combination of a colour charge and an anti-colour charge. According to the QCD, only colourless states can be observed. Therefore, the quarks are bound by the gluons to form colourless hadrons. If the distance between two quarks become too long, the gluons break to form new hadrons since it is more favourable in total energy. This makes the strong interaction propagate a very short range.

The weak interaction is described by the electroweak theory which is also known as the Glashow-Weinberg-Salam theory. The theory unified the electromagnetic interaction and the weak interaction. The two interactions are separated in the spontaneous electroweak symmetry break with the Higgs mechanism. Before the symmetry breaking, four types of massless gauge bosons B^0, W^0, W^+ and W^- exist to carry the electroweak interaction. When the symmetry breaking happens, the bosons get masses and a mix between the B^0 and W^0 results in the Z boson and the photon.

The Higgs field is a complex doublet scalar field with two charged components and two neutral components. At the beginning of the universe, the ground state of the Higgs field was at the origin. As the temperature of the universe decreases, the potential shape of the Higgs field changed to the shape shown in Fig. 1.2. Due to the Mexican hat shape, the ground state shifted from the origin to points that have non-zero expectation value with arbitrary phase. The Higgs field is approaching to its ground state. Then three components of the Higgs field are absorbed by the Z boson and $W^{\pm}$ bosons, and the perturbation of the remaining component manifests as

the Higgs boson observed in the Standard Model. The Higgs field with a non-zero expectation value also generates a mass term via the Yukawa coupling between the fermions and the Higgs field. As a result, the masses of the elementary particles are given by the Higgs field.

In 2012, the ATLAS Collaboration and the CMS Collaboration at CERN announced that they had observed a new boson which is very like the Higgs boson [6,7]. The following measurements of the properties of the new boson confirmed that it is the Higgs boson predicted by the Standard Model [8]. This discovery marks the completion of the Standard Model of Particle Physics.

However, only 5% of the universe can be described by the Standard Model, and the remaining 95% is dark matter and dark energy [9]. The presence of dark matter and dark energy, and other phenomena that cannot be explained by the Standard Model such as the origin of neutrino masses, the asymmetry between matter and antimatter, and the hierarchy problem between the mass of Higgs boson and the Planck mass scale, clearly indicate that new physics beyond the Standard Model (BSM) exists.

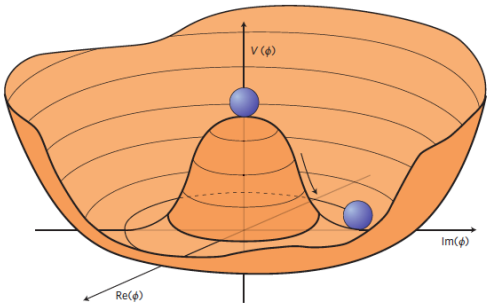

Fig. 1.2 The shape of Higgs potential in the Standard Model. When the state comes to the ground state, the rotational symmetry of the state will spontaneously break. The choice of the point at the bottom of the potential is arbitrary [10].

1.1.2 Search for Physics Beyond the Standard Model

To find answers to the unexplained questions, theorists proposed many new physics models. A popular model that can solve the hierarchy problem and give an explanation of the existence of dark matter is the Supersymmetry Models (SUSY) [11–17]. In the Supersymmetry Model, a new symmetry called R-parity is introduced [18]. The R-parity is the symmetry between boson and fermion, defined as $R = (-1)^{3(B-L)+2s}$, where B is the Baryon number, L is the Lepton number and s is the spin of the particle. It is considered that every elementary fermion has a boson partner and every elementary boson has a fermion partner. The Standard Model particles have R-parity $+1$, and the SUSY particles have R-parity -1.

In the SUSY models, two complex doublets Higgs fields are considered instead of one. One of the Higgs field gives mass to the up-type quarks and neutrinos, and the other one gives mass to the down-type quarks and charged leptons. The extension allows the existence of 5 types of Higgs bosons (H^+, H^-, h, A, H^0) at the normal particle side. The Higgs boson observed in 2012 is the lightest and neutral one h.

The supersymmetric partners of the Standard particles are only different in spin and mass and the same in other properties like electric charge and colour charge. The bosonic SUSY partners of the elementary fermions are scalar bosons called sfermions that can also be classified as squarks $\tilde{q}$ and sleptons $\tilde{l}$. The fermionic SUSY partners of the elementary bosons have spin $\frac{1}{2}$, including gauginos and higgsinos. There gauginos includes gluino $\tilde{g}$ corresponding to the gluon, 3 winos $\tilde{W}^+, \tilde{W}^-, \tilde{W}^0$ and 1 bino $\tilde{B}^0$ corresponding to the electroweak bosons. With the electroweak symmetry breaking, the winos and bino will mix and make supersymmetric partners

of photon and weak bosons. Due to the limit of degrees of freedom, 4 types of higgsinos are predicted, two of them are electrically charged $\tilde{H}^+, \tilde{H}^-$ and the other two are electrically neutral $\tilde{H}_1^0, \tilde{H}_2^0$. Furthermore, the gauginos and higgsinos can mix with each other to form new mass eigenstates. The charged winos and charged higgsinos mix to form charginos $\tilde{\chi}_1^+, \tilde{\chi}_1^-, \tilde{\chi}_2^+, \tilde{\chi}_2^-$, and the neutral wino, the bino and the neutral higgsinos mix to form neutralinos $\tilde{\chi}_1^0, \tilde{\chi}_2^0, \tilde{\chi}_3^0, \tilde{\chi}_4^0$.

If the R-parity is conserved, the SUSY particles must be produced in pair and the Lightest Supersymmetry Particle (LSP) will be stable. In many SUSY models, LSP is considered to be the lightest neutralino $\tilde{\chi}_1^0$ as a good candidate of WIMP dark matter [19, 20]. In the R-parity non-conserved models, the SUSY particles will finally decay into the Standard Model particles. By these R-violating models, the baryon asymmetry in the universe can be explained and the mystery of the non-zero neutrino mass can be solved by introducing lepton number violating couplings [21, 22].

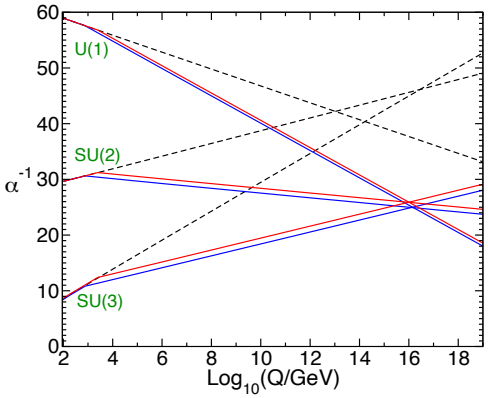

Fig. 1.3 Evolution of the inversed gauge coupling α^{-1} as a function of Q-value. The dashed line shows the prediction of the Standard Model. The solid lines are predictions of the Supersymmetry Model with different parameter settings. The electromagnetic force, the weak force and the strong force unify at one point with the supersymmetry [17]

Moreover, with the extension of SUSY particles, the strong interaction, the weak interaction and the electromagnetic interaction will be unified at one point at an energy scale of 10^{16} GeV as shown in Fig. 1.3. The search for SUSY will give hints of a grand unified theory (GUT) or even superstring models.

Therefore, the search for SUSY particles is very important and the results of SUSY search indicate the future direction of Particle Physics. At CERN, the ATLAS experiment and the CMS experiment continue to search for evidence of SUSY particles with the Large Hadron Collider (LHC). However, no SUSY particle is observed up to the present, and the lower limits of SUSY particles is measured from hundreds of GeV to 2.4 TeV [23]. To finally observe SUSY particles, we need more accurate measurements, larger statistics of data, and higher collision energy. The improvements in all degrees including the collider, the detectors and the analysis methods are necessary. Thus CERN plans to upgrade the LHC to High-Luminosity LHC with a centre-of-mass energy of 14 TeV to search SUSY and other new physics. Simultaneously the Phase-II upgrade of the ATLAS experiment will ensure that the detectors can work at the high luminosity environment with an excellent sensitivity to the new physics phenomena.

1.2 Requirements on the MDT Muon Trigger

As described in the previous section, high sensitivity and accuracy are required for the new physics search. This thesis describes the development of a new muon trigger system using the

Monitored Drift Tube (MDT) at the ATLAS experiment. The muon trigger system identifies and selects muons produced in the final states of collisions and then gives a decision whether the collision contains interested physical processes or not.

Since the protons are accelerated in large groups called bunches, several pairs of protons collide each other in one bunch crossing. With the increase of the luminosity of the LHC, more collisions happen in one bunch crossing. In the ATLAS Run 2, 33.7 collisions happen per crossing on average [24]. As the cross sections of new physics processes are very small, larger number of collisions in one bunch crossing means higher probability of new physics phenomena. Generally only up to one collision in the bunch crossing is related to the physical processes we are interested in. The accompanying collisions are called pileups and produce particles unrelated to the target physics processes. In the high luminosity environment after the upgrade of the LHC, the number of pileups is expected to increase up to 200 which makes the trigger system hard to select events related to the new physics.

As shown in Fig. 1.4, according to the Technical Design Report (TDR) for the Phase-II upgrade of the ATLAS Trigger and Data Acquisition System [25], higher thresholds must be applied in the current lepton trigger systems to maintain the trigger rate in a reasonable range. However, the no upgrade scenario is not acceptable for SUSY search, such as the compressed SUSY models. The compressed SUSY model has compressed mass spectrum with small mass difference between the LSP and heavier SUSY particles. The small mass difference means the muons produced in the decay chain will have small transverse momentum p_T and the increased p_{T} thresholds inevitably discards the muons and results in a low acceptance.

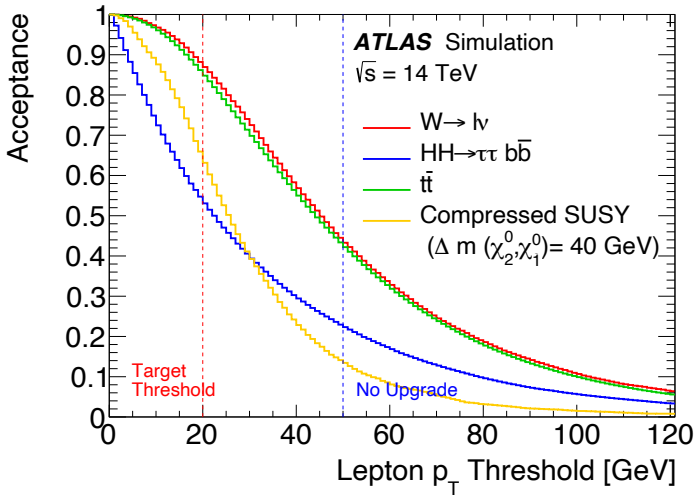

Fig. 1.4 Transverse momentum dependency of the acceptance to target physical processes in the ATLAS experiment at HL-LHC [25]. For the HH→ $\tau\tau bb$ process, at least one τ decays into e or μ, and for the $t\bar{t}$ production process, the semi-leptonic channel is considered. The Compressed SUSY model is using Well-tempered Neutralino which is designed to be consistent with the dark matter relic density [26].

Therefore, the muon trigger system of the ATLAS experiment at HL-LHC should have an ability to reject a large number of fake muons in the low momentum region while keeping a high momentum resolution to give correct trigger decision. In order to fulfil these requirements, introduction of a new muon trigger using information from the MDT is proposed. From the results of rate estimation studies shown in Fig. 1.5, additional rate reductions of approximately 55% and 70% events for transverse momentum (p_{T}) thresholds 10 GeV and 20 GeV can be achieved by introducing MDT muon trigger under the high-luminosity environment after the upgrade of current muon trigger. The estimation was conducted using Monte Carlo simulation

and the algorithm of the MDT muon trigger was implemented in a different method [27].

We use these numbers as the reference values of the MDT muon trigger performance. The MDT muon trigger needs to achieve a trigger rate reduction as high as possible while maintaining a high acquisition efficiency for muons with p_{T} larger than the p_{T} threshold.

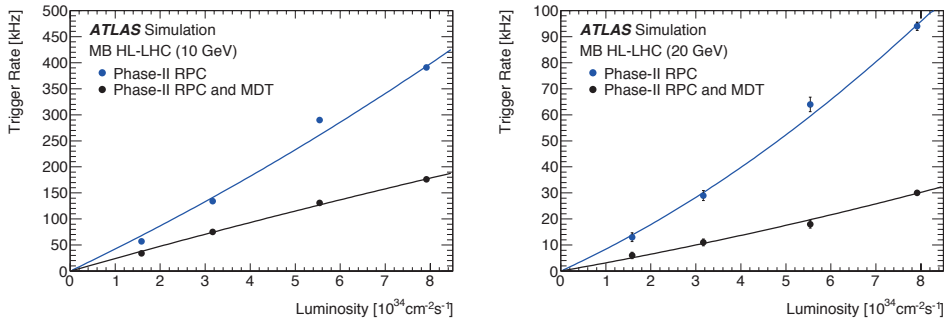

(a) (b)

Fig. 1.5 Estimated rates of the muon trigger system of the ATLAS in the "Barrel" part with and without the MDT muon trigger for p_{T} thresholds 10 GeV(a) and 20 GeV(b) under the high luminosity environment [25]. The solid lines are the second ordered polynomial fit results of the data points. The results are achieved using Monte Carlo simulation of proton-proton collisions at a centre-of-mass energy of 14 TeV with a 25 ns bunch crossing.

1.3 Previous Researches

Before this research, the performance of the MDT muon trigger has been investigated with several simulation samples and datasets. A study [28] showed that high precision information from the MDT evidently increases the sensitivity of the first level muon trigger with ATLAS Run 1 data taken in 2012 with a centre-of-mass energy of $\sqrt{s} = 8$ TeV and bunch spacing of 25 ns. The results are similar to the expected performance of the TDR that requires a 70% rate reduction in the whole ATLAS muon spectrometer region for p_{T} threshold 20 GeV while maintaining a 95% acquisition efficiency for muons with p_{T} larger than the p_{T} threshold. It also proposed an algorithm of fast track reconstruction for the MDT.

Then other studies [29, 30] redid the study with ATLAS Run 2 data taken in 2016 with $\sqrt{s} = 13$ TeV and bunch spacing of 25 ns. The results show that the rate reduction is only about 45% when the acquisition efficiency maintaining 95% with respect to the ATLAS Run 2 level-1 trigger system for p_{T} threshold 20 GeV. The difference between the results are mainly caused by the improvement of the muon trigger system before the start of Run 2. On the other hand, we found that the spatial resolution of MDT is better than expected in the results using the Run 2 data. For this reason, the performance of the MDT muon trigger is possibly underestimated, and the target performance would be still achievable.

This thesis is organised as follows. Chapter 2 describes the LHC and the ATLAS detector, also with the upgrade plans. The concepts of the MDT muon trigger with associative memory are described in Chapter 3. The results of the performance tests of the MDT muon trigger based on software emulation with Monte Carlo samples and ATLAS Run 2 data are shown in Chapter 4 and Chapter 5, respectively. The conclusions and outlook are given in Chapter 6.

Chapter 2

The LHC and the ATLAS Detector

2.1 The Large Hadron Collider

2.1.1 Overview of the Large Hadron Collider

The Large Hadron Collider (LHC), located at the border of France and Switzerland near the city of Geneva, is the largest proton-proton collider in the world. The centre-of-mass energy in proton-proton collision is 13 TeV in the Run 2 operation, which is also the highest collision energy the human beings have achieved so far.

The main machine body of the LHC is installed in a 27 km long 100 m deep tunnel, as part of the CERN accelerator complex. In Fig. 2.1, the whole CERN accelerator complex is shown. For proton-proton collision experiments at the LHC, the beam starts at the LINAC2 (LINear ACcelerator) until Run 2, which will be replaced by the LINAC4 from Run 3. The LINAC can accelerate protons, made by ionising hydrogen gas, to the energy of 50 MeV. Then the BOOSTER (Proton Synchrotron Booster) accelerating the protons to 1.4 GeV, followed by the PS (Proton Synchrotron) accelerates the protons to 25 GeV. The 25 GeV protons are injected to the SPS (Super Proton Synchrotron), which led to the discovery of the weak bosons, and then accelerated to 450 GeV. Finally, the protons are accelerated to 6.5 TeV in the LHC.

The LHC contains two vacuum beam pipes covered by superconducting magnets and cryogenic devices. The proton beams travel in opposite directions in the two beam pipes and form groups called proton bunch during the accelerating process. Each proton bunch contains about 10^{11} protons, and an interval of 25 ns is set between every two bunches in the LHC.

The two proton beams only cross with each other at the four interaction points (IP) of the LHC. At each IP, big detectors are installed for experiments with various physical motivations. Four big experiments at the LHC are the ATLAS (A Toroidal LHC ApparatuS) experiment, the ALICE (A Large Ion Collider Experiment), the CMS (Compact Muon Spectrometer) experiment and the LHCb (Large Hadron Collider beauty) experiment. The ATLAS experiment and the CMS experiment are experiments for general purposes, while the ALICE is focusing on heavy ion collision and the LHCb experiment is specialised in flavour physics of the bottom quark.

2.1.2 The High-Luminosity Large Hadron Collider

In order to meet the demands of a more significant data for new physics search, a plan to upgrade the LHC was approved. Since the main difference between the upgraded collider and the present LHC is the increase of peak luminosity, the upgraded collider is named the High-Luminosity Large Hadron Collider (HL-LHC). Fig. 2.2 shows the plan of LHC and HL-LHC. The LHC started physics run in 2010 and now the LHC is in the Long Shutdown 2 (LS2) for the Phase-I upgrade of the experiments. In 2021, Run 3 of the LHC will start and from 2024, the LS3 for the upgrade work of HL-LHC will take place. The upgrade is planned to be finished in 2026.

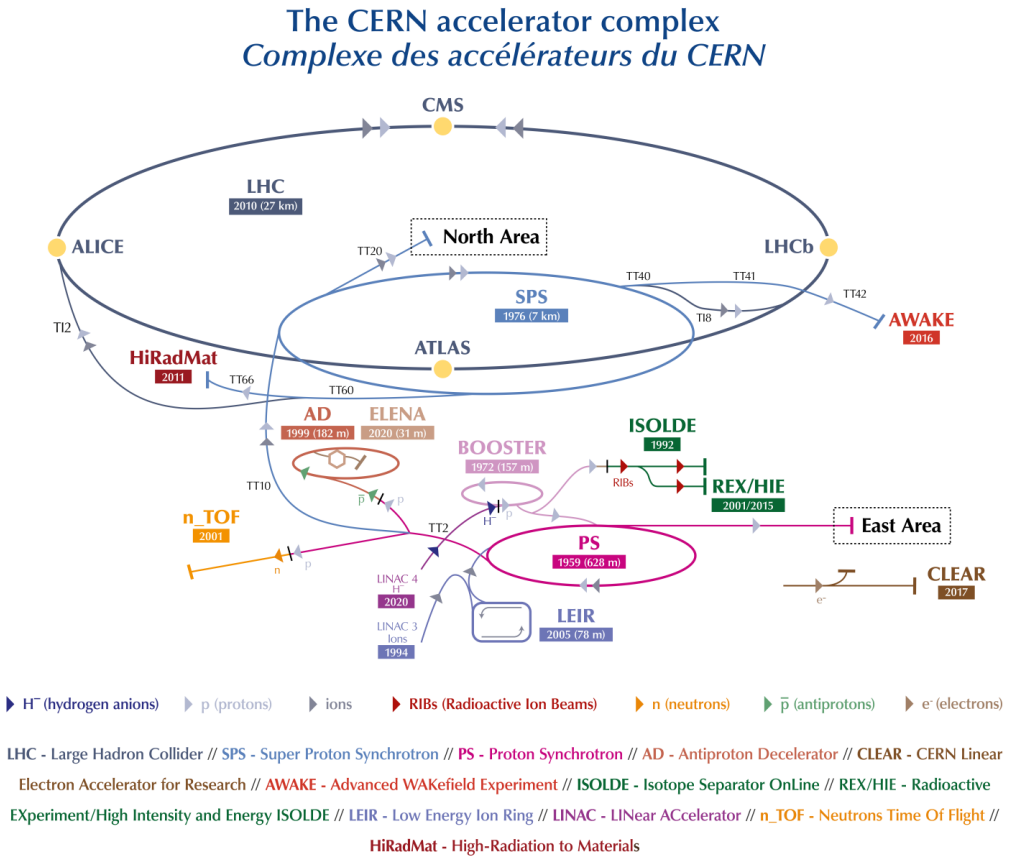

Fig. 2.1 The sketch of the CERN accelerator complex in 2020. The largest ellipse on the top is the LHC. The four main experiments at the LHC, ATLAS, CMS, ALICE and LHCb are also shown. The LINAC2 was used until the end of Run 2 in 2018, and not shown in the picture. [31]

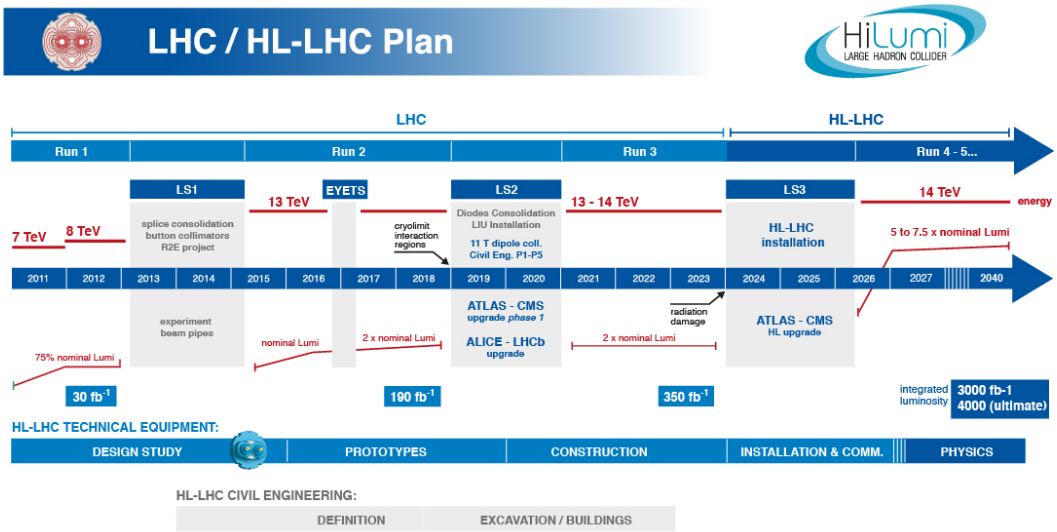

Fig. 2.2 The LHC/HL-LHC Plan. Upgrades of the accelerator and the detectors are planned in the LS2 and LS3 [32].

The instantaneous luminosity can be expressed as the following formula.

$$L = \gamma \frac{n_b N^2 f_{\mathrm{rev}}}{4\pi\beta^* \varepsilon_{\mathrm{n}}} R;\ R = \frac{1}{\sqrt{1 + \frac{\theta_{\mathrm{c}}\sigma_{\mathrm{z}}}{2\sigma}}} \tag{2.1}$$

where γ is the Lorentz factor of the protons, n_{b} is the number of bunches, N is the number of protons in the bunches and the f_{rev} is the bunch crossing frequency. The β^* is the beta function, and the ε_{n} is the normalised emittance in the plane which is perpendicular to the beam axis. The R is the geometrical reduction factor of the luminosity. The parameters included in R are θ_{c} that is the angle between the crossing bunches, the size of bunch in the direction parallel to the beam line σ_{z} , and the size of bunch in the direction perpendicular to the beam line σ.

After upgrading the LHC to the HL-LHC, the number of protons contained in the bunches will be increased up to 2.2×10^{11}. Smaller β^* and ε_{n} will also make a more intense beam that results in an increasing luminosity. Some essential properties of the LHC/HL-LHC are summarized in Table 2.1 for comparison. With the upgrade, ten times more data will be acquired by the HL-LHC, while the increasing instantaneous luminosity will lead to an increasing average pileups that make it harder for event selections.

	LHC (Run2)	LHC (Run3)	HL-LHC (design)
Centre-of-mass Energy $\sqrt{s}$[TeV]	13	14	14
Instantaneous Luminosity [$\mathrm{cm^{-2}s^{-1}}$]	2×10^{34}	2×10^{34}	$5 - 7.5 \times 10^{34}$
Integrated Luminosity [$\mathrm{fb^{-1}}$]	139	300 (with Run 2)	3000
Average Pileups $<\mu>$	35	50-60	150-200

Table 2.1 Essential properties of the LHC/HL-LHC for the ATLAS experiment.

2.2 The ATLAS Detector

2.2.1 Overview of the ATLAS Detector

As described in previous sections, the ATLAS experiment is one of the four big experiments at the LHC. The ATLAS detector is placed in a 100 m underground cavern at one of the interaction points of the LHC.

The ATLAS detector is a general-purpose detector that consists of many sub-detectors with around 100 million electronic channels. The detector is cylindrical, 46 m long and 25 m in diameter, which is the largest in the detectors at the LHC. The total mass of the detector is 7000 t. Fig. 2.3 and Fig. 2.4 show the structure of the ATLAS detector. The beam lines cross at the centre of the detector. Outside the beam pipe, the Inner Detector (ID) is installed to track charged particles produced in the proton-proton collisions. The information of tracks will be used in many steps of event reconstructions such as finding the vertex of collisions, momentum estimation of particles and particle identification. The Liquid Argon Electromagnetic Calorimeter outside the ID is used for catching photons and electrons produced by the collision, and the Tile Hadron Calorimeter detects the hadronised quarks and gluons. As the muon has a strong ability to penetrate the materials, the Muon Detectors are at the outermost of the ATLAS detector. The neutrinos do not interact with any the sub-detectors but can be indirectly detected as missing energy by combining the information of the whole ATLAS detector. The details of the sub-detectors will be described in the following sections.

The positional relation between the sub-detectors of the ATLAS detector is described using a coordinate system called ATLAS coordinate, as shown in Fig. 2.5. The ATLAS coordinate system is a right-hand coordinate, with the collision point as the origin. The direction to the

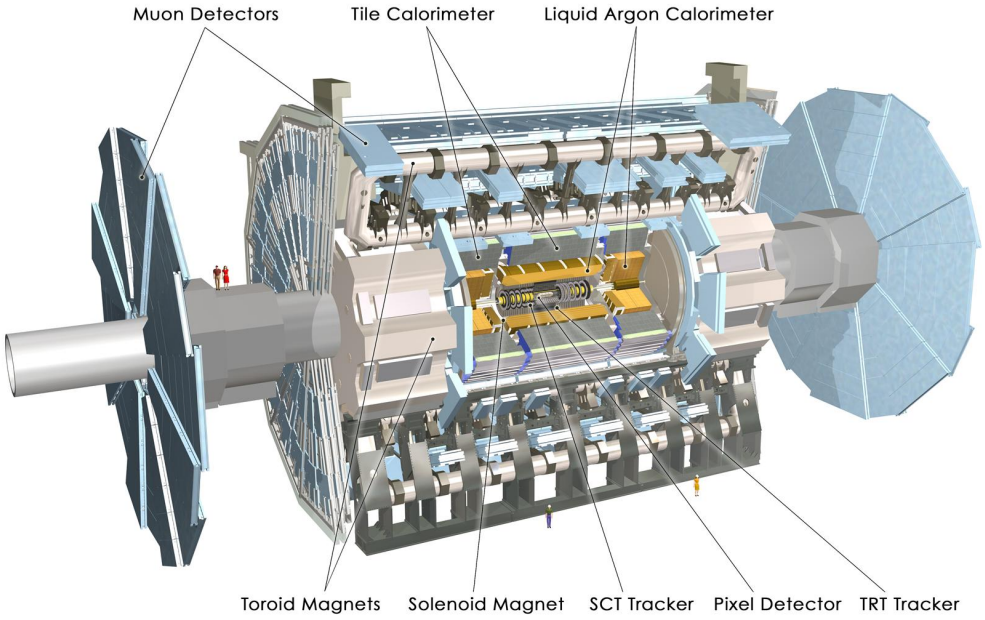

Fig. 2.3 The 3D view of the ATLAS detector. [33]

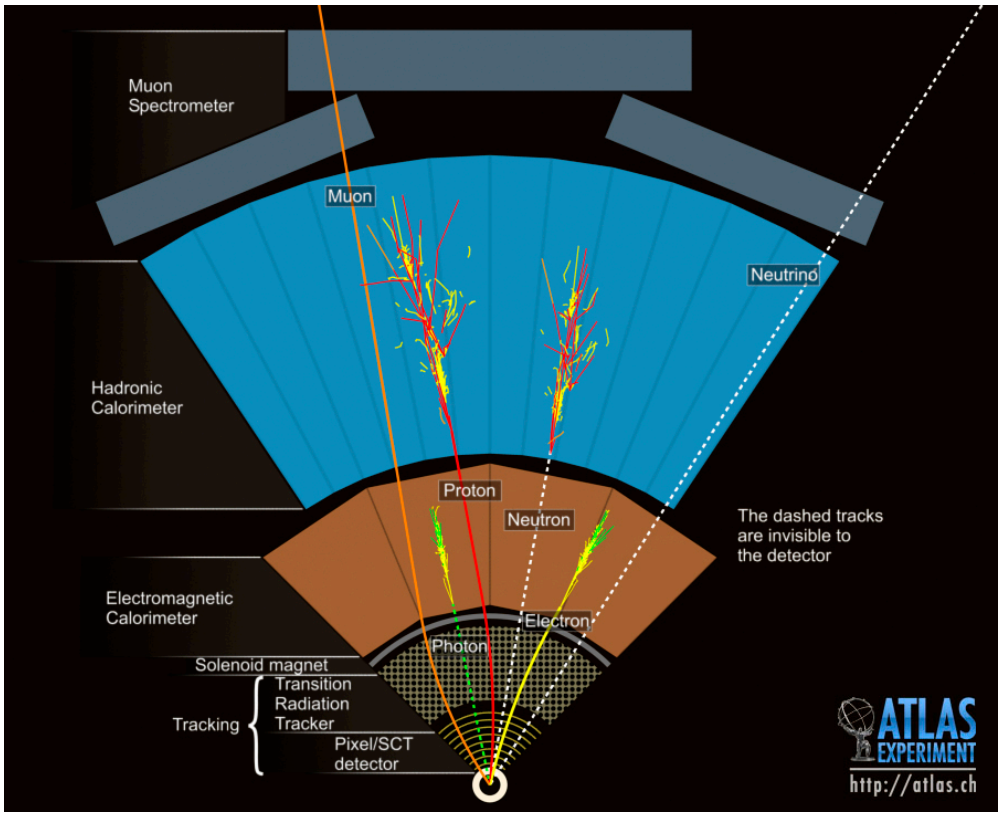

Fig. 2.4 The layered structure of the sub-detectors of the ATLAS detector and the interactions between the detectors and particles produced in the collision. The image is showing part of the sectors in the projection to the plane perpendicular to the beam line [34].

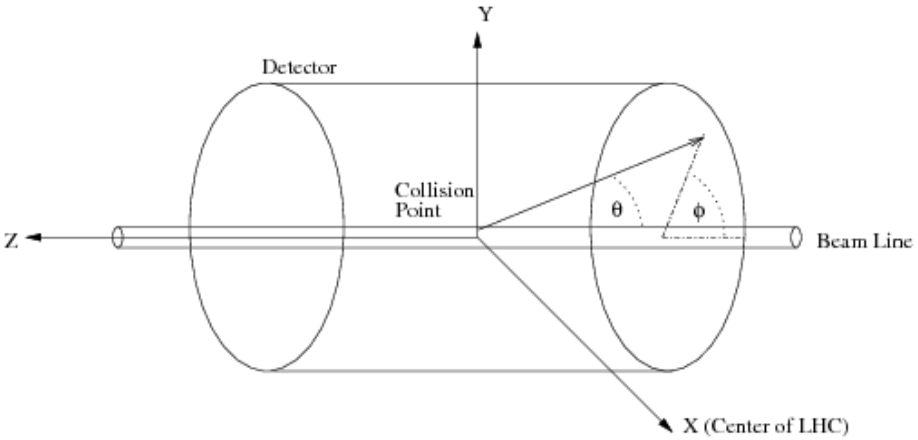

Fig. 2.5 The coordinate system used by the ATLAS detector [35].

centre of LHC is the x-axis positive direction, and the vertically upward direction is the y-axis positive direction. Naturally, the beam line is defined as the z-axis. The position of the sub-detectors can also be rewritten in the form of a cylindrical coordinate system in radius R, z coordinate along the beam line and zenith angle θ. When using cylindrical coordinate, pseudo-rapidity η is more often used than θ. Pseudo-rapidity η is the approximation of Lorentz invariant rapidity w with the assumption that the particles are massless. Strictly, rapidity w is defined as Eq. (2.2).

$$w = \frac{1}{2} \ln \frac{E + p_z}{E - p_z}, \; p_z = |\mathbf{p}| \cos\theta \tag{2.2}$$

where E is the energy of the particle, θ is the zenith angle, and $\mathbf{p}$ is the 3-momentum of the particle. If the particle mass is zero, with the relation $E = |\mathbf{p}|c$, the pseudo-rapidity η can be calculated as Eq. (2.3) as a function of the zenith angle θ.

$$\begin{aligned} \eta &= \frac{1}{2} \ln \frac{|\mathbf{p}| + |\mathbf{p}| \cos\theta}{|\mathbf{p}| - |\mathbf{p}| \cos\theta} \\ &= \frac{1}{2} \ln \frac{1}{\tan^2 \frac{\theta}{2}} \\ &= -\ln \left[\tan \frac{\theta}{2} \right] \end{aligned} \tag{2.3}$$

Typically, in the ATLAS experiment, the region with $\eta > 0$ is defined as A-side, and the other side is C-side. Considering the geometry of the sub-detectors, the region with $|\eta| \leq 1.05$ is called the "Barrel" region and the region with $|\eta| > 1.05$ is called the "Endcap" region. For the region with especially large $|\eta| > 2.4$, the "Forward" region is also defined.

2.2.2 The Magnet System and Detectors

The ATLAS detector is made of a large toroidal magnet system, a solenoid magnet system, and numbers of sub-detectors to detect different particles. The sub-detectors of the ATLAS detector can be classified into three main categories, the Inner Detector (ID), the Calorimeter (Calo), and the Muon Spectrometer (MS).

Magnet System

The magnet system of the ATLAS detector contains an extensive toroidal magnet system at the outer side of the detector, and a solenoid magnet system outside the ID. Both of the magnet systems are superconducting magnets and constantly cooled by the cryogenic system.

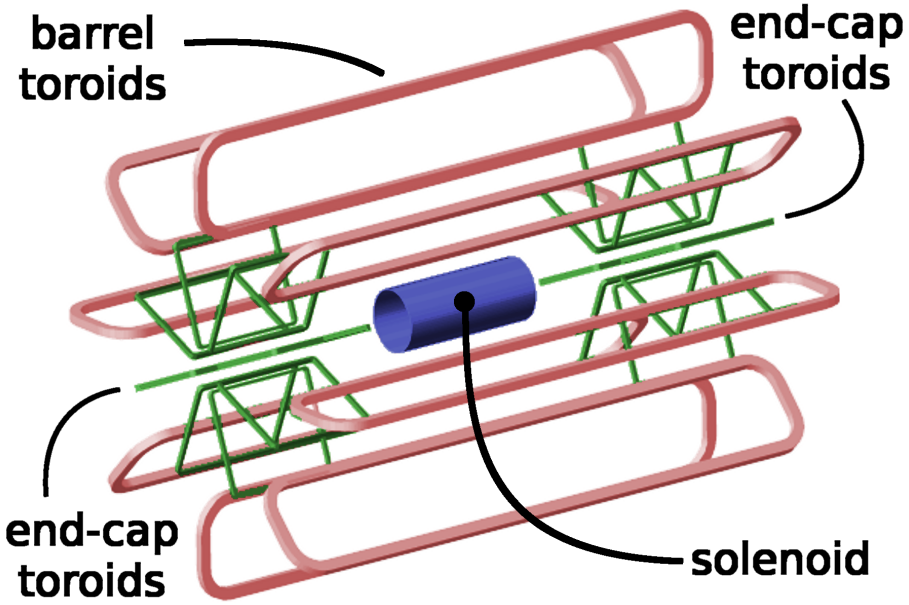

Fig. 2.6 The magnet system of the ATLAS detector. Both toroidal and solenoidal magnet systems are shown [36].

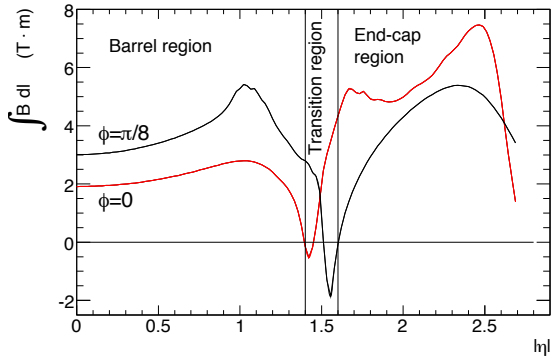

Fig. 2.7 The simulated integral of the magnetic field in the muon spectrometer as a function of $|\eta|$ [33]. The integration is performed along the tracks of infinite momentum muons. The toroidal magnetic field of the ATLAS detector is very complicated, especially in the region $|\eta| \simeq 1.5$. The red line and the black line represent different ϕ region $\phi = 0, \pi/8$ respectively.

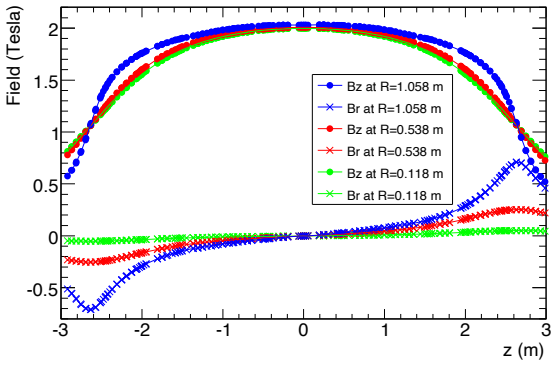

Fig. 2.8 R and z component of the magnetic field in the solenoidal magnet measured as a function of z [33]. Good uniformity in z-direction is observed and almost no magnetic field in the radial direction.

The toroidal magnet contains barrel toroids and endcap toroids, in an eight-fold symmetry, as shown in Fig. 2.6. The barrel toroids are 25.3 m long with inner radius 9.4 m and outer radius 20.1 m. The barrel toroids cover region up to about $|\eta| = 1.5$. The endcap toroids are 5 m long with inner radius 1.65 m and outer radius 10.7 m. The endcap toroids cover region from about $|\eta| = 1.5$ to about $|\eta| = 2.7$. The direction magnetic field created by the toroidal magnet is along the ϕ-direction and perpendicular to the R-z plane.

The strength of the magnetic field created by the toroidal magnet system varies in different η and ϕ. The magnetic field on the superconductor is 4.0 T while the average strength in the barrel region is 0.5 T and in the endcap region is 1.0 T. The variation of the integrated toroidal magnetic field is shown in Fig. 2.7.

The solenoidal magnet system is 5.8 m long and occupies the volume from an inner radius 2.46 m to outer radius 2.56 m. The solenoidal magnetic field is uniform in the z-direction. The strength of the magnetic field at the collision point is 1.998 T, and the dependency on R and z can be confirmed in Fig. 2.8.

Inner Detector (ID)

The innermost sub-detector of the ATLAS detector is the Inner Detector (ID). The purpose of ID is to reconstruct tracks of the charged particles produced in collisions and identify the primary vertex of collisions.

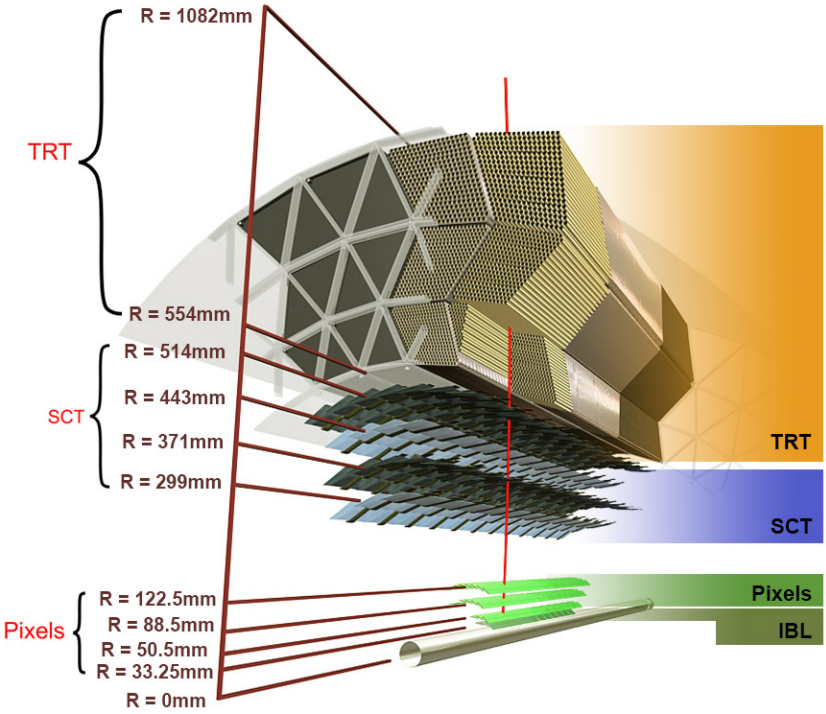

Fig. 2.9 The Inner Detector of the ATLAS detector [37].

As shown in Fig. 2.9, the ID includes 4 types of detectors. The detector nearest to the beam line is the Insertable B-Layer (IBL) which was newly installed from Run 2. The IBL covers the region $|\eta| < 3.0$ and has a pixel size $50\mu\text{m} \times 250\mu\text{m}$. The spatial resolution of the IBL is 8 μm on the $R - \phi$ plane and 40 μm in the z-direction.

Outside the IBL is the Pixel detector, that has three layers in the barrel region, and three plates each on A-side and C-side in the endcap region. The Pixel detector was installed from the construction of the ATLAS detector. The pixel size of the Pixel detector is larger than the IBL, which is $50\mu\text{m} \times 400\mu\text{m}$. The intrinsic spatial resolution for each layer is 10 μm on the $R - \phi$

plane and 115 μm in the z direction in the barrel region. In the endcap region, the z-position is given by the position of the plates, and the resolution of R is 115 μm. The spatial resolution of the ϕ-direction on the $R-\phi$ plane is 10 μm. The IBL and the Pixel detector make the "Pixels" part of the ID. The number of total channels of the Pixel part is 92 million. In other words, about 90% of readout channels are in the Pixels part.

The third type detector of the ID is the Semi-Conductor Tracker (SCT). The SCT is outside the Pixels and has four layers in the barrel region and two sets of nine plates in the endcap for both A-side and C-side. Each layer or plate is made of two pieces of silicon stripe sensors. Two pieces of sensors are set in an angle of 40 mrad so that the detector can determine where the charged particle passed. The spatial resolution of the SCT is 17 μm on the $R-\phi$ plane in all regions. The resolution of z-coordinate is 580 μm in the barrel region and the resolution of R-coordinate is 580 μm in the endcap region. The SCT and the Pixel detector both cover the region $|\eta| < 2.5$.

The last and the outermost layer of the ID is occupied by the Transition Radiation Tracker (TRT). The TRT identifies electrons by detecting the transition radiation emitted when the charged particles are passing through the border of materials with different dielectric constants. The TRT only covers the region $|\eta| < 2.0$, and is made of straw tubes filled by mixed gases with a radius of 4 mm. In the barrel region, the TRT has 73 layers of tubes and in the endcap region, 160 layers of tubes exist. The spatial resolution on the $R-\phi$ plane is 130 μm, and the TRT has no spatial resolution along the direction of the z-axis.

Calorimeter (Calo)

The Calorimeter (Calo) of the ATLAS detector measures the energy of most of the particles produced in the collision. The Calo consists of electromagnetic calorimeter and hadron calorimeter, as shown in Fig. 2.10, and can identify the type of particles by the place where the shower occurs. The Calo covers the region $|\eta| < 4.9$.

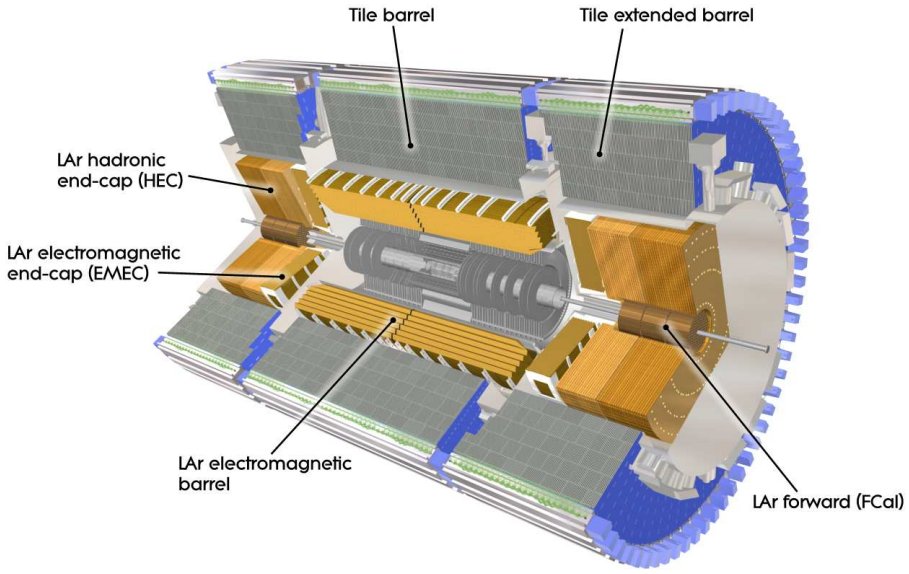

Fig. 2.10 The Calorimeter of the ATLAS detector. The ID is also shown in the centre of the picture [33].

The electromagnetic calorimeter is liquid argon calorimeter with lead absorbers. The electromagnetic calorimeter has three layers in the region $|\eta| < 1.35$ and the region $1.5 < |\eta| < 2.5$, and

two layers in other regions. The electromagnetic calorimeter covers the region up to $|\eta| = 3.2$. Thickness of the calorimeter is often written with the unit of radiation length X_0. The thickness of the calorimeter in the barrel region is more than $22X_0$, in the endcap region is more than $24X_0$. The granularity of the electromagnetic calorimeter is 0.1×0.1 described in $\Delta\eta \times \Delta\phi$ on average.

The hadron calorimeter in the region $|\eta| < 1.7$ is tile calorimeter that consists of plastic scintillators and iron absorbers. The tile calorimeter has three layers, and the thickness is more than 8 λ (nuclear collision length). The granularity of tile calorimeter is 0.1×0.1 described in $\Delta\eta \times \Delta\phi$ for the first two layers and 0.2×0.1 for the out-most layer. In the region $1.5 < |\eta| < 3.2$, four layers of liquid argon calorimeters with copper absorber are used as hadron calorimeter. The thickness in this region is more than 10 λ. The granularity described in $\Delta\eta \times \Delta\phi$ is 0.1×0.1 in the region $|\eta| \leq 2.5$ and 0.2×0.2 in the region $2.5 < |\eta| \leq 3.2$.

For the region $3.1 < |\eta| < 4.9$, liquid argon calorimeter with copper and tungsten absorber called the Forward Calorimeter (FCal) is used as an electromagnetic calorimeter and hadron calorimeter at the same time. The FCal has three layers, and the granularity varies in different layers and $|\eta|$ region from 3.0 cm $\times$ 2.6 cm to 5.4 cm $\times$ 4.7 cm in $\Delta x \times \Delta y$.

Muon Spectrometer (MS)

Because of the strong penetration ability of muons, it is not easy to measure the energy of high momentum muons with the calorimeters. In the ATLAS experiment, the momentum of the muons are measured instead. The momentum of muons can be measured by measuring the curvature of muon tracks in the magnetic field. To achieve high momentum resolution, longer arm length in the momentum measurement is more desirable, and this results in that most of the volume of the ATLAS detector is occupied by the Muon Spectrometer (MS).

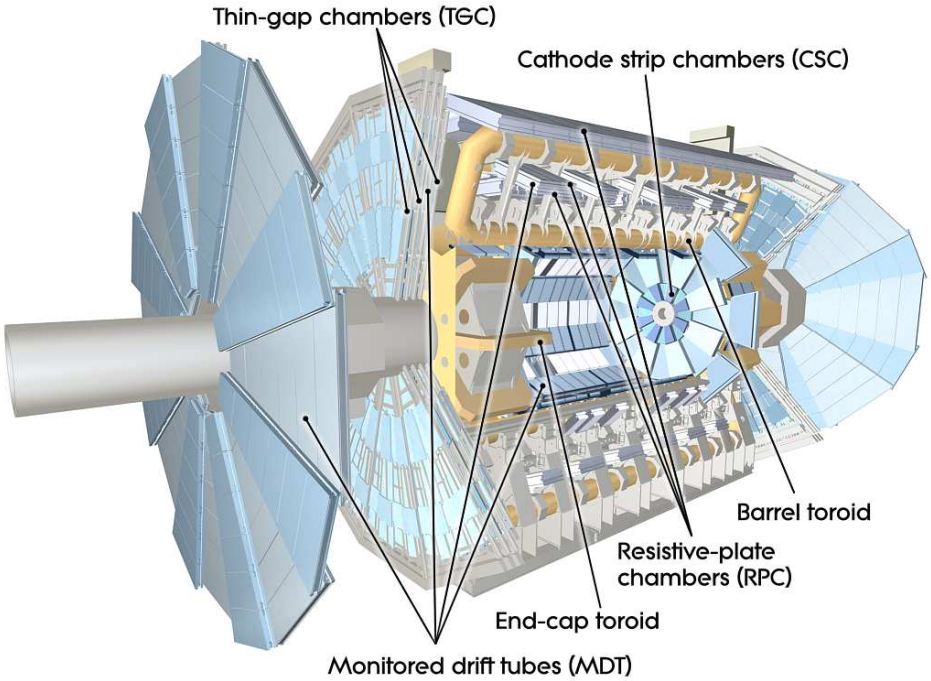

Fig. 2.11 The Muon Spectrometer of the ATLAS Detector. The toroidal magnet system is also shown [33].

The MS consists of four types of muon detectors, covering the region $|\eta| < 2.7$, as shown in Fig. 2.11. The Thin-Gap Chambers (TGC) and the Resistive-Plate Chambers (RPC) are gas detectors with quick response and excellent time resolution. Therefore the TGC and RPC are used for hardware-based muon triggering. The Monitored Drift Tubes (MDT) and Cathode Strip Chambers are detectors which have good spatial and angular resolution, but long readout time, so the information from the MDT and CSC are used for precise measurement in subsequent steps.

The structure of the muon detectors is corresponding to the octant structure on the R-ϕ plane. As a result, 16 sectors are defined in the case of the MS. 8 out of 16 sectors are called Large Sectors, and the other 8 sectors are called Small Sectors, simply depending on the size of the detectors. The numbering of the sectors starts from the $\phi = 0$ of the ATLAS coordinate. The Large Sector with centre at $\phi = 0$ is defined as Sector 1. Then the neighbouring small sector at the positive ϕ side is sector 2, and the next large sector is sector 3. The details of sector numbering can be confirmed in Fig. 2.12 and Fig. 2.13. In the area where the ATLAS "feet" - pillars to support the detector structure - exist, the positions of muon detectors are different from other sectors. These sectors (Sector 11, 12, 14, 15) are called Special Sectors and have sector-specific algorithm to measure muon momentums.

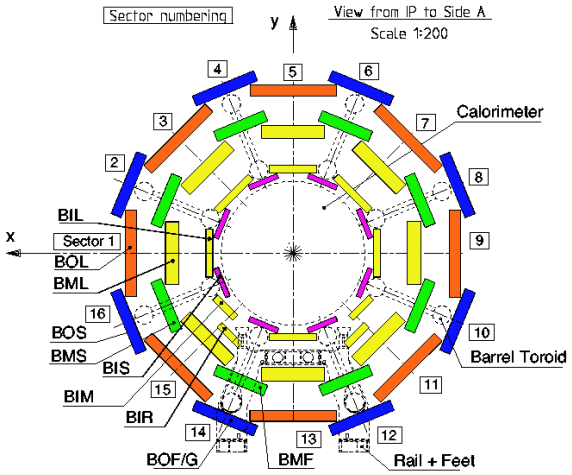

Fig. 2.12 Numbering of the sectors of the muon spectrometer in the barrel region in the $x - y$ panel, looking from the A-side. The numbering of sectors in the endcap region is corresponding to the sector number in the barrel region [33].

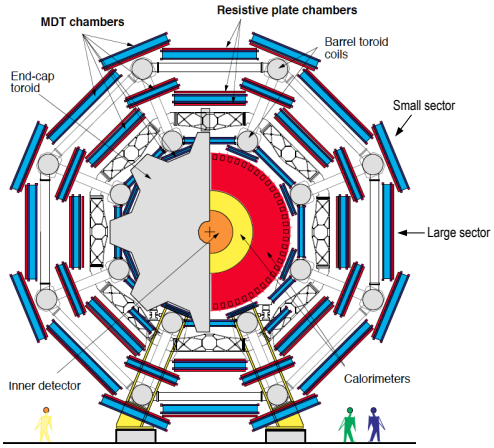

Fig. 2.13 Sectional view of the ATLAS detector in the $x - y$ panel, looking from the A-side. The spatial relation between the toroidal magnet and muon detectors can be confirmed [33].

Typical arrangements of muon detectors in the large and small sector are shown in Fig. 2.14. The MDT has three stations in each region. In the order of the distance from the interaction point, the three stations are named Inner, Middle and Outer. Because of the height limit due to the size of cavern, the Endcap Outer station only covers the region $|\eta| > 1.5$. So Endcap Extra MDT (EE station) is added to the region $1.3 < |\eta| < 1.5$ to ensure that all regions have three stations of muon detectors for precise momentum measurement. In the forward region $2.0 < |\eta| < 2.7$, due to the existence of particles created by accidental collisions of protons and beam pipe, the hit rate is expected to exceed the performance limit of the MDT. To resolve this problem the MDT Inner station is replaced by the CSC in this region.

The TGC and the RPC are installed near the MDT. Two layers of TGCs are set in front of and behind the endcap MDT Middle station and one more layer at the outer side, cover the

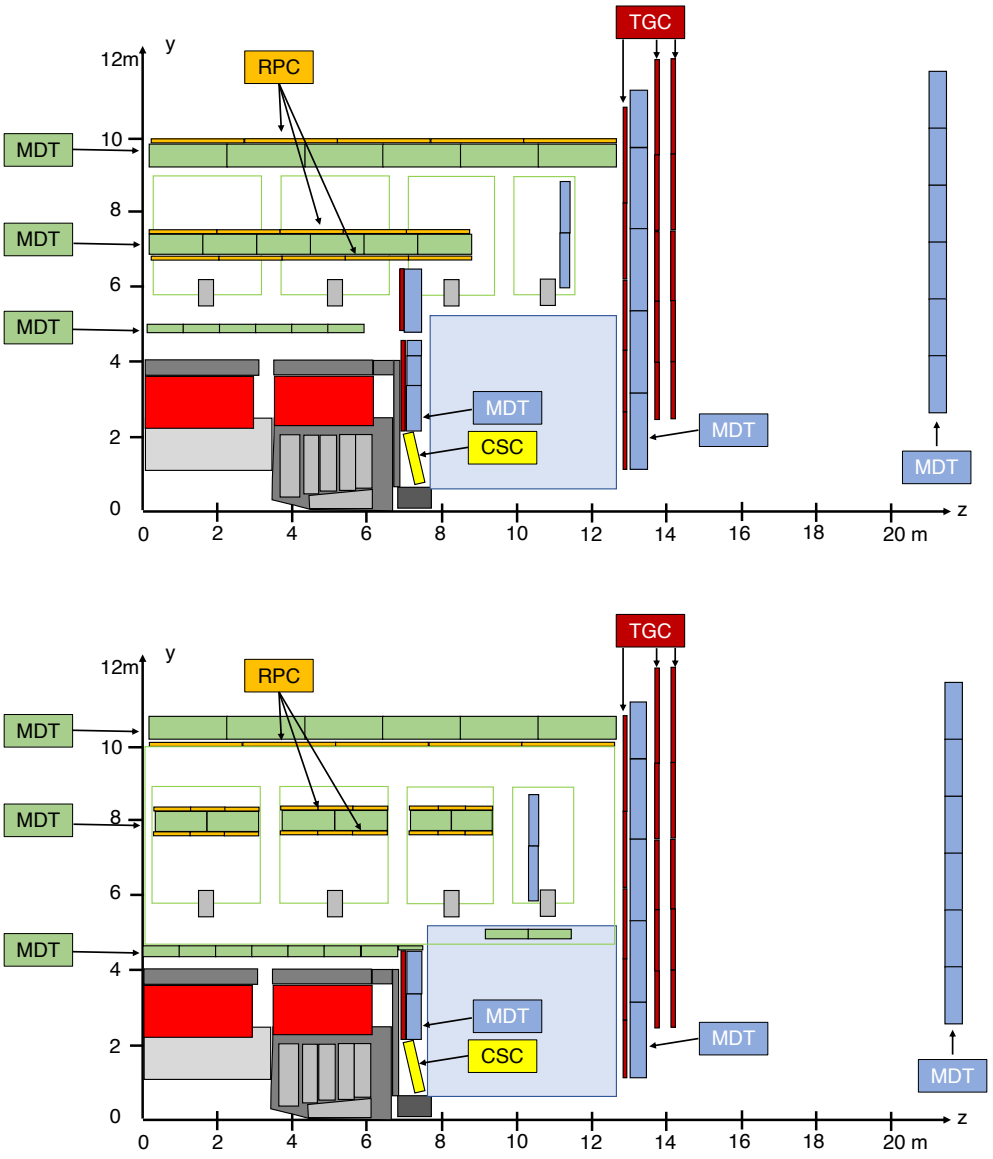

Fig. 2.14 Sectional view of the ATLAS Muon detectors of the Large (top) sector and the Small (bottom) sector. Current arrangement of detectors in the Run 2 is shown.

region $1.05 < |\eta| < 2.4$. At the endcap Inner station, one layer of TGC is also installed. In the case of barrel region, the chambers are set on both sides of the Middle station, and one layer of RPC is installed behind the barrel MDT Outer station. The RPC covers all the barrel region.

Thin-Gap Chamber (TGC)

The Thin-Gap Chamber (TGC) is used for triggering muons in the endcap region. The TGC is a MultiWire Proportional Chamber (MWPC). In the chamber, mixed gas (CO_2 : n-C_5H_{12} = 55 : 45) is filled. Anode wires and cathode strips are placed perpendicular to each other in the TGC. In the ATLAS MS, two types of TGC are installed, one is doublet that has only two gas gaps, and the other one is triplet which has three gas gaps. The cross-section view of the doublet and triplet TGC is shown in Fig. 2.15.

The TGC has good time resolution of 4 ns, and the spatial resolution is 2-6 mm in R-direction

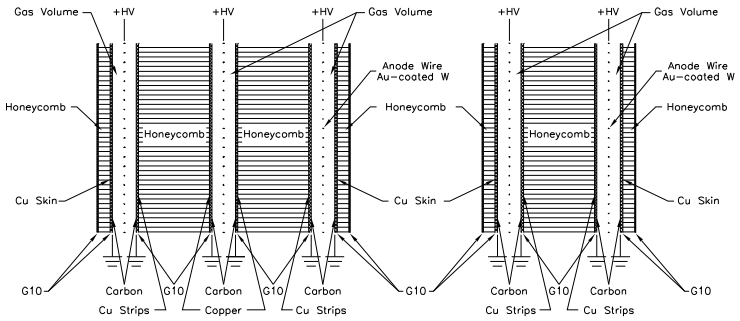

Fig. 2.15 Cross-section view of the doublet (left) and the triplet (right) TGC [33].

and 3-7 mm in ϕ-direction.

Resistive-Plate Chamber (RPC)

The Resistive-Plate Chamber (RPC) is used for triggering muons in the barrel region. Different from the TGC, each RPC unit is made of two plates of electrode with a 2 mm gap, without any wires. Between the two electrodes, the mixed gas ($C_2H_2F_4$: Iso-C_4H_{10} : SF_6 = 94.7 : 5 : 0.3) is filled. When a charged particle passes through, the electronic avalanche will quickly occur in the ionised gas.

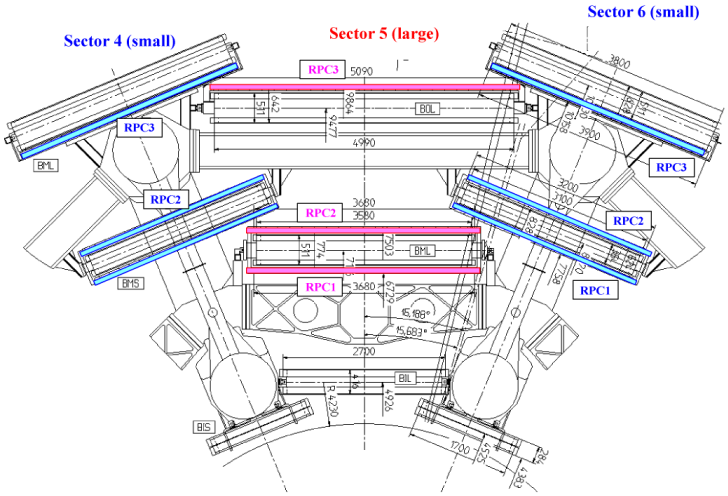

Fig. 2.16 Placement position of the RPC in large and small sectors [33].

The time resolution of the RPC is 1.5 ns, while the spatial resolution is 10 mm along the z-direction and 5-10 mm in the ϕ-direction.

Monitored Drift Tubes (MDT)

The MDT is a gas tube detector used for precise measurement of muons in most regions of the ATLAS MS. Three stations of MDT detectors are installed both in the barrel region and the endcap region. A unit of MDT detector is shown in Fig. 2.17. The MDT unit consists of 2 superlayers isolated by three spacer bars. Each superlayer is made of 3 layers (or 4 layers for the Inner station) MDT tubes.

The MDT tube is a drift tube with a diameter of 29.970 mm. In the centre, an anode wire is stretched through the tube and the tube wall is the cathode. In the tube, gas mixed by 93% of argon and 7% of carbon dioxide and slight water steam is filled at a pressure of 3 atm.

When muons pass through the MDT, hit signals are generated in the MDT tubes. A drift radius can be measured tube-by-tube, by calculating the difference between the bunch crossing time and the arrival time of the first charge. The longest drift time is around 700 ns, so an MDT tube will be busy once a muon passed and insensible in following a few tens bunch crossings.

The resolution of the drift radius is 80 μm. However, with just one hit we can not determine the exact point where the muon passed on the circle. Hence it is necessary to calculate the segment of muons trajectory in the MDT detector with information from multiple hits. The spatial resolution with combined information from MDT tubes is 35 μm along z-direction in the barrel region or R-direction in the endcap region in each station. The MDT has no resolution in ϕ-direction.

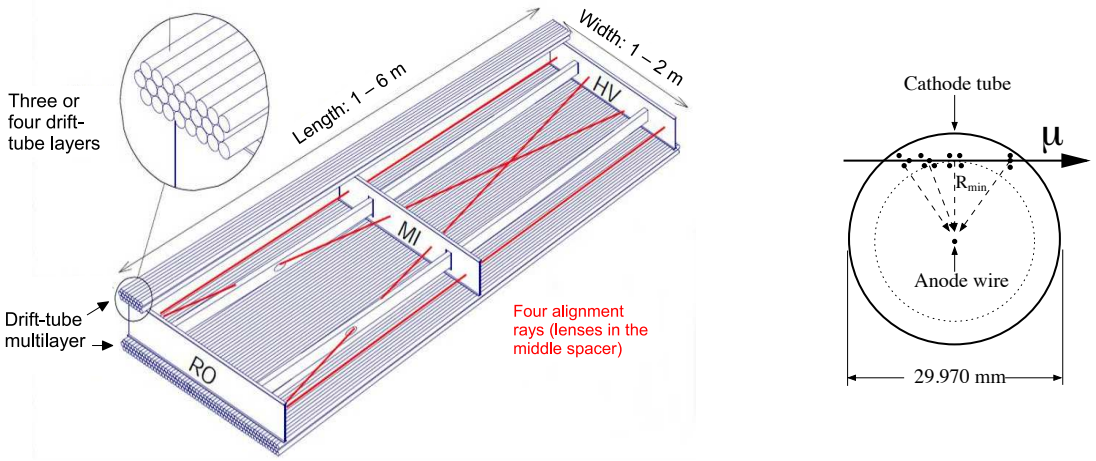

Fig. 2.17 Unit of the MDT, consists of 2 superlayers which are made of 3 (or 4 for Inner station) layers of MDT tubes. Red lines show the alignment laser for geometry monitoring of the MDT (left). The sectional view of an MDT tube (right) [33].

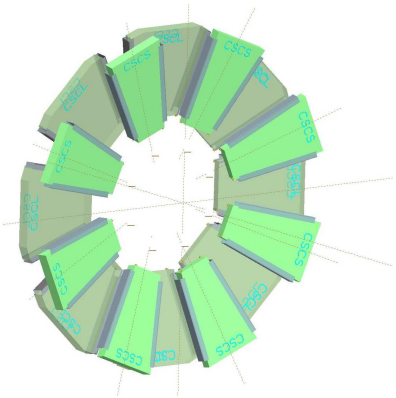

Fig. 2.18 Layout of the CSC. The structure of large and small sectors can be confirmed [33].

Cathode Strip Chamber (CSC)

The Cathode Strip Chamber (CSC) is a MWPC with mixed gas of 80% argon and 20% of carbon dioxide. The anode wires of CSC are oriented in the R direction, and cathode strips in different directions are used. Cathode strips which are perpendicular to the anode wires provide precise measurement of the position in R. On the other hand, cathode strips which are parallel to the anode wires provide transverse position measurement. This structure leads to a good time resolution with a good spatial resolution. As other muon detectors, the CSC is also divided into 16 sectors corresponding to the structure of the ATLAS detector, as shown in Fig. 2.18.

The CSC detector has a 7 ns time resolution and 60 μm spatial resolution on the CSC plane. If the information from two cathode strips combined, the calculated muon segment will have a 40 μm resolution in r-direction and 5 mm resolution in ϕ-direction.

2.2.3 Muon Trigger System of the ATLAS Detector

As described in previous sections, the proton-proton collision occurs every 25 ns at the interaction point when the LHC is in regular operation, and the frequency of collisions is more than 2×10^9 Hz. It is impossible to record all collision data with a reasonable cost using current technology. In the ATLAS experiment, a multi-level trigger system is introduced to select the events that we are interested in with physical motivations.

The ATLAS trigger system at Run2 consists of a hardware-based Level-1 (L1) Trigger and a software-based High-Level Trigger (HLT). The trigger rate of the L1 trigger is approximately 100 kHz, and the event rate after the HLT is about 1 kHz [38].

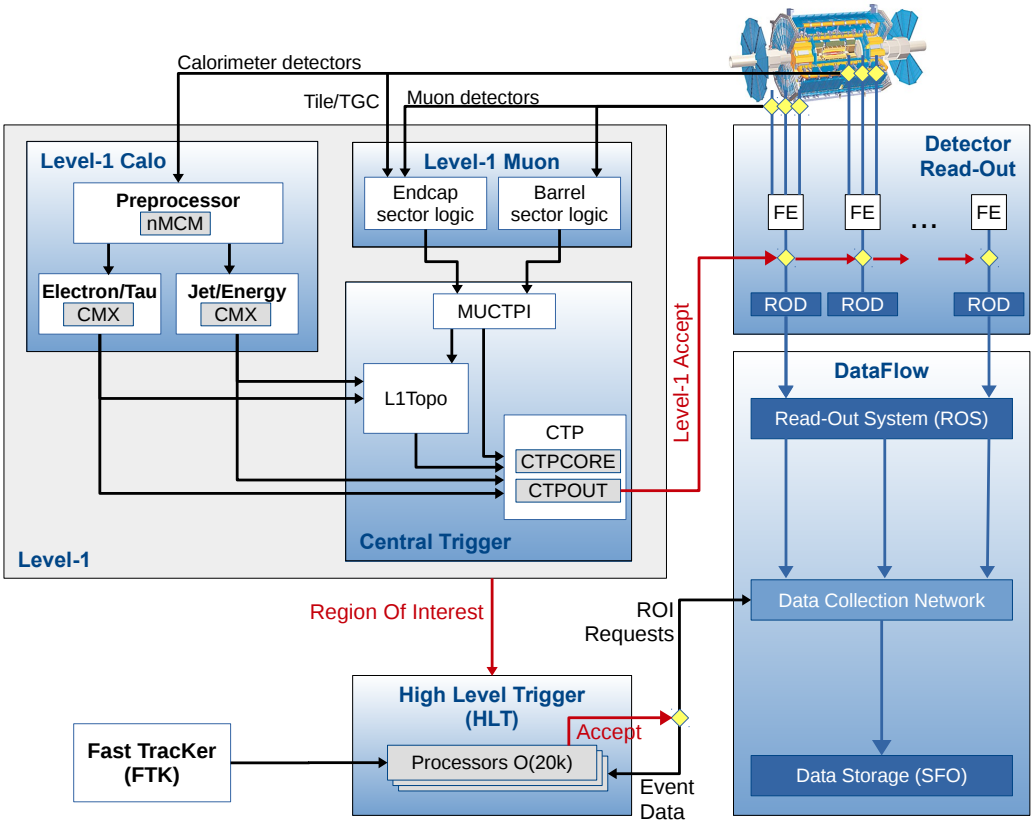

Fig. 2.19 Schematic layout of the ATLAS trigger and DAQ system in Run 2 [38].

As shown in Fig. 2.19, in the L1 step, trigger systems of the Calo and the MS first process information from the detectors independently. Then the information is sent to the central trigger processor. The central trigger processor (CTP) decides to reject the event or pass the event to the HLT. A region of interest (RoI) is also passed to the HLT from the CTP when an L1 trigger is issued. The time that the L1 trigger can use is up to 2.5 μs.

In the HLT step, the information from all sub-detectors of the ATLAS detector is used to reconstruct the physical objects. The main object findings are conducted around the RoI given by the L1 trigger. Complex algorithms that are similar to, or the same as the offline reconstruction algorithms are used in the HLT to precisely select the events which are possibly related to the new physics. The time for the LHC trigger decision is up tp 200 ms.

Focusing on the muon trigger system of the ATLAS detector, it also consists of the L1 Muon Trigger and the High-Level Muon Trigger. In the L1 muon trigger, the trigger system for the barrel region and the trigger system for the endcap system operate separately, and the outputs of the two-part system are processed at the MUon to Central Trigger Processor Interface (MUCTPI) before being sent to the CTP. In the muon trigger system, the common condition used for the selection of muons is the transverse momentum p_{T} of the muons. The trigger conditions usually require the existence of one or several muons having p_{T} larger than the pre-configured p_{T} threshold.

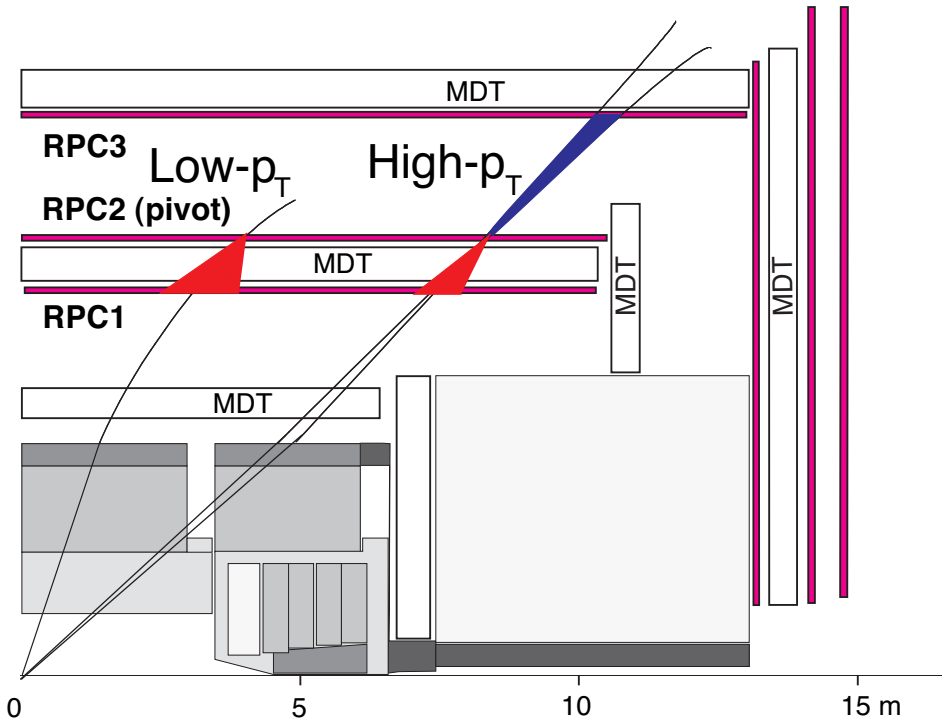

Fig. 2.20 The L1 muon trigger in the barrel region. Coincidence between different RPC stations is required. The number of stations required and the width of the road depends on the threshold of p_{T} [33].

Level 1 Muon Trigger

The L1 muon trigger in the barrel region only uses information from the RPC. Fig. 2.20 shows the schema of the L1 RPC muon trigger. The three layers of the RPC are named RPC1, RPC2 and RPC3. The RPC2 is the pivot station of RPC. When a charged particle passes the RPC and

generates a hit in the RPC2, a coincidence window is defined for finding hits in other two RPC stations. The width of the window is different for different p_{T} threshold. For low-p_{T} muons, only coincidence of the RPC1 and RPC2 is required, and the window is wider because the low-p_{T} muons draw a more curved track in the magnetic field. Higher-p_{T} muons have straighter tracks, and the coincidence requirement is hits in all three RPC stations with a narrower window.

Since the RPC stations have a doublet structure, up to two hits can be found in each RPC station. The trigger with low-p_{T} thresholds will be fired when at least three out of four hits found in RPC1 and RPC2. For high-p_{T} thresholds, at least one more hit is additionally required in the RPC3. When the coincidence condition is met, and the trigger is fired, a 0.1×0.1 ($\Delta\eta \times \Delta\phi$) sized RoI will be issued for HLT processing.

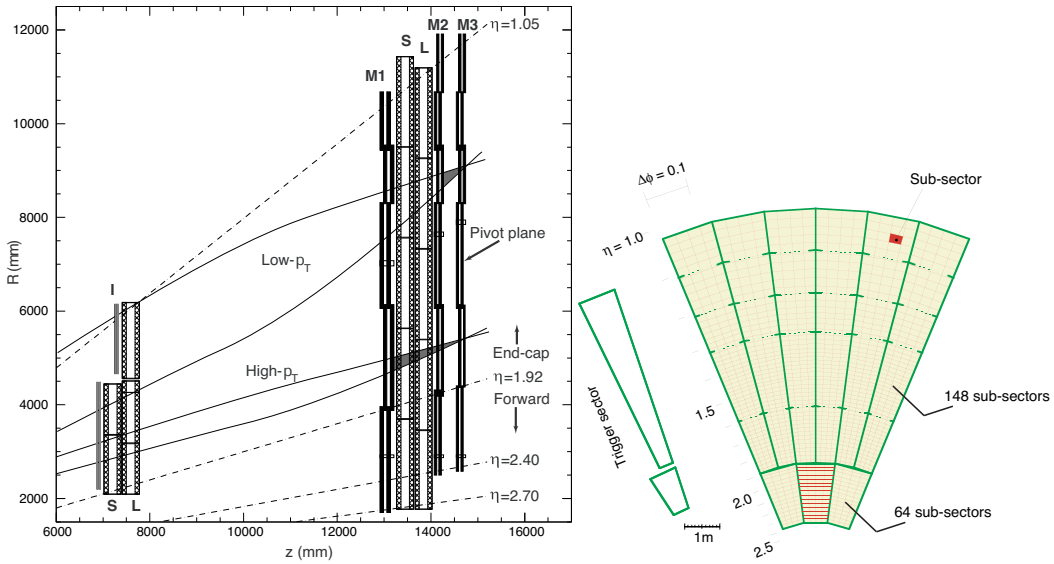

Fig. 2.21 The L1 muon trigger in the endcap region (left), and the segmentation of the L1 muon endcap trigger (right) [33].

In the endcap region, the L1 trigger is issued by the TGC. In Fig. 2.21 (left), the four layers of TGC are named I, M1, M2, M3 in the order of distance from the interaction point. The I, M2 and M3 are doublet TGCs, and the M1 is triplet TGC. In the same way as the RPC trigger, the M3 is used as the pivot station in the TGC trigger. When a hit is found in M3, a track of a virtual muon with infinite momentum will be drawn by connecting the hit position and the detector centre. Then a window for hit coincidence finding is defined for different p_{T} thresholds. The coincidence signals between M2 and M3 are generated independently for R and ϕ directions. The issue of a TGC trigger requires a coincidence of a least three out of four hits for both TGC wires and TGC strips. For the high-p_{T} thresholds, at least two out of three hits on the TGC wire plane and at least one out of two hits on the TGC strip plane are also required for the M1 triplet.

Since the M1, M2 and M3 TGCs are outside the ATLAS toroidal magnetic field, no curvature can be measured with the three TGC layers in the Middle station. To roughly determine the p_{T} of the muons, the TGC trigger draws a track of infinite momentum muon by connecting the position of hits in M3 and the detector centre and compares the ΔR and $\Delta\phi$ between the virtual track and hits in M1 and M2. High-p_{T} muons will have small ΔR and $\Delta\phi$ and the ΔR and $\Delta\phi$ of low-p_{T} muons will be larger. Coincidence windows corresponding to different p_{T} thresholds are defined with the results of simulation in ΔR and $\Delta\phi$. The trigger decision will be given by checking the $R-\phi$ coincidence with the information from the I station and the tile trigger. The RoIs issued by the TGC trigger are defined with the sub-sector where the hits were found. The

details of the segmentation of the TGC can be confirmed in Fig. 2.21 (right).

Results of the RPC trigger and the TGC trigger are passed to the MUCTPI. In the MUCTPI, the information from all sectors of the barrel and the endcap regions is combined. With the information from the whole ATLAS MS, the MUCTPI counts the number of muon track candidates passing different p_{T} thresholds and resolves the overlap between candidates in different sectors. Then the number of muon candidates and the related information are sent to the CTP for L1 trigger processing. On the other hand, the RoIs issued by the L1 muon trigger with the information of passed p_{T} thresholds are sent to the HLT for more precise calculation.

High-Level Muon Trigger

In the HLT step of the muon trigger, three steps of algorithms are used for the p_{T} calculation of muon track candidates. The first step is called Muon Stand Alone (MuonSA), and the second is called Muon Combined (MuComb). The last step of the HLT is Event Filter (EF).

MuonSA The MuonSA algorithm calculates the p_{T} of muons with the information of the MS without any help from other sub-detectors. The MuonSA first reconstructs muon segments in MDT stations with the RoI given by the L1 trigger. The muon segments are partial muon tracks in each station. In the reconstruction, MDT hits around the input RoI will be collected with references to the hits in TGC or RPC. Since the thickness of each station is small enough compared to the size of the MS, the partial tracks are considered to be straight. The direction and the representative position of the segments are calculated by performing least-squares fittings using the MDT hits information.

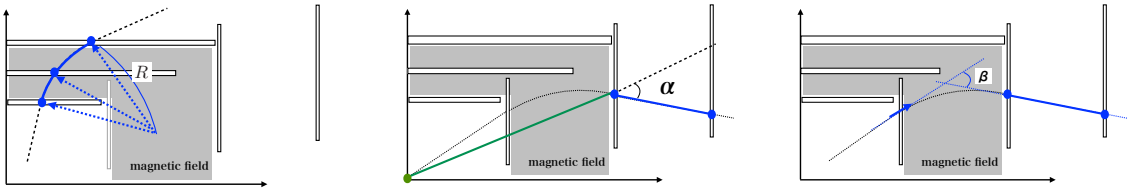

Fig. 2.22 Parameters used for the MuonSA algorithm [39].

In the barrel region, when segments are successfully reconstructed in all three stations of the MDT, the MuonSA assumes the magnetic field is completely uniform, and the three segments represent three points of the circular muon track. When only two out of three segments are reconstructed, the path of the muon is considered as a straight line from the detector centre to the Inner MDT station, and then a circle in the toroidal magnetic field. The direction of the segments can help the selection of the best-reconstructed track. Then by comparing the curvature radius of the track to the Look-Up Table (LUT), the p_{T} of the muon track can be acquired.

In the case of the endcap region, because no magnetic field exists between the endcap Middle station and the endcap Outer station, the curvature radius can not be calculated when $|\eta| > 1.5$. Instead, angular parameters correlated to the p_{T} of muon are used for the selection. Typical parameters used for the MuonSA in endcap region is α and β, defined as shown in Fig. 2.22. Same as the curvature radius, by using the LUT of the calculated parameters, the p_{T} can be acquired. For the region $1.05 < |\eta| < 1.5$, by using the endcap Middle station as Outer and let the endcap Extra station play the role of Middle station, 3-station reconstruction is possible, and the p_{T} can be estimated similar to the barrel region.

MuComb The MuComb algorithm uses the p_{T} calculated by the MuonSA and the tracking information of the ID as input. The MuComb performs a matching between muon tracks reconstructed in the MS and the ID tracks. If the tracks successfully matched with each other, p_{T} from the matched ID track $p_{\mathrm{T,ID}}$ will be acquired from the ID. Then the MuComb calculates $p_{\mathrm{T,Comb}}$ by combining weighted $p_{\mathrm{T,ID}}$ and $p_{\mathrm{T,MS}}$. The biggest difference between $p_{\mathrm{T,Comb}}$ and

$p_{\mathrm{T,MS}}$ is that $p_{\mathrm{T,Comb}}$ has corrected the energy loss in the Calo using information from ID. The correction is necessary and with $p_{\mathrm{T,Comb}}$, more accurate event selection is possible. The muons that are reconstructed by the MuComb algorithm are called combined muons.

Event Filter Finally, all the information will be transferred to the Event Filter (EF) for more complicated selections. In the EF step, information from the whole detectors and algorithms that are same as the offline reconstruction are used. As a result, the EF can investigate more event details. For example, the EF can resolve the collimated muon tracks, as well as reconstruct muons that are not triggered by the L1 trigger. The final muon trigger decision on event level will be made by the EF.

2.3 Upgrade of the ATLAS Detector

2.3.1 Overview of the ATLAS Detector Upgrade Plan

The upgrade of the ATLAS detector is synchronised with the upgrade of the LHC, as shown in Fig. 2.2. In the Long Shutdown 2 (LS2), the Phase I upgrade for Run 3 and preparation of the upgrade for HL-LHC will be conducted. The installations and commissions for the Phase II upgrade are scheduled in the LS3. After the LS3, the ATLAS detector will be ready for the operation under high luminosity environment.

The Phase I upgrade includes upgrades of the muon spectrometer and the readout system, that increase the accuracy of particle reconstruction. New sub-detectors will be installed in the Phase I upgrade to increase the coverage of detectors and the performance of trigger system.

In the Phase II upgrade, large-scale upgrades take place everywhere in the ATLAS detector. The ID will be completely replaced, and the covered region will be extended up to $|\eta| = 4.0$. To deal with a large number of tracks produced under the high luminosity environment, the TRT will be removed and replaced by silicon strip detectors in the new ID. The new Pixels will use a new type of pixel detector which has a smaller pixel size. A new readout upgrade for the calorimeter readout is planned to subtract the pileup components effectively . New muon detectors will be added in the Phase II upgrade, and the muon trigger system will be re-designed.

2.3.2 The ATLAS Detector after Phase I Upgrade

In the Phase I upgrade, the endcap Inner station of the muon detectors will be replaced by the New Small Wheel (NSW), and the readout system of the Calorimeter will also be upgraded.

With the increase of luminosity, a much higher hit rate in the endcap region is predicted. The expected rate in the HL-LHC can exceed the rate limit of the CSC. The Inner station MDT and CSC will be wholly replaced by a new type detector which is a combination of MicroMegas (MM) and small-strip TGC (sTGC) to maintain the measurement accuracy and the environment of trigger system [40].

The structure of MM is shown in Fig. 2.23. The MM has a conversion gap as conventional gas detectors. The charged particles ionise the gas in the conversion gap, and the ionised electrons drift to the readout strips. Then in the amplification gap, the signals are significantly amplified before readout. The quick drift time and the fine structure of the readout strips provide the MM with good time resolution and spatial resolution.

The basic structure of the sTGC is similar to the TGC detector, but the smaller pitch between the TGC strips gives the sTGC better spatial resolution than the TGC used for the current muon triggering [42]. With the combination of the MM and the sTGC, the NSW can determine the position of muon segments with a resolution of 100 μm and the direction with an angular resolution of 1 mrad.

According to the newest plan up to date, only the A-side NSW will be installed to the ATLAS detector at the end of LS2, and the C-side NSW is under construction and will be installed during

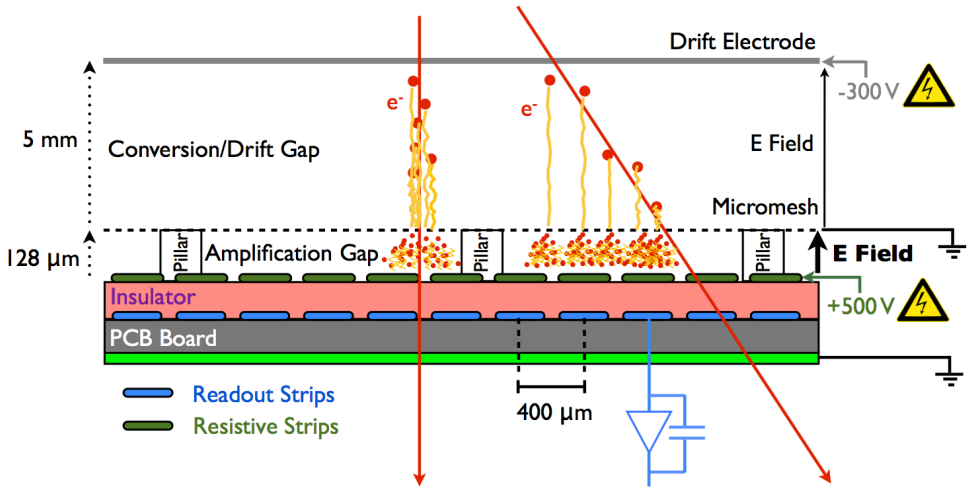

Fig. 2.23 The structure of the MicroMegas detector. The gap width for the amplification is narrower than conventional gas detectors, and this makes the MM has better time response [41].

the technical stop during the Run 3 period. For the upgrade of Calorimeter, the new readout system will provide the ability to achieve information from the Calo with a smaller granularity which improved the accuracy of jet reconstruction. The rigger system will also be upgraded corresponding to the changes in Phase I upgrade [43].

2.3.3 Phase II Upgrade of Muon Detectors

After the NSW are installed in the Phase I upgrade, new muon detectors are added in the Phase II upgrade [44]. The sectional view of the ATLAS Muon detectors in the HL-LHC is shown in Fig. 2.24.

In the barrel region, with the new RPC station added to the barrel Inner station next to the MDT, the coverage of RPC will significantly increase, and as a result, higher efficiency of trigger is expected. Because of the existence of the barrel toroidal magnet, the MDT detectors in the small sectors are replaced by small MDT (sMDT) detectors, to make space for the new RPC

For the large sectors, the doublet TGC which is behind the remained Inner station MDT in the EE region, will be replaced by a triplet TGC. This upgrade increases the sensitivity of the inner station TGC and makes the trigger seeding from the endcap inner station possible.

The High-η tagger is proposed to be installed to the ATLAS detector to cover the muons in large η region. The High-η tagger covers the regions $2.7 < |\eta| < 4.0$. The High-η tagger can be either a gas chamber detector or an additional pixel detector. When hits are found in the High-η tagger, the information from ID will be used to reconstruct muon in the very forward. The High-η tagger only indicates the existence of the muon and the p_{T} will be calculated using only ID information.

The electronics of the whole muon spectrometer system will be re-designed. The information from RPC and TGC can be used in every step of the triggering after the Phase-II upgrade. Faster readout for the MDT will also be introduced, and with larger buffers, the latency for the first level trigger will be extended.

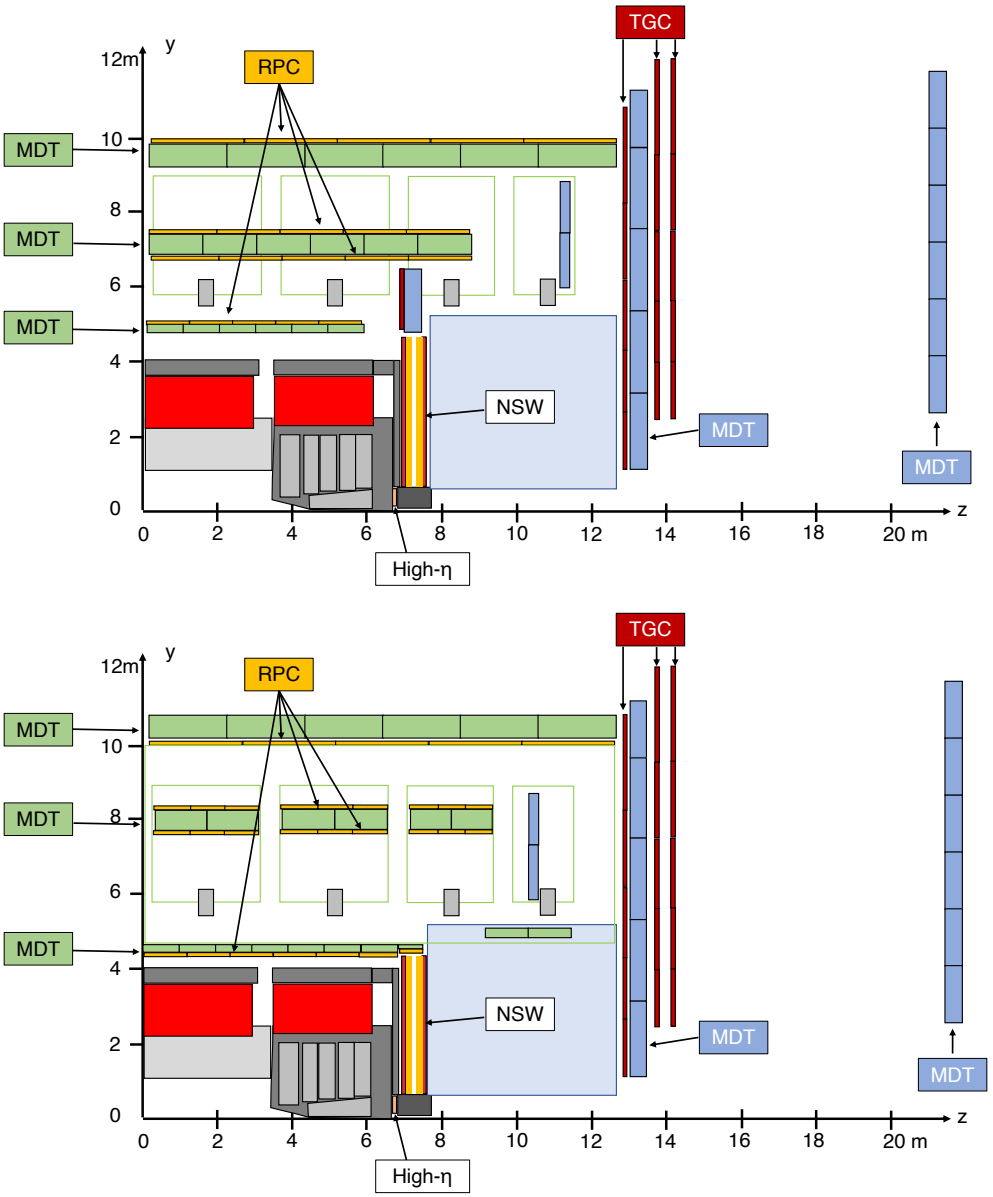

Fig. 2.24 Sectional view of the ATLAS Muon detector of the Large (top) sector and the Small (bottom) sector in the HL-LHC.

2.3.4 Phase II Upgrade of the Muon Trigger System

After the Phase-II upgrade, the trigger system of the ATLAS detector will be renewed. The trigger will consist of a hardware-based Level-0 (L0) trigger and a software-based Event Filter (EF) as shown in Fig. 2.25. The maximum trigger rate for the L0 trigger is 1 MHz and 10 kHz for the EF. With the upgraded readout electronics and larger buffers, the latency that can used for the L0 trigger is 10 μs instead of 2.5 μs. The extension of latency means that the first level trigger system can use information from more detectors and more sophisticated algorithms. Especially for the muon trigger system, information from all muon detectors and additional help from the tile calorimeter are used for event selection based on p_{T} estimation.

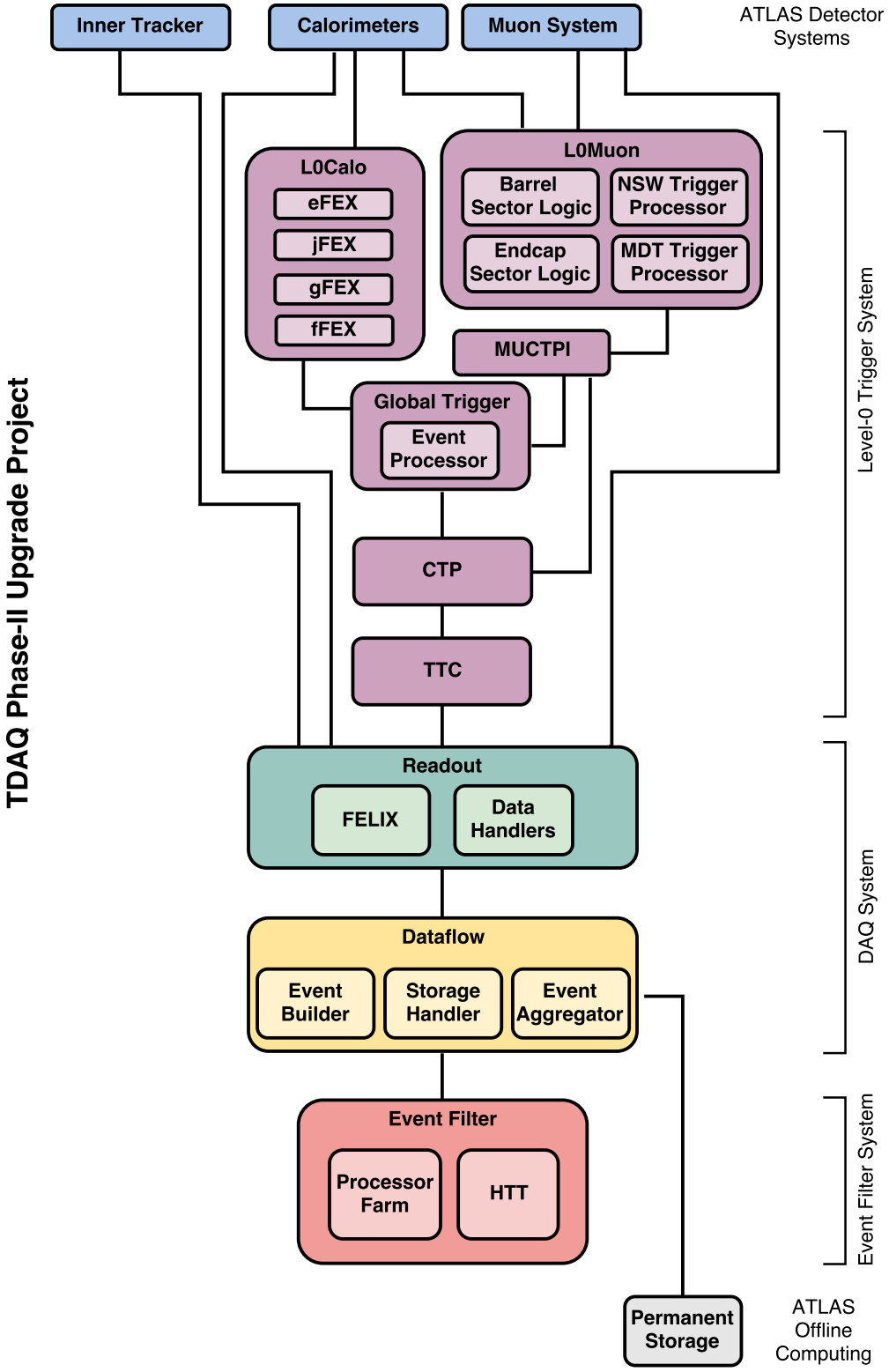

Fig. 2.25 Trigger system of the ATLAS detector after the Phase-II upgrade. New components like Global Trigger and Trigger, Timing, and Control system (TTC) are added in the first level trigger system [25].

Fig. 2.26 shows the structure of the L0 Muon trigger. At the first step, the RPC trigger or the TGC trigger fires to make an RoI for hit extraction for the trigger using MDT information. The MDT trigger then conducts a quick reconstruction of muon segments and returns an estimated p_{T} to the sector logic. The information of the energy deposit in the tile calorimeter is used to reduce trigger rate caused by fake muons, since the high energy muons also slightly ionise atoms in the calorimeter. In the endcap region, information of segments reconstructed by the NSW and hits from RPC installed in the small sectors which cover the EE region are also used for the trigger decision. The candidates of muon tracks are the sent to the L0 MUCTPI to resolve the overlap and then passed to the EF for further processing.

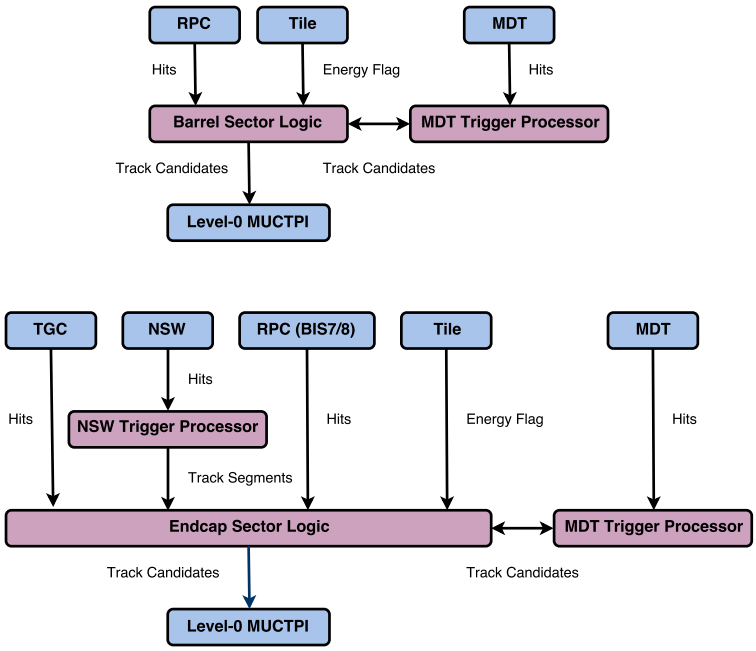

Fig. 2.26 Structure of L0 Muon trigger in the barrel region (top) and the in the endcap region (bottom). [25]

The new RPC trigger and the TGC trigger abolish the pivot layer and can be fired with seed from all layers. With the newly added RPC layers in the inner station RPC0, following coincidence conditions are considered to be used in the new RPC trigger.

- at least 3 out of 4 hits in the RPC1 and RPC2 with at least 1 hit in the RPC3. The same as the current RPC trigger coincidence condition but can start from the RPC1 or RPC3 for there is no priority for the RPC2.
- at least 2 out of 3 hits in the RPC 0 with 3 out of 6 hits in RPC1, RPC2, and RPC3.
- at least 2 out of 3 hits in the RPC 0 with at least 1 hit in the RPC3.

If all of these conditions are implemented in the online operation, the acceptance for muon events in the barrel region will be increased from 78% to 92%.

The new TGC trigger applies a method of matching hit patterns for quick TGC track segment reconstruction in the middle station. The track segment can be reconstructed in an angular resolution of 4 mrad. The concept of the new TGC trigger is shown in Fig. 2.27. With the segments reconstructed in the NSW, a MuonSA like new TGC trigger can be realised in the region $1.3 < |\eta| < 2.4$. In the region $1.05 < |\eta| < 1.3$, the p_{T} will be estimated with combination between the TGC track segment and the hits in the inner station TGC (or the barrel RPC cover this region) and the energy tag from the tile calorimeter.

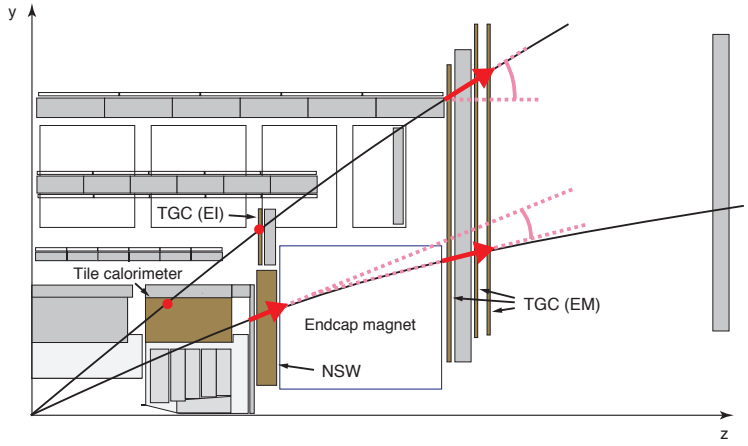

Fig. 2.27 Concept of new TGC trigger with track segment reconstruction in the middle station. Shown in large sector. [25]

The segments reconstructed by the NSW are required to pass the NSW trigger. The NSW trigger will be built into the muon trigger system in the Phase I upgrade. The NSW trigger rejects segments that are not created by the muons produced at the interaction point, as shown in Fig. 2.28. With the restriction of the NSW trigger, the number of segments reconstructed in the endcap inner station is limited to a reasonable amount, which also saves time for segment matching in the new TGC trigger.

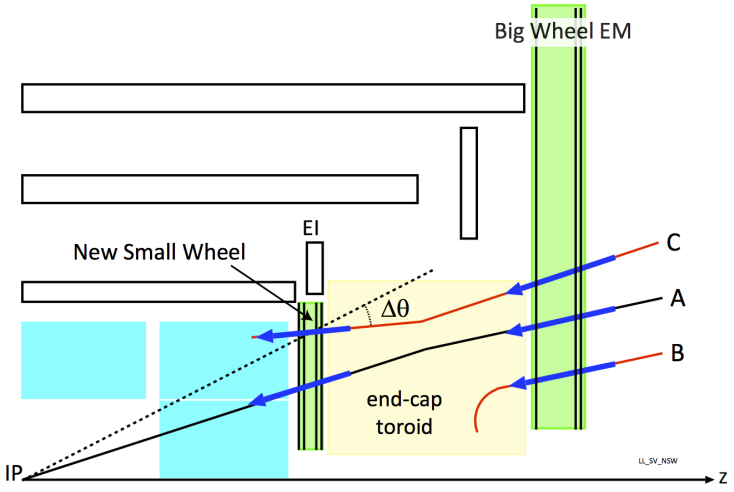

Fig. 2.28 Concept of the NSW trigger [40]. Segments with direction not pointing to the interaction point will be rejected.

Other than the triggers described above, a completely new muon trigger to be added in the Phase II upgrade is the MDT trigger. The MDT trigger is proposed aiming to achieve a high p_{T} resolution at the first level trigger. The RoIs issued by the TGC/RPC trigger is necessary for the MDT trigger to reconstruct muon segments in the MDT detector. The MDT trigger selects muons using parameters correlated to the curvature radius of muon track. Some of the parameters are currently used for the MuonSA software trigger. In some degrees, the MDT muon trigger is to implement a hardware-based MuonSA algorithm.

- α: The difference between the direction of the segment and the zenith angle corresponding

to the segment η.

- β: The difference between the directions of segments in different MDT stations.
- sagitta: The distance in z-coordinate between the Middle station segment and the corresponding point on the line connecting the segments in the Inner station and the Outer station.

The concept of the parameters is shown in Fig. 2.29. This thesis will describe the MDT trigger using segments reconstructed using Associative Memory. The details of the MDT trigger will be shown in the next chapter.

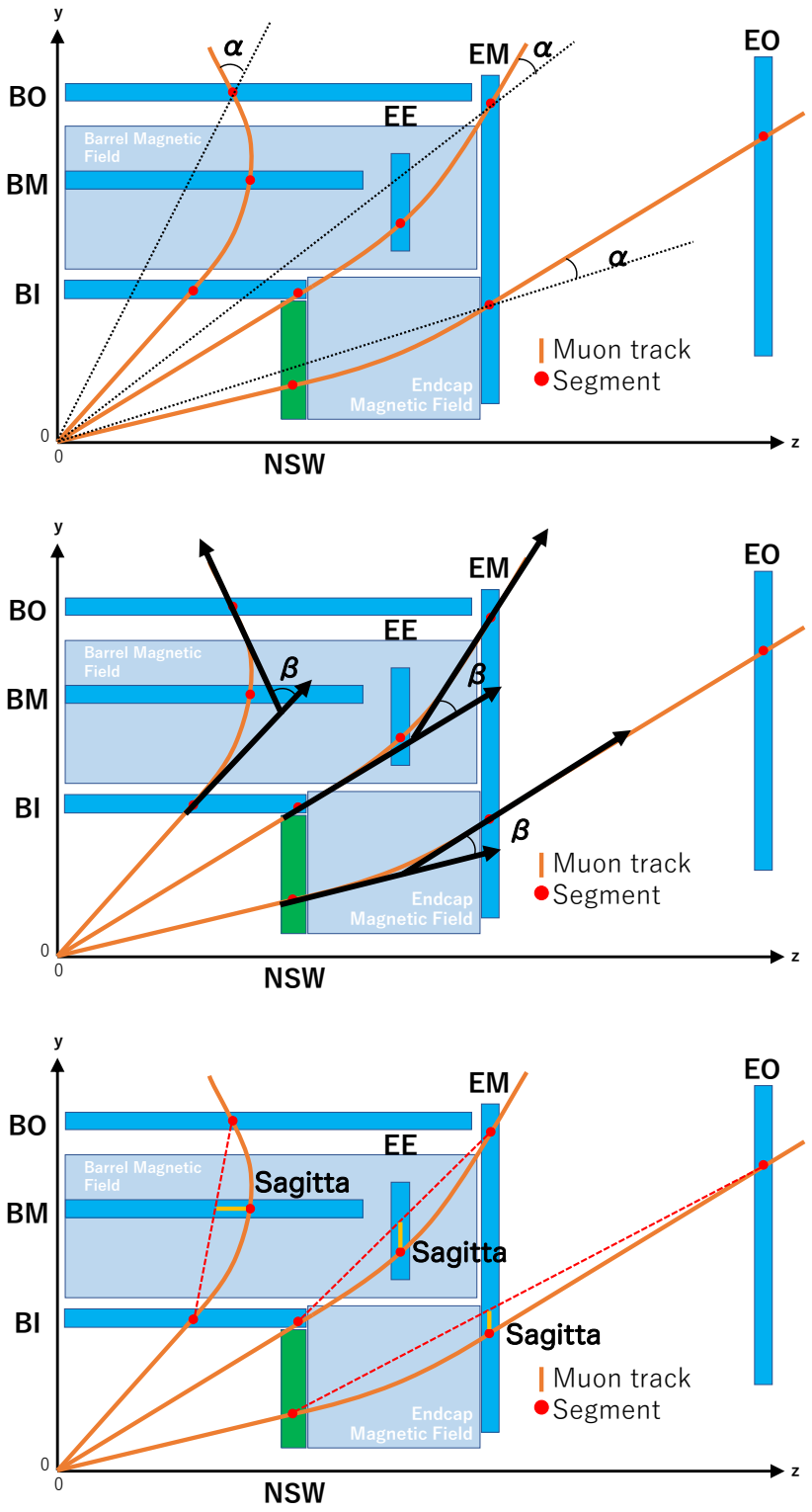

Fig. 2.29 The concept of the MDT trigger using parameter α (Top), β (Middle), and sagitta (Bottom).

Chapter 3

MDT Muon Trigger with Associative Memory

3.1 MDT Muon Trigger for the ATLAS Experiment at HL-LHC

The MDT trigger is an essential part of the L0 muon trigger for the ATLAS experiment at HL-LHC. The purpose of introducing the new hardware muon trigger using the information given by the MDT detector is to make a more precise muon selection at the L0 trigger and to maintain the trigger rate at an acceptable level in the high luminosity environment.

As mentioned in the previous section, the hit information from the MDT has a much higher spatial resolution than TGC and RPC designed for the triggering purpose. The muon segments with more precise spatial and angular information can provide a more accurate estimation of the muon transverse momentum p_{T}. The reconstruction of the MDT segments requires hits in the MDT tubes on a straight line that matches the direction indicated by the RPC and TGC hits. The requirement makes the muon trigger more robust to the accidental coincidence caused by the noise hits and results in a mitigation of the trigger rate increase.

In the L0 muon trigger system of the ATLAS detector at HL-LHC, the process of the MDT trigger will start when the muon track candidate created by the RPC trigger or the TGC trigger arrives the MDT processor. The output of the MDT trigger is sent to the sector logic, as shown in Fig. 2.26. The candidate arrives 1.675 μs after the bunch crossing, and the latency of the arrival of the MDT candidate to the sector logic is 3.810 μs [25]. Therefore the MDT trigger must reconstruct the muon segments and estimate the muon p_{T} in about 2.2 μs.

To quickly reconstruct the muon segments in the MDT trigger, we proposed to use the Associative Memory (AM) for the segment reconstruction. Then reconstruction of the muon track will be performed in an FPGA to estimate the muon p_{T}. The AM is a special kind of memory that can be used for quick matching between input data with saved patterns which are prepared in advance. Other groups in the ATLAS experiment also suggested pure FPGA-based methods [25].

3.2 Associative Memory

The Associative Memory is implemented on silicon as a CMOS VLSI chip that can be fully-customised. The devices as so called "AMchip" is made of sets of content addressable memories (CAM). The patterns of data are stored as pre-saved RAM words in the CAM sets. Input data from the detectors flow through the AMchip and will be compared with the patterns bit by bit. The AMchip conducts the comparison in parallel for each pre-stored pattern [45]. If any pattern is found the same as the input data, a matched signal will be fired, and the AMchip will output the pattern ID.

The list of patterns is called pattern bank, and the size of the pattern bank is strictly limited by the size of and the technology used by the AMchip. Very early generation AMchips can store only about 512 patterns [45]. After long-time development, the bank size increased to 12k[*1] for the newest mass-production type AMchip, and a new type of AMchip that can contain 3×128k patterns is under development [46].

The patterns stored in the AMchips are designed according to the data format of detectors. The precision of the pattern can be adjusted according to the demand. The matching of patterns and data also can be required from a perfect match or a partial match by changing the work mode of the AMchip.

3.3 Design of AM-MDT Muon Trigger

3.3.1 Overview of AM-MDT Muon Trigger

The MDT Muon Trigger with Associative Memory, which is also called the AM-MDT Muon Trigger, uses AMchips for muon segment reconstruction. Fig. 3.1 shows the basic concept of the AM-MDT Muon Trigger. The process starts when a candidate from RPC or TGC arrives. The MDT tube hits in the RoI region are read out and sent to the AMchips. In the AMchips, patterns defined as the combinations of MDT tube indicies and the drift radius in each tube are pre-stored based on a huge number of simulated muon tracks with ideal geometry of the detector. Then, the AMchip compares the input hits with all pre-stored patterns and outputs the pattern ID of matched patterns. The information associated with the matched patterns will also be read out from a pre-stored list mapped with respect to the pattern ID. The main information associated with patterns includes the position and the direction of the muon segment corresponding to the pattern that can be used for muon track reconstruction.

Once the pattern matching is over, the information is sent to the FPGA for muon track reconstruction and trigger decision. The FPGA gathers outputs from AMchips of all three MDT stations and tries to calculate parameters of α, β, and sagitta with the reconstructed muon segments. Then the calculated parameters are compared with the thresholds corresponding to the muon p_{T} threshold, which are obtained with simulation samples in advance. The result of the comparison is used for deciding the muon track to be passed or discarded by the MDT muon trigger. If the muon track passes the decision, an estimate of p_{T} is processed using the parameters.

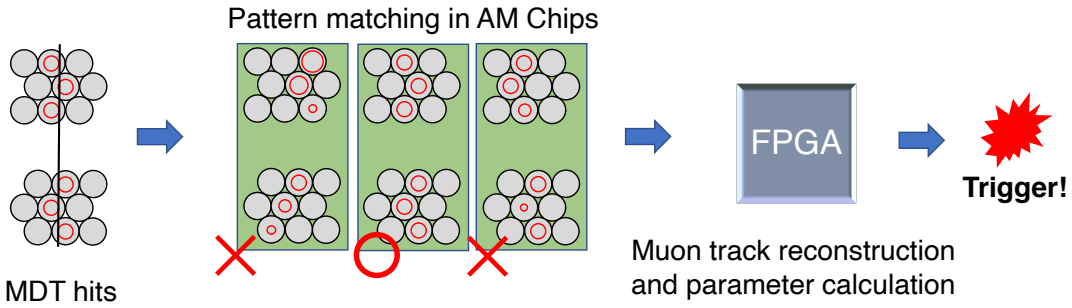

Fig. 3.1 The concept of the AM-MDT Muon Trigger. The information associated with the matched pattern is sent to the FPGA and then processed to calculate the parameters used for the selection of muons.

The information of the reconstructed muon track will be sent back to the sector logic and

[*1] With the configuration 1 pattern = 16 bit $\times$ 8words

then passed to the MUCTPI. The p_{T} calculated by the AM-MDT Muon Trigger would be used in the following software-based trigger processes when the muon track candidate passes the L0 trigger.

3.3.2 Pattern Definition and Bank Generation for Associative Memory

The patterns used by the AM-MDT Muon Trigger are made of hit information from MDT tubes. Each pattern contains six hits, and one hit is represented with 16 bit as shown in Table 3.1. Ten bits are used to represent the tube number, four bits are used to define the drift radius and one sign bit is used for the determination of which side the muon passed. As the radius of the MDT tubes is 15 mm, the drift radius is represented in 1 mm binning. The definition of the hit information is shown in Fig. 3.2. For each pattern, only one hit is stored in each MDT layer, and if the muon leaves more than one hits in an MDT layer, the hit in the tube with larger $|\eta|$ will be selected as the layer's hit for this pattern. It allows to prevent storing duplicating patterns.

The pattern bank is generated by training using the hit information of MDT tubes in a Monte Carlo simulation sample of single muon particle gun. The training sample contains 290M muons that are uniformly distributed in the region of $|\eta| < 2.5$. The p_{T} distribution of the muons is flat in $\frac{1}{p_{\mathrm{T}}}$ in p_{T} region the 6-500 GeV.

Description	Spare	Tube Channel Number	Sign	Drift Radius
Number of bits	1	10	1	4

Table 3.1 The usage of bits for hits information contained in the patterns.

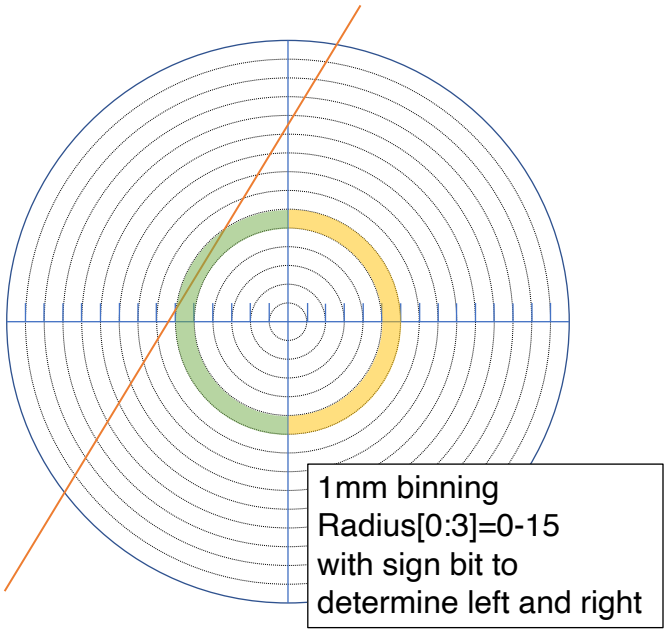

Fig. 3.2 Definition of the hit information. The muon track shown in this figure leaves a hit at 5 mm at left side.

The original pattern banks generated with the Monte Carlo sample have a huge bank size due to the precise binning of the drift radius. To store the pattern banks in the AMchips used for the AM-MDT Muon Trigger, we have to reduce the bank size while maintaining the precision of patterns at a high level. Therefore, Don't Care (DC) bits are introduced in the patterns. Technically, the DC bits are ternary bits in the patterns that always give a matched result regardless of the input data. With the optimisation of the DC bits, the precision of the drift radius binning can be adjusted pattern by pattern and layer by layer. The DC bits are activated from the least significant bits of the pattern. For example, two patterns can have the same hit information in five layers, but different drift radius in the last tube by only 1 mm. In such a case, the choice of either pattern has no large impact on the precision of the reconstructed segments. Then a DC bit will be activated to the last layer to change the binning into 2 mm. With the new rough binning, the two patterns are completely the same so that they can be merged into one pattern to reduce the bank size.

The number of DC bits is limited to two in each MDT layer. Only bits representing the drift radius can be activated as DC bits, and DC bits in the tube number is not allowed since no pattern can match with hits from different tubes in one MDT layer. In pattern level, the limits on the number of DC bits is decided on the smallest number that makes the bank size fits the storage capacity of the AMchips. Not all the patterns in the banks have DC bits activated, for example, when the limit on the number of DC bits is two, the bank contains patterns with two DC bits, with only one DC bit and with no DC bit. According to the basic hardware design of the AM-MDT Muon Trigger, the storage capacity of patterns is 800k for the Inner Station and the Middle Station and 1600k for the Outer Station. From the results of the dependency test of the number of DC bits for the bank size, patterns in the bank of the Inner Station can have two or fewer DC bits, and in the case of the Middle Station and the Outer Station, the limit is 11 DC bits, as shown in Fig. 3.3.

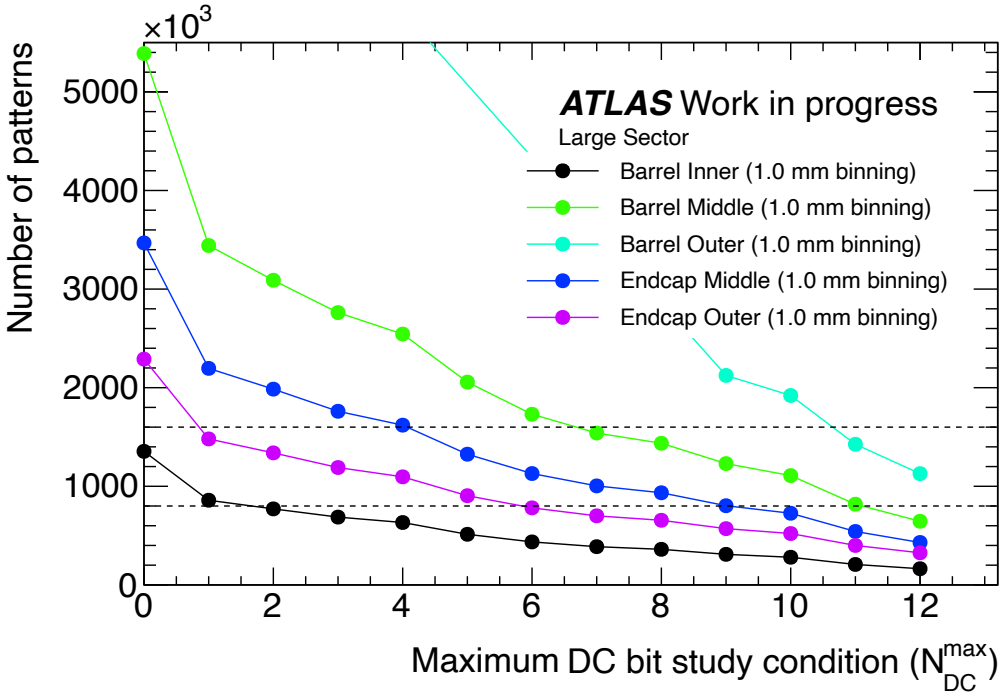

Fig. 3.3 Dependency on the number of DC bits of the bank size in the Large Sector. The 800k and 1600k storage capacities of AM chips are shown in dashed lines. The numeber of patterns in each station with no DC bit are proportional to the number of MDT tubes.

Barrel Inner		Barrel Middle		Barrel Outer	
Sector	Number of Patterns	Sector	Number of Patterns	Sector	Number of Patterns
1	770853	1	818222	1	1426306
2	504702	2	612138	2	1428449
3	765278	3	821680	3	1427864
4	512500	4	614993	4	1435061
5	801401	5	804597	5	1406094
6	504328	6	616034	6	1436506
7	733737	7	758602	7	1352641
8	478868	8	612063	8	1357614
9	743749	9	761175	9	1351073
10	465454	10	612287	10	1432393
11	special sector	11	special sector	11	special sector
12	special sector	12	special sector	12	special sector
13	713902	13	657058	13	1224128
14	special sector	14	special sector	14	special sector
15	special sector	15	special sector	15	special sector
16	474459	16	606440	16	1418384

Table 3.2 List of bank size after DC bits activated. The banks shown in the list are for A-side of the barrel region.

By activating the DC bits to the original generated pattern banks, the bank sizes are significantly reduced. The sizes of banks used for the performance test that will be described in the following chapters are summarized in Table 3.2. The banks of the special sectors are not generated yet. Since this thesis focuses on the AM-MDT muon trigger in A-side of the barrel region, the banks shown in Table 3.2 are for A-side of the barrel region only. As the ATLAS detector is symmetric in A-side and C-side, the bank sizes for C-side are considered similar to the numbers shown here. From Table 3.2, we can find that the current configuration of the number of DC bits is still sub-optimal. The small sectors of the Inner Station can store more patterns, which means a higher accuracy of pattern matching can be achieved in these sectors. Meanwhile, some sectors of the Middle Station and sector 5 of the Inner Station still have a bank size that exceeds the storage capacity of the AMchips. The little excess of the bank size can be resolved by dropping the least often matched patterns. With the consideration of the future development of the AMchip, the current banks are possible to fit into the storage capacities and we used these banks for the performance tests.

The information necessary for muon segment reconstruction is stored together with the corresponding patterns. The information includes the position of the segment in $\eta - \phi$ coordinate, the representing direction of the pattern. The gradient and intercept of the muon track are also stored by assuming the track can be considered straight in the MDT stations. This information is acquired from muon segments reconstructed with the offline algorithm in the training Monte Carlo sample.

3.3.3 Reconstruction of Muon Trajectory

The reconstruction of muon trajectories in the AMchips uses the outputs of information associated with the matched patterns. The minimum requirement of pattern matching is four out of six hits match with the input data. Three groups of AMchips work parallel for each MDT station and require a full match (six-out-of-six match), a five-out-of-six match and a four-out-of-six match respectively. The results of the full match group are read out with the highest priority.

Only when no pattern was found in the full match group, the outputs of the five-out-of-six group are read out and the four-out-of-six group is the last. Once the pattern matching process is over, the information of the matched pattern is read out in the order of the number of matched hits.

The muon segments are reconstructed using the pre-stored information associated with the matched patterns. The positions of the segments in R-z plane[*2] are calculated using the stored gradient and intercept of muon tracks, and the direction of the segments directly uses the stored representing direction. Another option is performing a χ^2-fitting to obtain more accurate information of segments. However, additional processing time in the FPGA is needed. By comparing the two options, we found that the first option has sufficient performance of segment reconstruction as follows.

The performance of segment reconstruction is tested with a Monte Carlo sample that reproduces the high-luminosity environment. The pattern banks described in the previous section show an excellent reconstruction efficiency and good angular and spatial resolution with respect to the results of offline reconstruction. The results are shown in Table 3.3, and the details can be confirmed in Appendix A. The best angular resolution is better than 1 mrad, and the best spatial resolution is only 0.2 mm.

	Barrel Inner		Barrel Middle		Barrel Outer	
	Large	Small	Large	Small	Large	Small
Angular Resolution [mrad]	0.956	1.945	1.659	2.410	1.510	1.575
Spatial Resolution [μm]	200.532	230.990	363.509	367.115	369.872	371.989

Table 3.3 Angular and spatial resolution of the banks after DC bits activated.

Before the parameter calculation of muon track, a matching with the RoI issued by the TGC/RPC trigger is performed. The matching windows are defined with conditions of $\Delta\eta, \Delta\phi$ and ΔR ($\Delta R = \sqrt{\Delta\eta^2 + \Delta\phi^2}$). The shape of matching windows is shown in Fig. 3.4, and the conditions are summarized in Table 3.4. The cut values of each condition are decided using single muon particle gun Monte Carlo samples. When more than one segments are found in the matching window, all the matched segments is sent to the FPGA for parameter calculations. In the hardware implementation, a hit extraction algorithm will be used instead of the matching. The hit extraction algorithm specifies a set of MDT tubes for the segment reconstruction. Then the information of hits is sent to the AMchips and the segment are reconstructed using the patterns matched in the AMchips.

After the segment reconstruction, the AM-MDT Muon Trigger checks in which MDT station the reconstructed segments exist. Depending on the number of stations that have segments found, different parameters are used in the momentum estimation. The parameters used for muon selection include two αs ($\alpha_{\rm mid}, \alpha_{\rm out}$), three βs ($\beta_{\rm IO}, \beta_{\rm IM}, \beta_{\rm MO}$) and a sagitta, as described in Chapter 2. $\alpha_{\rm in}$ is not calculable because no toroidal magnetic field exists between the interaction point and the Inner Station. All the calculable parameters are calculated for the RoIs. For example, if an RoI matches with segments in all three MDT stations, all the six parameters are calculated, and if an RoI matches with segments in the Inner Station and the Middle Station, then only $\beta_{\rm IM}$ and $\alpha_{\rm mid}$ are calculated. Estimated $p_{\rm T}$ that is corresponding to the parameters will also be given. The method of calculation is described in the following sections.

The calculated parameters are compared with the corresponding thresholds, respectively. The AM-MDT Muon Trigger sorts calculated parameters in a prioritised list. The trigger decision made by the highest priority parameter is used as the final decision. The sagitta has the highest priority, in other words, the trigger decision made by sagitta is the final decision when

[*2] Since the MDT detector has no ϕ resolution of hits, the ϕ information is accompanied with a large uncertainty.

sagitta is usable. The priority is then followed by β_{IO}, β_{IM}, β_{MO}, α_{out} and α_{mid} in the order of p_{T} resolution. Only when the parameters with higher priorities are not available due to the segment combination in the parameter calculation, the trigger decision made by parameters with the next highest priority is used.

When one RoI is decided to pass the AM-MDT Muon Trigger, the information of reconstructed muon track is sent back to the sector logic. The information includes the η and ϕ of the RoI, the information of calculated parameters and segments used for the parameter calculation, and the estimated p_{T} calculated with the parameters. The calculation of the p_{T} will be described in the next section. In the case that an RoI failed to pass the AM-MDT Muon Trigger, a signal is also sent back to the sector logic as a notification of no corresponding muon track of the RoI with p_{T} larger than the p_{T} threshold.

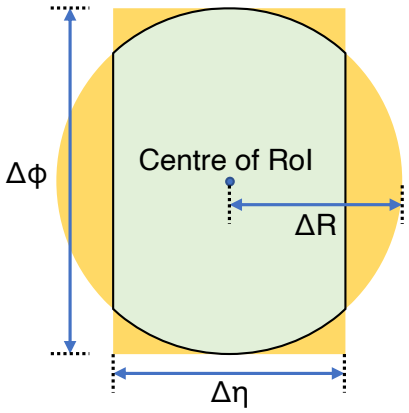

Fig. 3.4 The shape of the window for matching between the RoI and reconstructed muon segments. Only segments in the region that meet $\Delta\eta$, $\Delta\phi$ and ΔR conditions will be used for muon track reconstruction.

Station	$\Delta\eta$	$\Delta\phi$	ΔR
Inner	0.11	0.30	0.30
Middle	0.13	0.30	0.30
Outer	0.15	0.30	0.30

Table 3.4 The cut value of $\Delta\eta$, $\Delta\phi$ and ΔR in each station.

3.3.4 p_{T} Calculation with parameter α, β and sagitta (s)

As described at the end of chapter 2, the MDT muon trigger uses three parameters correlated to the curvature radius of the muon track to select muons. Fig. 2.29 shows the concept of the three parameters α, β and sagitta (s).

According to the equation of the Lorentz Force, the curvature radius of the muon track inside a constant magnetic field is proportional to the muon momentum component that is perpendicular to the magnetic field. The transverse momentum p_{T} can be directly transformed from the momentum of muon when the zenith angle θ is given. Therefore the p_{T} of the muon is proportional to the curvature radius of muon.

In Fig. 3.5, the relations between the parameters and the curvature radius of the muon track are shown. Parameter β is the easiest to understand. Under the assumption that the muon trajectory is a part of a circle, the concentric angle corresponding to arc AB is equal to β, as shown in Fig. 3.5 (a). When the length of arc AB is Δs, the relation between the curvature

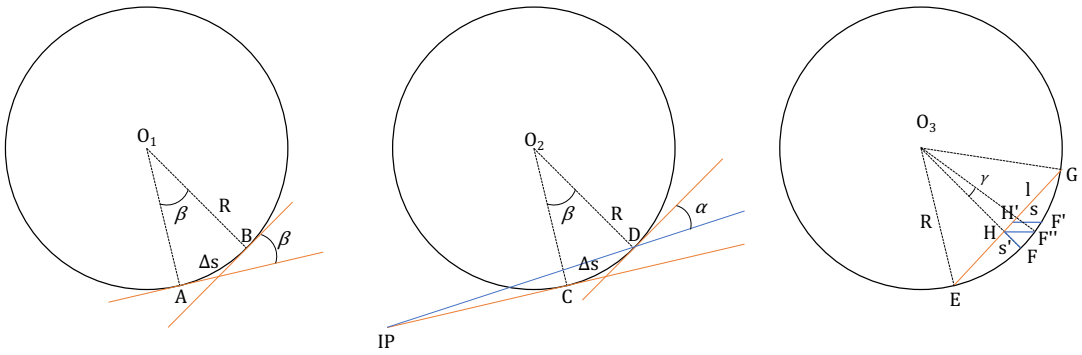

(a) β-R relation (b) α-R relation (c) sagitta(s)-R relation

Fig. 3.5 The relation between the curvature radius of the muon track and parameters.

radius R and parameter β can be written as Eq. (3.1). Therefore the parameter β is inversely proportional to the curvature radius R.

$$\beta = \frac{\Delta s}{R} \tag{3.1}$$

If segments are reconstructed only in the Middle or Outer MDT station, with an auxiliary line start from the interaction point (IP)[*3], the parameter α can be calculated, as shown in Fig. 3.5 (b). Also, under the assumption that the muon trajectory is a circle, the opening angle of points C and D from IP is $\beta - \alpha$. Assuming the muon trajectory is linear from the IP to the Inner Station, and requiring a smooth connection between the curvature and the linear trajectory with the consideration of tangential direction at point C, we can uniquely determine the point C in the Inner Station. In this case, the value of β can be directly determined by adding a constant to the value α, and the relation between the parameter α and the curvature radius R can be written as Eq. (3.2).

$$\alpha = \frac{\Delta s}{R} + \text{Const.} \tag{3.2}$$

The parameter sagitta s is a little more complicated than α and β. As shown in Fig. 3.5 (c), according to the mathematical definition, the mathematical saigtta s' is given by the curvature radius R and the half-length of string EG l.

$$s' = R - \sqrt{R^2 - l^2} \tag{3.3}$$

Since the muons produced in the collisions have large momentum, the sagitta is much smaller compared to the curvature radius of muon track. As an approximation, the relation between the mathematical sagitta s' and the curvature radius R can be written as Eq. (3.4).

$$s' \approx \frac{l^2}{2R} \tag{3.4}$$

However, the position corresponding to the muon segment in the Middle station is not at the point F where is the middle point of string EG but point F' where slightly displaced from the point F. Thus the sagitta calculated by the AM-MDT Muon Trigger will be s instead of s'. When the relation of Eq. (3.4) is established, the length of arc FF' is also much smaller than

[*3] The direction of the solenoidal magnetic field is perpendicular to the $R-z$ plane, so the muon trajectories from the IP to the Inner station can be considered as a straight line.

the circumference and can be approximated to a straight line. Then by shifting H'F' to HF", the relation between s and s' is given by Eq. (3.5).

$$\begin{aligned} s^2 &= R^2 + (R - s')^2 - 2R(R - s')\cos\gamma \\ &= R^2 + (R^2 - l^2) - 2R\sqrt{R^2 - l^2}\cos\gamma \\ &= s'^2 + 2R\sqrt{R^2 - l^2}(1 - \cos\gamma) \end{aligned} \tag{3.5}$$

Since $1 \gg \gamma$ when FF" is much smaller than the circumference, $\cos\gamma$ is approximately 1, and the relation $s \approx s'$ is established. As a result, the sagitta (s) measured by the AM-MDT Muon Trigger can be used as a substitute for the mathematical sagitta.

Thus, all the three types of parameters used by the AM-MDT Muon trigger are inversely proportional to the curvature radius R, or namely proportional to the transverse momentum inverse $1/p_{\mathrm{T}}$.

In the algorithm implemented in the AM-DT Muon Trigger, the parameters should be calculated with the information output from the AMchips. The parameter α and the parameter β are calculated by subtraction between the angle information of matched patterns. The parameter sagitta (s) is calculated with the positions of segments in the R-z plane. Eq. (3.6) is the formula to calculate sagitta (s) with the information of reconstructed segments.

$$s = (z_{\mathrm{out}} - z_{\mathrm{in}}) \times \frac{R_{\mathrm{mid}} - R_{\mathrm{in}}}{R_{\mathrm{out}} - R_{\mathrm{in}}} + z_{\mathrm{in}} - z_{\mathrm{mid}} \tag{3.6}$$

$z_{\mathrm{in}}, z_{\mathrm{mid}}, z_{\mathrm{out}}, R_{\mathrm{in}}, R_{\mathrm{mid}}, R_{\mathrm{out}}$ are the z coordinate and R coordinate of the reconstructed segments in the R-z plane corresponding to the sector that the input RoI exists.

Furthermore, the correlation of the parameters and $1/p_{\mathrm{T}}$ has a strong dependence on η and ϕ of the RoIs. Considering the octant structure of the ATLAS magnetic field and the overlap between the MDT detectors in different sectors, we divided the η-ϕ plane into small regions with the consideration of the combination of segments in different sectors, instead directly applying η and ϕ correction to the calculated parameter. The plan of region division is shown in Fig. 3.6. The ϕ direction is divided equally into 80 regions, and the 80 bins are regrouped into 5 groups of ϕ. The ϕ groups are shown in different colour in Fig. 3.6 (b). Two ϕ groups cover the overlap region and are defined separately for the large sectors and small sectors. The input RoIs are classified with the region that the RoIs belongs to. In the case of the RoIs in the overlap region, the sectorID given by the TGC/RPC trigger are used to determine which sector the RoIs belong to. As a result, 42 regions ($6\eta \times 7\phi$) are defined for barrel A-side. The region division is symmetric for the A-side and C-side. The expression of relation between the parameters and $1/p_{\mathrm{T}}$ is investigated region-by-region for all the regions.

Additional conditions are required for the calculation of parameter β and s. From the relation between parameter α and β shown in Fig. 3.5 (b), the opening angle looking from the interaction point is correlated with parameter β. The opening angle can be expressed by $\Delta\eta$ between segments in different MDT stations. Consequently, a linear correlation between the parameter β and the $\Delta\eta$ is expected, and wrong combinations of segments tend to deviate from the line. Hence, the correlation between the parameter β and the $\Delta\eta$ can be used to determine the correct combination of reconstructed segments for the parameter calculation. Fig. 3.7 shows an example of the band cut in one of the η-ϕ regions. Parameter β that has β-$\Delta\eta$ pair outside the band will be discarded as an invalid result. The distributions shown in Fig. 3.7 are calculated using Monte Carlo samples, using reference to the correct segment combination. The widths of the band are determined region by region.

Since it is naturally possible to calculate all the three β's in the calculation of s, all the three β's are required to be valid. This requirement ensures that the three segments belong to the same muon track, and prevents the from accidentally matching with segments in three stations from using parameter s for the trigger decision.

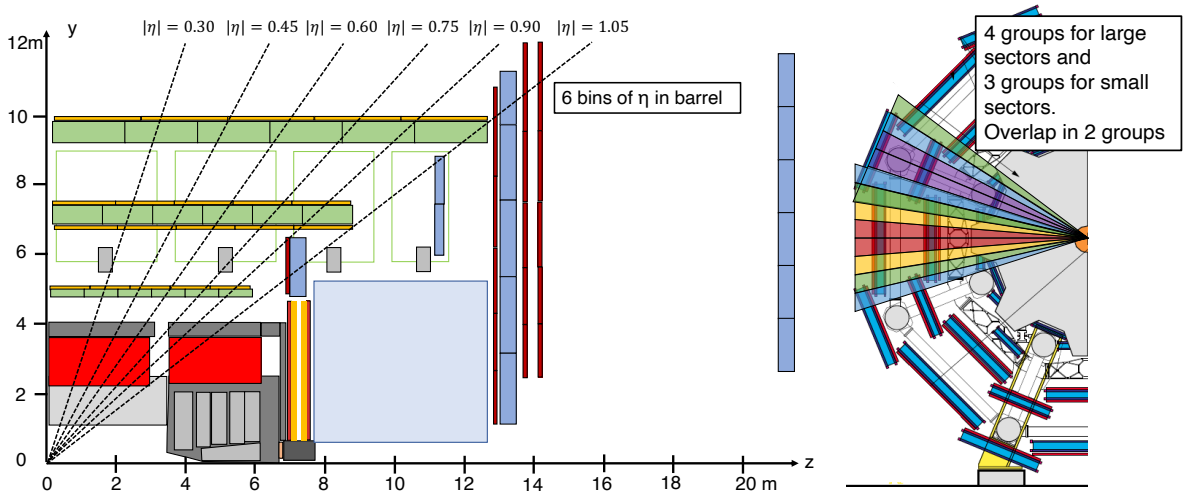

(a) (b)

Fig. 3.6 The binning of η (a) and ϕ (b) in the barrel region. Five ϕ groups are defined and in two of the ϕ groups (green and blue), overlap between the large sector and the small sector exists. The ϕ groups in the overlap region are redefined separately for the large sectors and the small sectors.

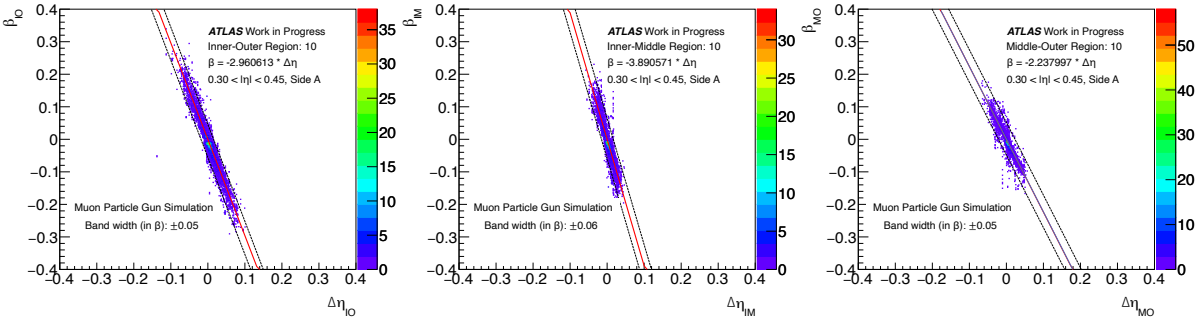

(a) Inner-Outer (b) Inner-Middle (c) Middle-Outer

Fig. 3.7 The approximately linear correlation between parameter β and the $\Delta\eta$ of segments in different MDT stations in one of the defined regions. Only parameters calculated with correct segment combination are shown. The red lines in the figures show the result of fitting and the black lines show the border of the band. Pairs of β with $\Delta\eta$ which are outside the band will not be used.

The parameter-$1/p_{\mathrm{T}}$ distributions are checked using single muon particle gun Monte Carlo samples flat in η, ϕ and p_{T} from 3 GeV to 100 GeV. When more than one segment combinations are available for one parameter, the combination giving smaller parameter will be used according to a maximum efficiency strategy. From the results shown in Fig. 3.8, strong correlations are confirmed between the parameters and $1/p_{\mathrm{T}}$, which means that all the parameters can be used for muon selection. Two arms of the distributions are corresponding to muons with plus and minus charges. In the low-p_{T} region, some higher-order effects can be observed, but do not influence the trigger performance where the p_{T} threshold is set to 10 GeV.

After the calculation of parameters, a conversion from the parameters to the corresponding p_{T} is conducted. The parametrisation of p_{T} is based on a large amount of data in single muon particle gun Monte Carlo samples. The results of pattern matching with AMchips are not used, but the offline information of muon tracks is directly used. The direction and the position

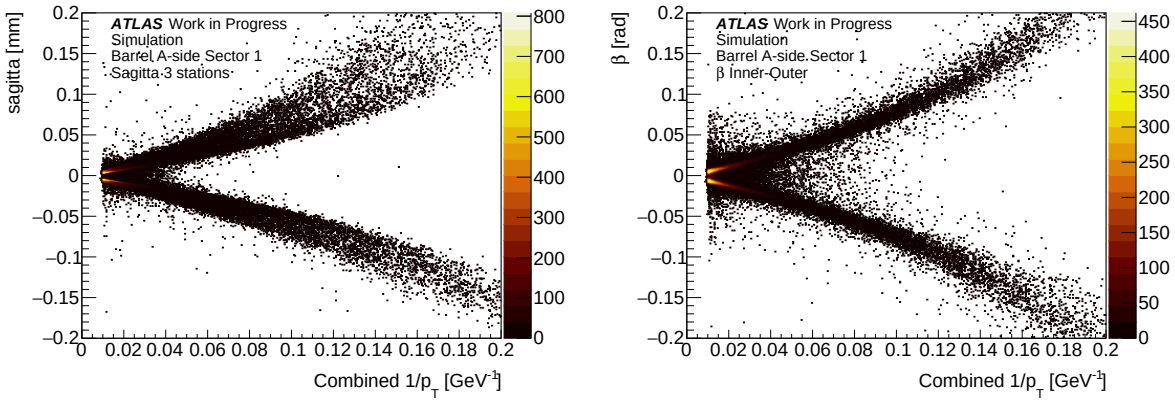

(a) sagitta (s)

(b) β_{IO}

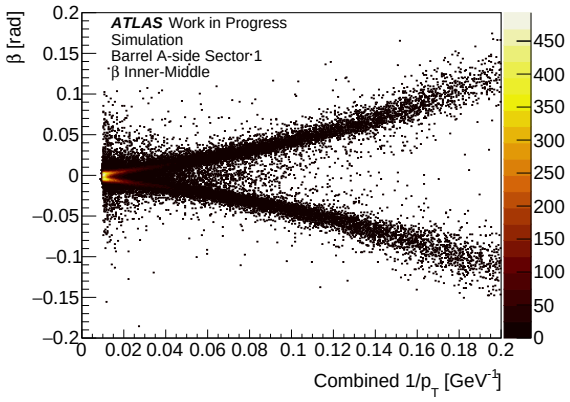

(c) β_{IM}

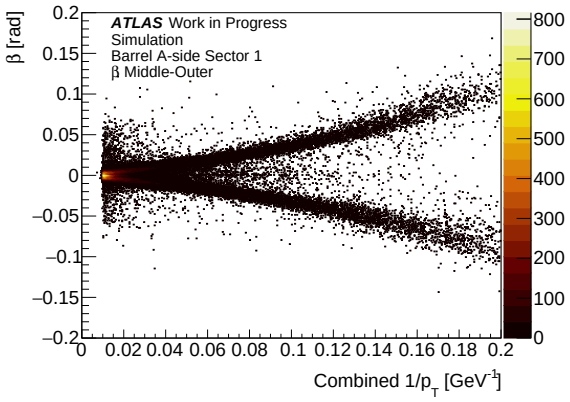

(d) β_{MO}

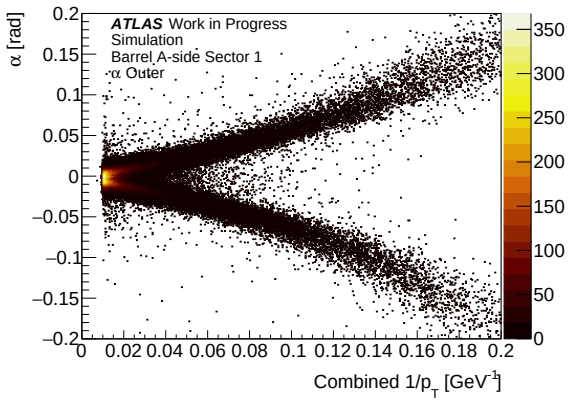

(e) α_{out}

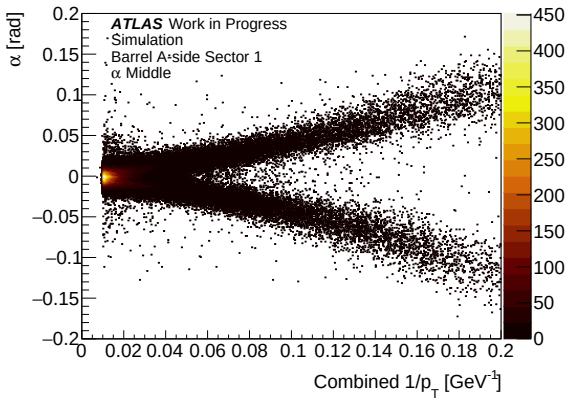

(f) α_{mid}

Fig. 3.8 Relations between online parameters and $1/p_{\mathrm{T}}$ estimated with offline muons. The distributions are inclusive distributions of one sector. The sign of the parameters indicates the charge of muons.

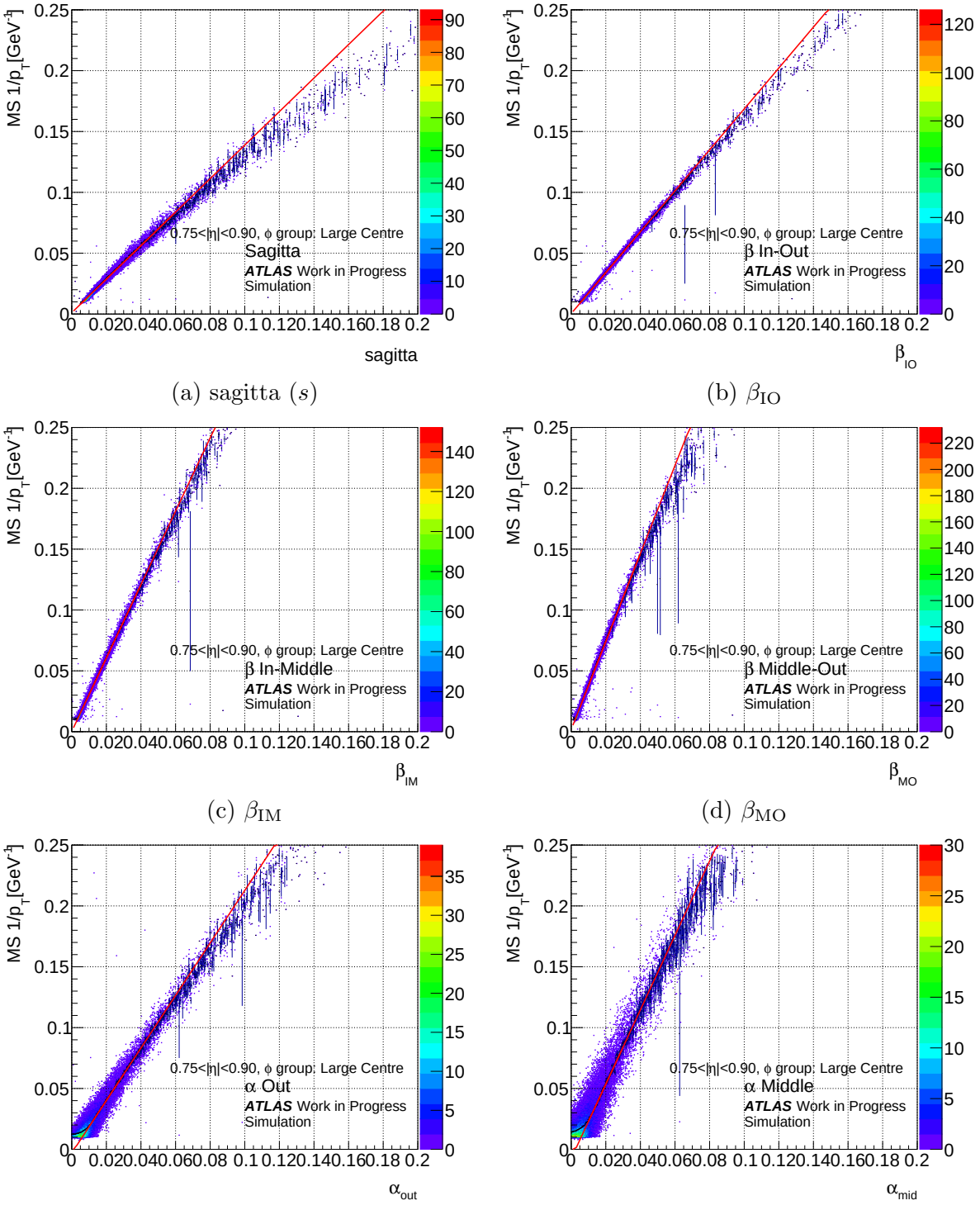

(a) sagitta (s) (b) β_{IO}

(c) β_{IM} (d) β_{MO}

(e) α_{out} (f) α_{mid}

Fig. 3.9 Parametrisation of p_{T} in the region of $0.75 < |\eta| < 0.90$ and ϕ group of Large Centre at A-side with positive-signed parameters. The red line showns the results of linear fitting and are extrapolated to the low-p_{T} and high-p_{T} regions. The width of the distribution indicates the p_{T} resolution of each parameter. If we focus on the two αs, we will find that the linearity will be lost in the very high-p_{T} region, which means parameter α is not suitable to be used for determining p_{T} in the high-p_{T} region. Conversely, parameter β can be used in most of the p_{T} region for the widths of distribution do not change.

are reconstructed with the offline algorithms, and only reconstructed segments associated with an offline combined muon are used to calculate the parameters. Here, two kinds of p_{T} can be parametrised. One is the offline combined p_{T} given by combining the ID, Calo and Muon Spectrometer information. The other is the offline muon spectrometer p_{T} with the information from Muon Spectrometer only. The most significant difference between the offline combined p_{T} and the offline muon spectrometer p_{T} is that the offline combined p_{T} has a correction of the energy loss in the Calorimeter for the muon tracks. Since the energy loss in the Calorimeter is a random process, the uncertainty from the Lorentzian distribution affects the p_{T} resolution and can not be eliminated only by using the MS information. Thus we decide to perform a parametrisation of the muon spectrometer p_{T}.

In the parametrisation, we perform linear fittings on the parameter-$1/p_{\mathrm{T}}$ distributions for all regions considering the sign of parameters. The fittings are not performed in all areas, for the linearity is not good in the very low or high p_{T} region. The fitting areas are set to 10 GeV $< p_{\mathrm{T}} <$ 20 GeV in most of the regions with minor tunings in some regions that have a small number of entries. The parametrisation of the muon spectrometer p_{T} is shown in Fig. 3.9. Excellent linearities can be confirmed for all the parameters in the fitting regions. The gradients and intercepts of the fitting results are saved in a LUT for online use.

The muon spectrometer p_{T}s are estimated from the calculated parameters using the LUT. The estimated muon spectrometer p_{T} is sent to the EF for later software-based calculations, as the MuonSA algorithm in the current trigger system. The p_{T} of muons at the IP can be approximately estimated by a simple correction considering average energy loss. The difference between the offline muon spectrometer p_{T} and the offline combined p_{T} is shown in Fig. 3.10. As the lowest order approximation, the offline combined p_{T} is calculated by adding an offset that is the average energy loss in the Calorimeter to the muon spectrometer p_{T}, as Eq. (3.7).

$$p_{\mathrm{T}}^{\mathrm{IP}} = p_{\mathrm{T}}^{\mathrm{MS}} + 2.77 \text{ [GeV]} \tag{3.7}$$

In the following chapters, the p_{T} calculated by the MuComb algorithms will be noted as offline combined p_{T} while the p_{T} at the IP estimated by the AM-MDT muon trigger will be noted as $p_{\mathrm{T}}^{\mathrm{IP}}$. The offline muon spectrometer p_{T} will be noted as offline MS p_{T}, and the muon spectrometer p_{T} estimated by the AM-MDT muon trigger, will be $p_{\mathrm{T}}^{\mathrm{MS}}$.

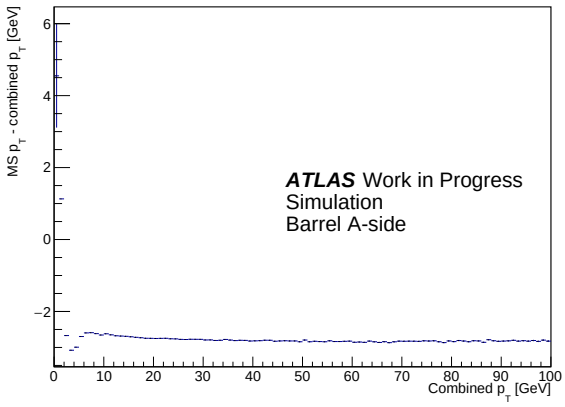

Fig. 3.10 The difference between offline combined p_{T} and offline muon spectrometer p_{T}. The difference is almost constant in most of the p_{T} region except the very low-p_{T} region.

3.3.5 Threshold Determination

The decision of the AM-MDT muon trigger is made by comparing the parameter with corresponding thresholds. The procedure to determine a parameter threshold in one region is as follows. First, the parameter distribution is divided into two parts with the sign of the parameter. Then a p_{T} window is decided. The window for the case of p_{T} threshold 20 GeV is 16 GeV $< p_{\mathrm{T}} <$ 24 GeV. Then the distributions of parameters of the RoIs in the window area are created, as shown in Fig. 3.11. An integration is performed from zero to a positive cut value for the distribution with a plus sign. For the distribution with a minus sign, the integration is performed from negative cut value to zero. The ratio of the integral and the total entries in the corresponding distribution is calculated. The values of thresholds are determined as the point that the ratio becomes 95%. Finally, a positive threshold and a negative threshold are determined. This procedure is performed for all 6 parameters, in all 42 regions.

The thresholds of $p_{\mathrm{T}}^{\mathrm{MS}}$ corresponding to the parameters are then converted from the parameter thresholds using the parametrisation described in the previous section. The thresholds of $p_{\mathrm{T}}^{\mathrm{IP}}$ are defined as $p_{\mathrm{T}}^{\mathrm{MS}}$ thresholds +2.77 GeV.

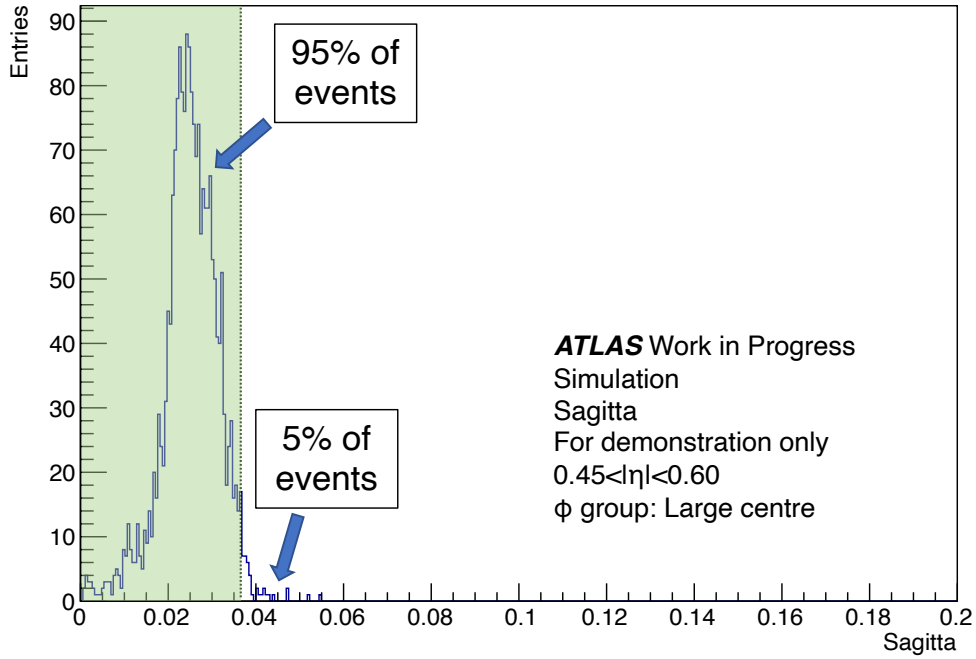

Fig. 3.11 A demonstration image of the determination of the parameter thresholds. The sagitta distribution in the region of $0.45 < |\eta| < 0.60$ and ϕ group Large Centre at the A-side is shown. The dashed line shows the determined cut value that will be stored as the parameter threshold. At this time, 95% of events are in the green area. The graph is for demonstration only.

3.4 Hardware Overview

The AM-MDT Muon Trigger is considered to be implemented on a Pattern Recognition Mezzanine (PRM) with control from a host board of the MDT muon trigger. The basic design of the PRM and the functionality test have already done [47]. As shown in Fig. 3.12, on the PRM board, 24 AMchips (4 groups ×6 AMchips) will be installed, and one Xilinx Ultrascale+ FPGA

with interface to the AMchips is between the AMchips and the I/O interface to the host board. The High Bandwidth Memories (HBM) on the board are used to store the pattern information. When the patterns are matched in the AMchips, the pattern IDs are sent to the HBM via the FPGA. The information associated with the matched pattern are read out as well.

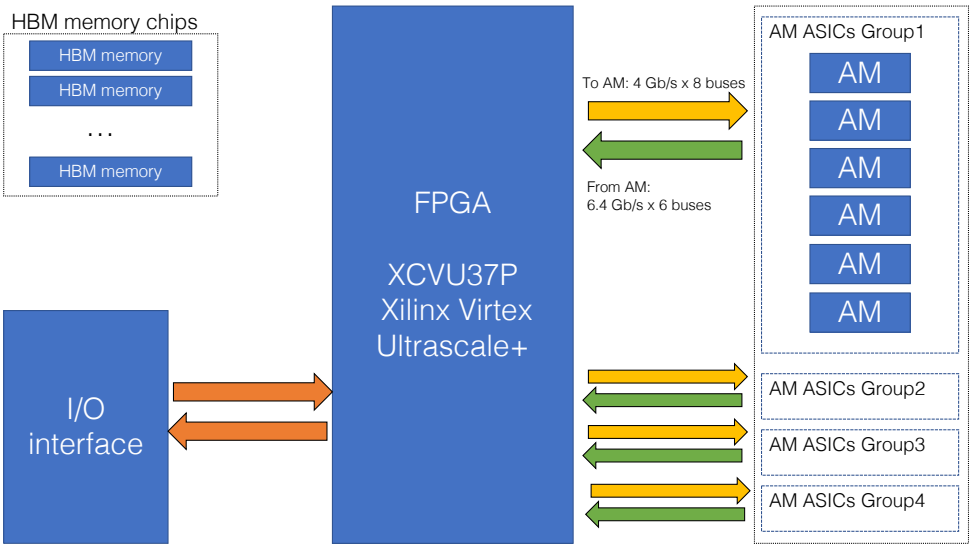

Fig. 3.12 The concept design of the board of the AM-MDT Muon Trigger. [48]

According to the documents of the specification of Associative Memory ASIC, the maximum number of usable patterns of one group of AMchips is limited to 400k per ASIC [46]. From the research of bank generation, two groups of AM ASICs are assigned to the Barrel Inner Station and the Barrel Middle Station, and four groups for the Barrel Outer Station. The corresponding pattern number limits are 800k and 1600k. Fig. 3.13 shows the arrangement of AMchips and the scheme of communication between the FPGA and AMchips in different limits on pattern number. The units for the pattern matching are called pattern matching engine that contains two or four AMchips. Since three matching requirements (six-out-of-six hits, five-out-of-six hits, and four-out-of-six hits) exist in the AM-MDT muon trigger, three pattern matching engines are used. Each engine has its own pattern bank, but the pattern list in the banks are the same. The only difference between the engines is the configuration of matching requirement in the AMchips. The readout of the engines are prioritised in the order of six-out-of-six, five-out-of-six and four-out-of-six to suppress the multiplicity of matched patterns.

When a candidate of muon arrives from the TGC or RPC trigger to the MDT processor, the hits information of the MDT tubes near the RoI are extracted and sent to the AMchips. Then the AMchips perform the pattern matching. The output patterns are sent to the FPGA on the PRM as the input of the segment reconstruction. The segment reconstruction is performed on the FPGA on the PRM with the matched patterns and associated information is read out from the HBM. The FPGA on the PRM then sends the reconstructed segments to another FPGA on the host board. The FPGA on the host board collects segments from each station and calculates the parameters with the online algorithm implemented. A final trigger decision of the AM-MDT muon trigger is given by the online algorithm. The communication between the AM-MDT Muon Trigger and the sector logic is also performed via the control board.

The estimated latency of segment reconstruction on the PRM is 477 ns [48] assuming 250 MHz clock speed at FPGA and AMchips. The remaining time for the AM-MDT Muon Trigger is around 1.7 μs. Since the parameters are calculated with simple formulas and the results of trigger decision can be made with the help of the parameter thresholds LUT, the time is sufficient for

the parameter calculation and the trigger decision to be done. The AM-MDT Muon Trigger correctly meets the hardware requirements well.

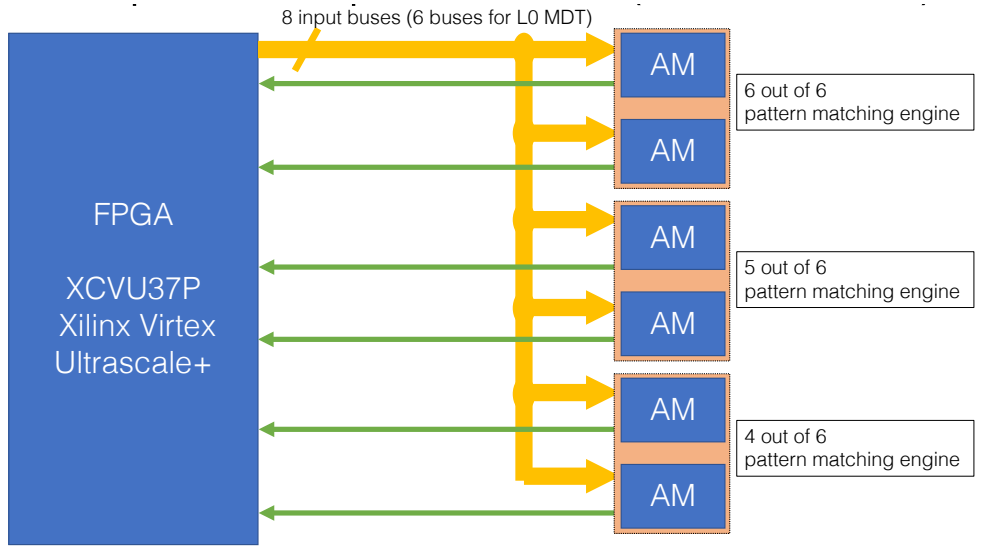

(a) 800k

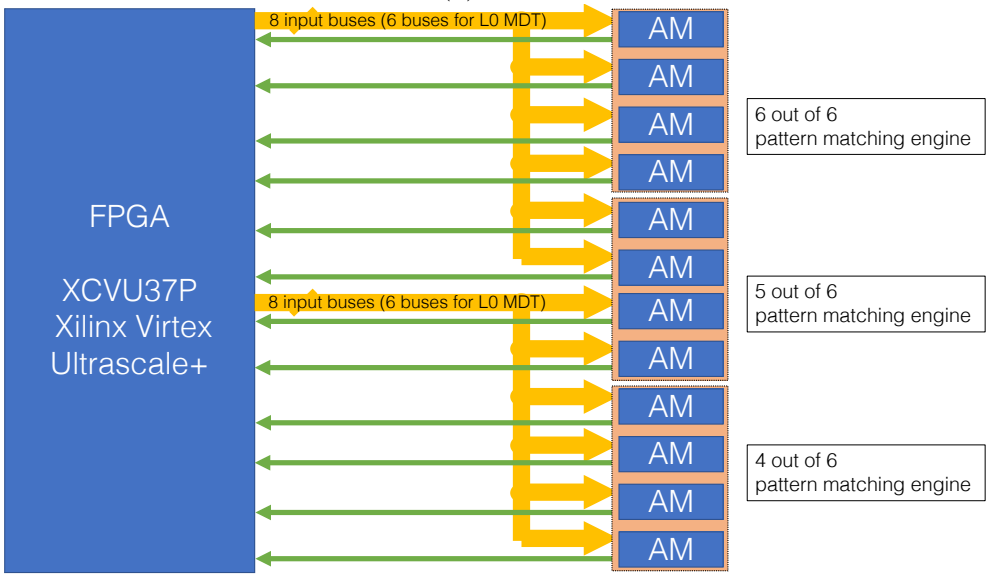

(b) 1600k

Fig. 3.13 Assignments of AMchips with pattern number limit 800k (a) and 1600k (b). In both arrangements, the AMchips are organised into three pattern matching engines with same pattern banks. Each pattern matching engine runs pattern matching with different requirements on numbers of hits matched. [48]

Chapter 4

Muon Selection Efficiency Study with Monte Carlo Samples

The AM MDT muon trigger described in Chapter 3 was implemented in a software emulation. After the implementation of the full chain software emulation, we tested the muon selection efficiency with the AM-MDT muon trigger in Monte Carlo samples. In this chapter, the results with a single muon sample and a $Z \to \mu\mu$ sample will be shown.

4.1 Test Conditions

The test area is limited to the barrel A-side ($0 < |\eta| < 1.05$), and the emulation of the pattern-finding step uses the banks described in Chapter 3. Simulation of the RPC trigger is not included in the software[*1], thus the RoIs are generated using information of offline combined muons. Thus the accuracy of RoIs is better than actual. The samples used for the tests are as follows.

- **Single muon test sample**: Single muon particle gun, background free, flat in η, ϕ, and p_{T} from 3 GeV to 100 GeV.
- $Z \to \mu\mu$ **test sample**: $Z \to \mu\mu$ process with 200 pileups and 25 cavern backgrounds.

In the test, the offline combined p_{T} of the muons are considered as the actual p_{T} of muons. The muons are selected using $p_{\mathrm{T}}^{\mathrm{IP}}$ thresholds transformed from the parameter thresholds that are corresponding to an offline p_{T} threshold of 20 GeV. The parameter thresholds are tuned to make the acquisition efficiency at the point of 20 GeV in offline p_{T} to be 95%. The acquisition efficiency is defined as the ratio of offline combined muon that passed the AM-MDT muon trigger with respect to all offline combined muons. Therefore, the ideal result is that 100% efficiency is achieved in the region of offline p_{T} larger than the threshold and all the muons with offline p_{T} smaller than the thresholds are discarded. However, since the p_{T} resolution of the AM-MDT muon trigger is finite, as well as the efficiencies of segment reconstruction is not 100%, the results will not be a step function at the threshold, but a turn-on curve will be seen, as an example shown in Fig. 4.1.

The performance tests of muon selection first check the resolution of p_{T} at IP calculated by the AM-MDT muon trigger parameters. Then the turn-on curves against offline combined p_{T} with α only, β only and s are drawn to understand the individual performances of parameters. The resolution of $p_{\mathrm{T}}^{\mathrm{IP}}$ is calculated from the distribution of residual between the offline combined p_{T} and the $p_{\mathrm{T}}^{\mathrm{IP}}$ with a gaussian fitting. Then, a combined result with the prioritisation of parameter shows the expected performance of the AM-MDT muon trigger. The turn-on curves for individual performances are drawn with muons that have corresponding valid parameters. For example, a muon matched with two segments in the Inner station and the Outer station

[*1] One of the reasons is that the simulation of the upgraded RPC trigger is not established yet.

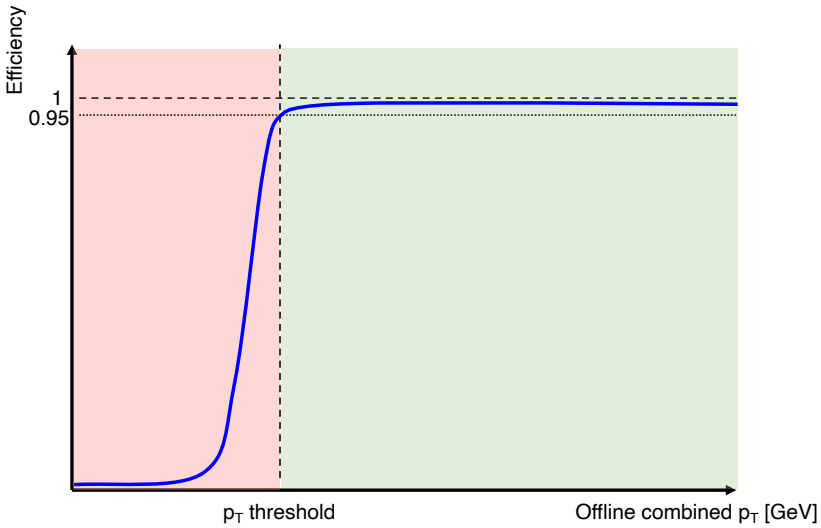

Fig. 4.1 An example of the turn-on curve with the efficiency tuned to be 95% at the p_{T} threshold. The higher efficiency in the green region and the lower efficiency in the red region are corresponding to a better performance of muon selection.

would not be used to test the performance of α_{mid}, β_{IM}, β_{MO} and sagitta. In contrast, the turn-on curve in the combined result is drawn with all offline combined muons as the denominator of the efficiency. Offline combined muons that have no valid parameters are all discarded and decrease the efficiency plateau of the combined result.

The test results using the single muon test sample show the performance of AM-MDT muon trigger in an ideal very low pileup environment and indicate the performance limit of the developed online algorithm. On the other hand, the results using the $Z \to \mu\mu$ test sample show the performance of AM-MDT muon trigger under the toughest environment that can be expected at HL-LHC.

4.2 Estimates with Single Muon Sample

4.2.1 Results with Parameter α only

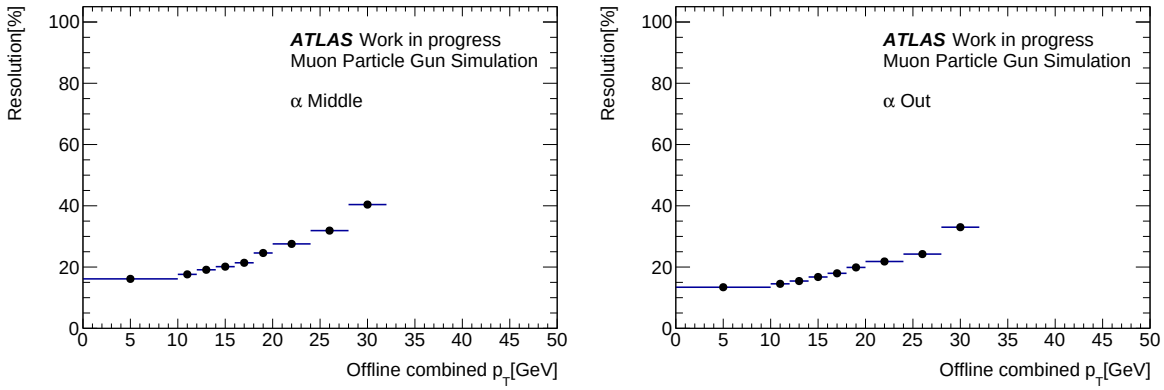

Fig. 4.2 $p_{\mathrm{T}}^{\mathrm{IP}}$ resolutions of α_{mid} (left) and α_{out} (right) using the single muon test sample.

The results of $p_{\mathrm{T}}^{\mathrm{IP}}$ resolutions with parameter α in the single muon test sample are shown in

Fig. 4.2. The binning is tuned to match the binning of the resolution test using real data (details in Chapter 5). The $p_{\mathrm{T}}^{\mathrm{IP}}$ resolution with parameter α is about 15% for low-p_{T} muons and reaches more than 30% at about 30 GeV. In all p_{T} regions, α_{out} has a better resolution than α_{mid} for about 5%. These results support the prioritisation of using α_{out} when both α's are available. The p_{T} dependence of the resolution indicates that parameter α can be used for muon selections in the low-p_{T} region but not suitable to estimate p_{T} of high-p_{T} muons.

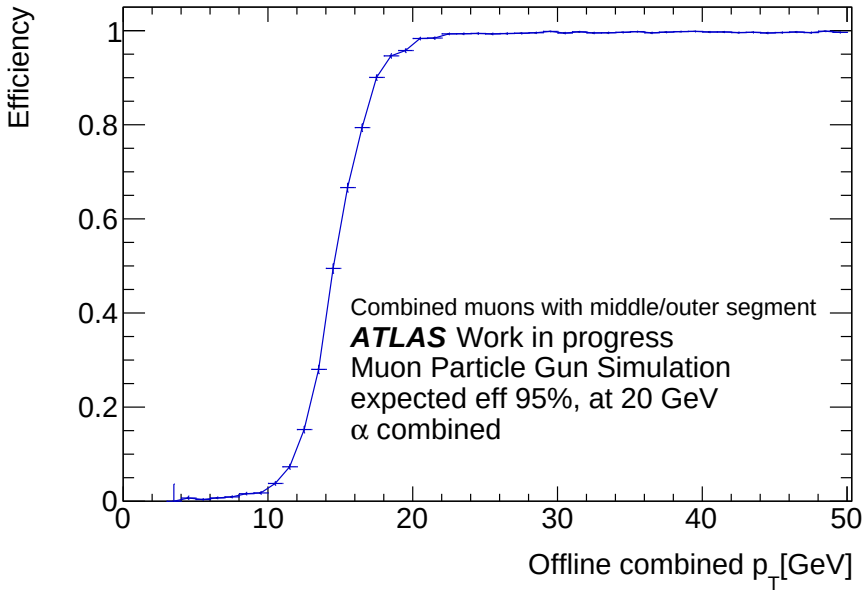

Fig. 4.3 Turn-on curve with only parameter α with α_{out} prioritised using the single muon test sample.

Fig. 4.3 shows the efficiency of the AM-MDT muon trigger when using only parameter α in the single muon test sample. The denominator contains all offline combined muons in which at least a valid α_{mid} or α_{out} is calculated. For the muons with both α's available, α_{out} is prioritised to be used. From the turn-on curve, an excellent acquisition efficiency is achieved in the region offline combined $p_{\mathrm{T}} > 20$ GeV, and muons with lower p_{T} are effectively discarded, especially in the region offline combined $p_{\mathrm{T}} < 10$ GeV.

4.2.2 Results with Parameter β only

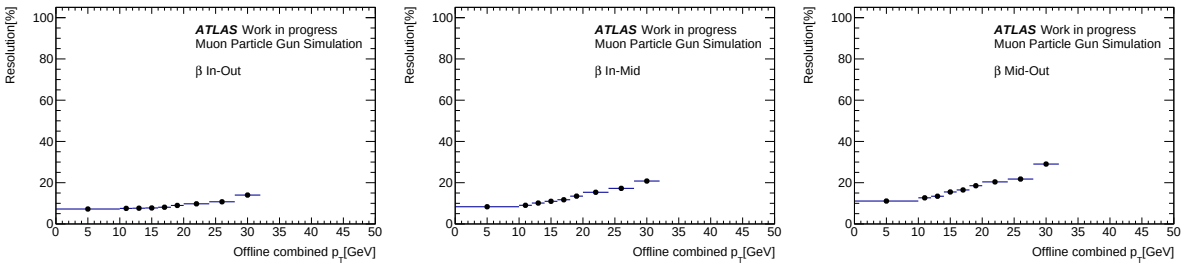

Fig. 4.4 $p_{\mathrm{T}}^{\mathrm{IP}}$ resolutions with β_{IO} (left), β_{IM} (middle) and β_{MO} (right) using the single muon test sample.

The $p_{\mathrm{T}}^{\mathrm{IP}}$ resolutions with β in the single muon test sample are shown in Fig. 4.4. The results show different behaviours with combinations of segments in different stations. β_{IO} shows very

good $p_{\mathrm{T}}^{\mathrm{IP}}$ resolution of 7% in the low-p_{T} region and still maintains a 15% at 30 GeV. The $p_{\mathrm{T}}^{\mathrm{IP}}$ resolutions with β_{IM} and β_{MO} are both about 10% in the low-p_{T} region. At the point of $p_{\mathrm{T}}^{\mathrm{IP}}$ of 30 GeV, the resolutions rise to 20% for β_{IM} and 30% for β_{MO}, respectively. This difference on $p_{\mathrm{T}}^{\mathrm{IP}}$ resolutions comes from the difference of distance between MDT stations. The combinations of segments in the Inner station and the Outer station have the longest distance between stations, thus the largest angular variation of the muon track direction. When the curvature radius is fixed, the larger the difference in direction measured, the more precise the muon p_{T} can be estimated. As a result, according to the resolution results, we prioritised the three β's in the order of β_{IO}, β_{IM} and β_{MO} when more than one β is calculated for a muon track.

With the parameter prioritised algorithm, the result of performance test using parameter β in the single muon test sample is shown in Fig. 4.5. Almost 100% acquisition efficiency is achieved in the region of offline combined $p_{\mathrm{T}} > 20$ GeV. The turn-on curve in Fig. 4.5 is sharper compared to the turn-on curve using α shown in Fig. 4.3, that is consistent with the results of $p_{\mathrm{T}}^{\mathrm{IP}}$ resolution.

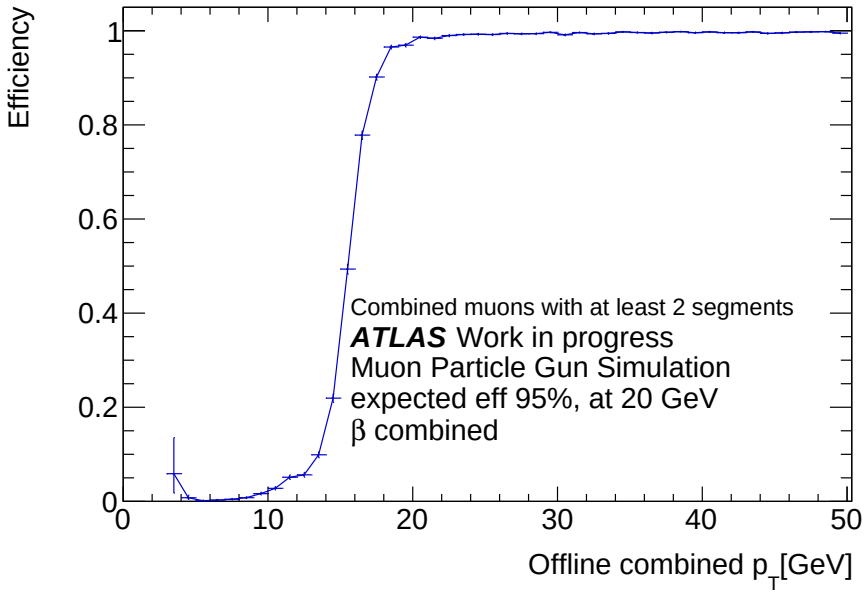

Fig. 4.5 Turn-on curve with only parameter β, with parameters prioritised in the order of β_{IO}, β_{IM} and β_{MO} using the single muon test sample.

4.2.3 Results with Parameter sagitta (s) only

The $p_{\mathrm{T}}^{\mathrm{IP}}$ resolution with sagitta (s) in the single muon test sample is shown in Fig. 4.6. Different from other parameters, the $p_{\mathrm{T}}^{\mathrm{IP}}$ resolution seems to be stable in the region of offline combined $p_{\mathrm{T}} < 30$ GeV at a level of less than 10%. This difference on the $p_{\mathrm{T}}^{\mathrm{IP}}$ dependence originates from the definition of the parameters. The parameter α and β use the angular information of muon segments and the parameter s uses the information of segment positions. The typical order of α and β is 10 mard and the angular resolutions of reconstructed segments are about $1 \sim 2$ mrad. When the p_{T} increases, the parameter α and parameter β become smaller, and the effect of the angular resolutions of reconstructed segments becomes larger and results in the worse p_{T} resolution. However, the typical value of parameter s is 1 cm, and the spatial resolution of the reconstructed segments is $200 \sim 370$ μm. Thus the uncertainty of segment positions do not contribute much to the uncertainty of $p_{\mathrm{T}}^{\mathrm{IP}}$ resolution in the p_{T} region shown in Fig. 4.6.

Due to the high $p_{\mathrm{T}}^{\mathrm{IP}}$ resolution, the performance with parameter s only has a stable perfor-

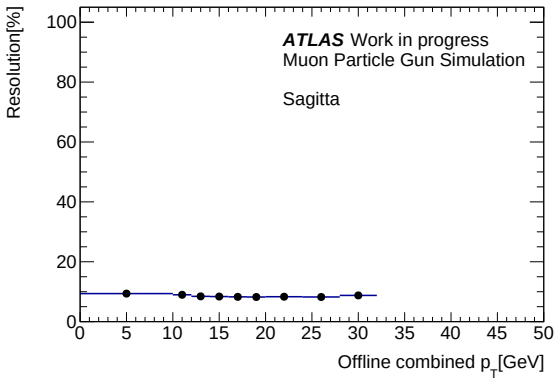

Fig. 4.6 $p_{\mathrm{T}}^{\mathrm{IP}}$ resolution with sagitta (s) using the single muon test sample.

mance in the region of offline combined $p_{\mathrm{T}} > 20$ GeV with almost 100% acquisition efficiency and a very steep turn-on curve, as shown in Fig. 4.7. From the turn-on curve, we can find that muons with offline combined $p_{\mathrm{T}} < 10$ GeV that have a valid s are completely discarded. Based on this fact, the parameter s is expected to make a significant contribution to rate reduction in the low-p_{T} region.

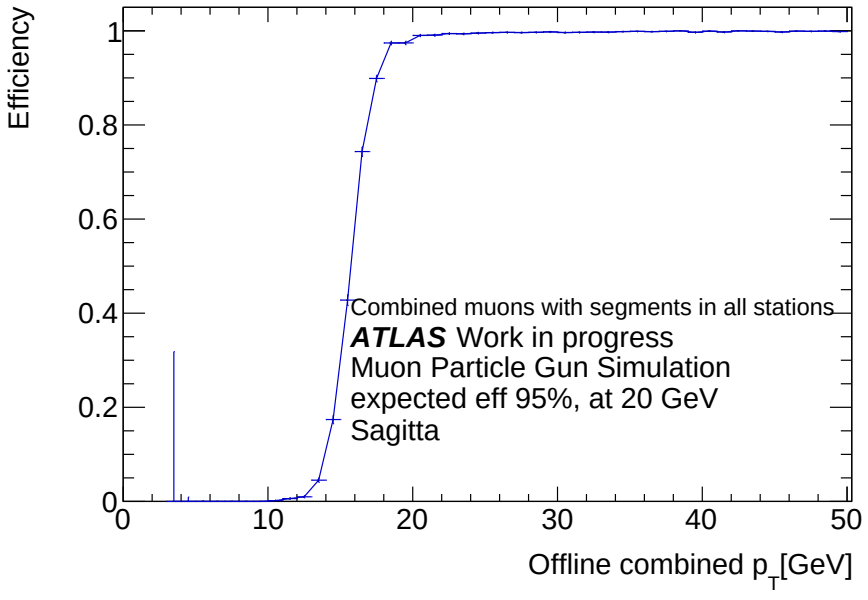

Fig. 4.7 Turn-on curve with parameter sagitta (s) using the single muon test sample.

4.2.4 Combined Result with Single Muon Sample

Considering the $p_{\mathrm{T}}^{\mathrm{IP}}$ resolutions, we decided to prioritise the parameters in the order of sagitta (s), β_{IO}, β_{IM}, β_{MO}, α_{mid}, and α_{out}, as described in Chapter 3. The combined result of muon selection with the single muon sample is shown in Fig. 4.8. The shape of the turn-on curve is similar to the turn-on curves of the individual results, but the acquisition efficiency in the region of offline combined $p_{\mathrm{T}} > 20$ GeV is 97.7%. The cause of the inefficiency is the offline combined muons that failed to calculate any valid parameter for muon selection. As shown in Fig. 4.9, about 2% of offline combined muons have matched AM-reconstructed segments in the Inner

station only or matched no AM-reconstructed segment. This result shows the ideal performance with the algorithm described in this thesis using the current version bank and the inefficiency is expected to be recovered by optimising the pattern generation and the matching conditions between RoIs and segments.

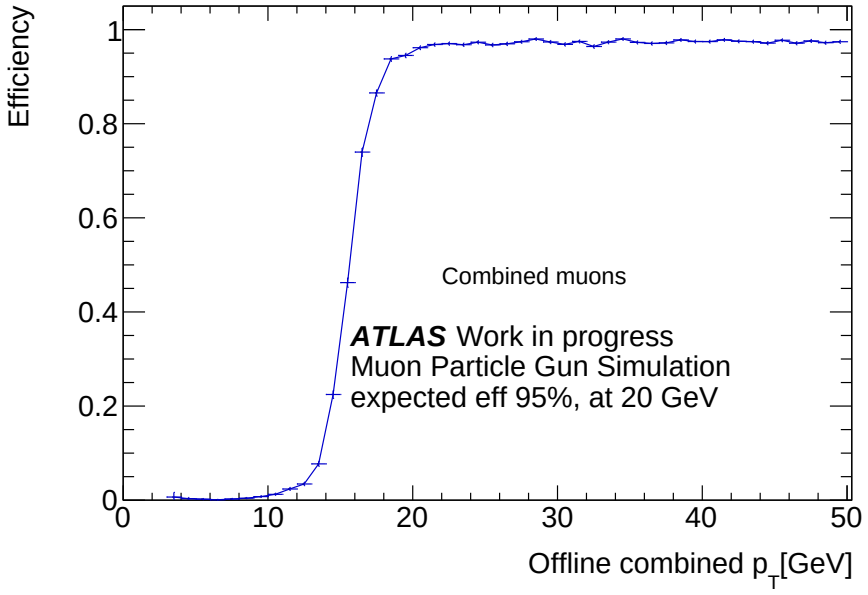

Fig. 4.8 Combined performance using the online algorithm with prioritised parameters using single muon test sample.

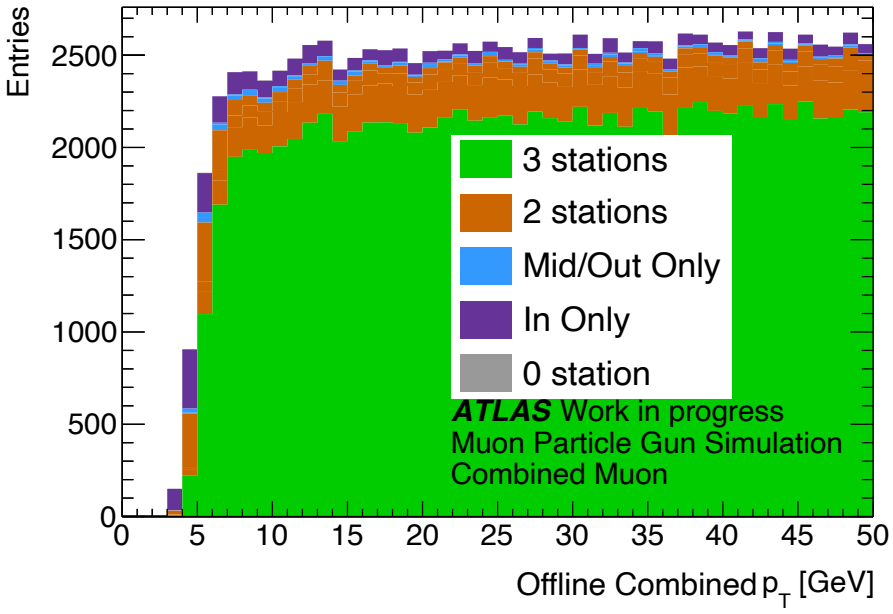

Fig. 4.9 Components of offline combined muons contained in the single muon test sample. The colour shows the number of AM reconstructed segments matched with the offline combined muons. The offline combined muons with segments in the Inner station only (purple) and with no segmet matched (grey) can not calculate any valid parameter and are discarded by the AM-MDT muon trigger in the performance test.

4.3 Estimates with the $Z \to \mu\mu$ Sample under the HL-LHC environment

4.3.1 Results with Parameter α only

Fig. 4.10 shows the $p_{\mathrm{T}}^{\mathrm{IP}}$ resolution with parameter α using the $Z \to \mu\mu$ test sample and the combined performance of the two α's with α_{out} prioritised is shown in Fig. 4.11. Compared with the results using the single muon test sample, the resolutions slightly get worse. The shape of the turn-on curve is almost the same as the turn-on curve drawn using the single muon sample, except a rise of the acquisition efficiency at the low-p_{T} region and some inefficiency in the plateau region. With the consideration of the difference of the two test samples, the rise is possibly caused by the accidentally matching with offline combined muon and segments created by pileups. The $p_{\mathrm{T}}^{\mathrm{IP}}$ given by the parameter calculated using the accidentally matched segments is almost unrelated to the p_{T} of muons. Hence some of the low-p_{T} muons accidentally pass the selection and some of the high-p_{T} muons are wrongly discarded by the algorithm.

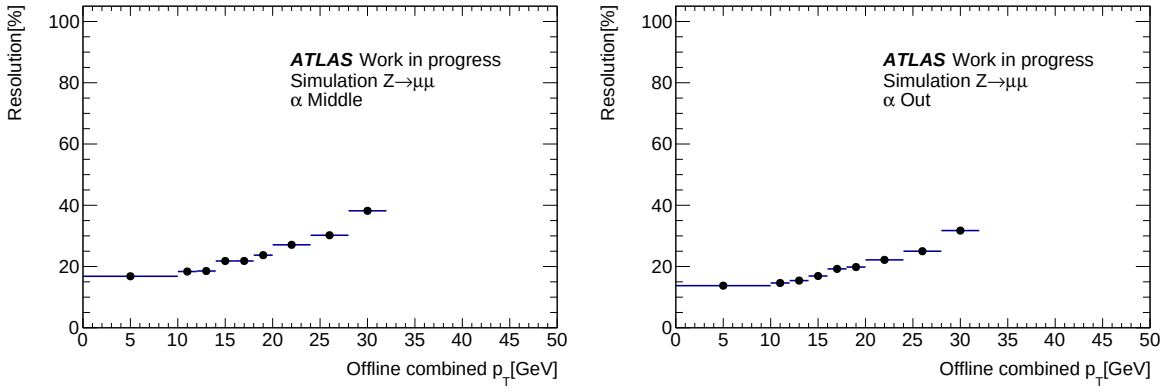

Fig. 4.10 $p_{\mathrm{T}}^{\mathrm{IP}}$ resolutions with α_{mid} (left) and α_{out} (right) using the $Z \to \mu\mu$ test sample.

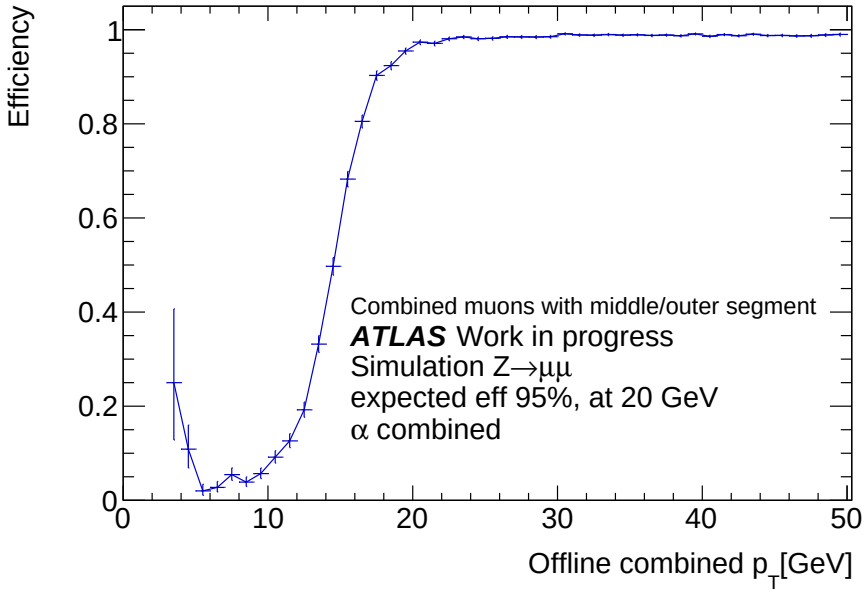

Fig. 4.11 Turn-on curve with only parameter α with α_{out} prioritised using the $Z \to \mu\mu$ test sample.

4.3.2 Results with Parameter β only

Fig. 4.12 and Fig. 4.13 show the p_{T}^{IP} resolution and the turn-on curve calculated with the parameter prioritised algorithm of parameter β using the $Z \to \mu\mu$ test sample, respectively. Similar to the case of parameter α, no significant change is confirmed in the performance tests of parameter β. The p_{T}^{IP} resolution and the shape of the turn-on curve is almost the same as the results with the single muon test sample. The rise of acquisition efficiency is also observed for the muons with offline combined $p_{\text{T}} < 15$ GeV. The origin of this rise is also the segments created by the particles from pileups accidentally matched with the offline combined muons. The accidentally matched segments sometimes give a parameter β that corresponds to large p_{T}^{IP} and results in a wrong trigger decision. Since multiple MDT stations involve the calculation of parameter β, the existence of segments from pileups means a much larger number of possible combinations of segments. Therefore, the wrong combinations of segments used for β calculation increase as the luminosity increases. However, since the actual change of the turn-on curve is not significant, the conditions required in the parameter calculation step is effective for selecting the correct combination of segments.

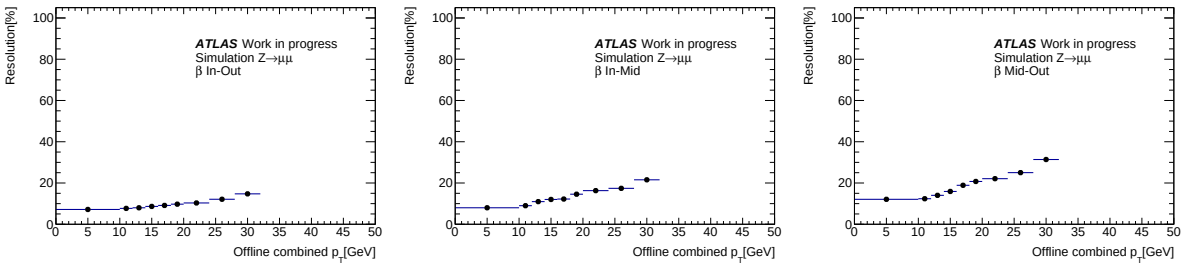

Fig. 4.12 p_{T}^{IP} resolutions with β_{IO} (left), β_{IM} (middle) and β_{MO} (right) using the $Z \to \mu\mu$ test sample.

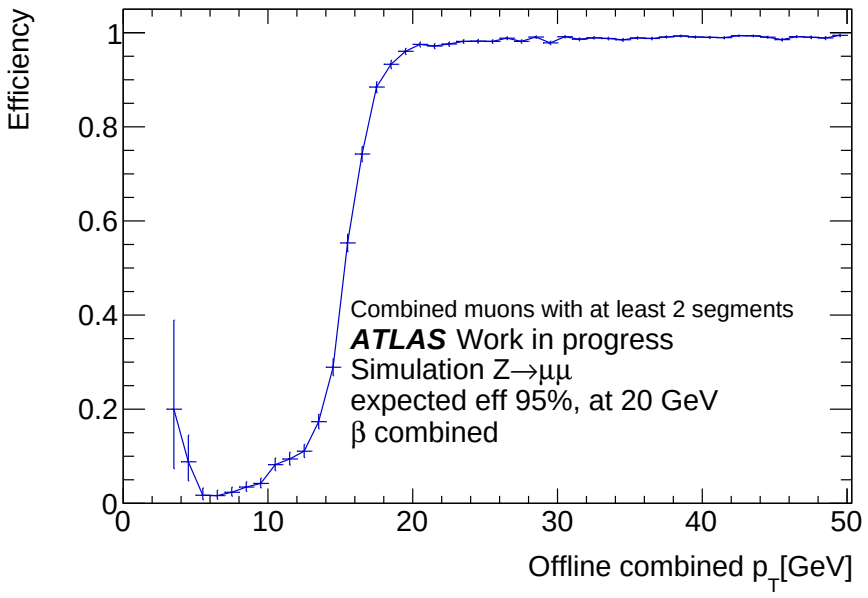

Fig. 4.13 Turn-on curve with only parameter β, with parameters prioritised in the order of β_{IO}, β_{IM} and β_{MO} using the $Z \to \mu\mu$ test sample.

4.3.3 Results with Parameter sagitta (s) only

The result of $p_{\mathrm{T}}^{\mathrm{IP}}$ resolution with parameter sagitta (s) with the $Z \to \mu\mu$ test sample is shown in Fig. 4.14. The parameter s maintains an excellent $p_{\mathrm{T}}^{\mathrm{IP}}$ resolution at a level of about 9% under the high pileup environment. Fig. 4.15 shows the individual performance on muon selection only using parameter s with the $Z \to \mu\mu$ test sample. Almost the same shape of turn-on curve is observed, and no rise in the low-p_{T} region is confirmed. This result reconfirms the effectiveness of the conditions required for the selection of segment combinations.

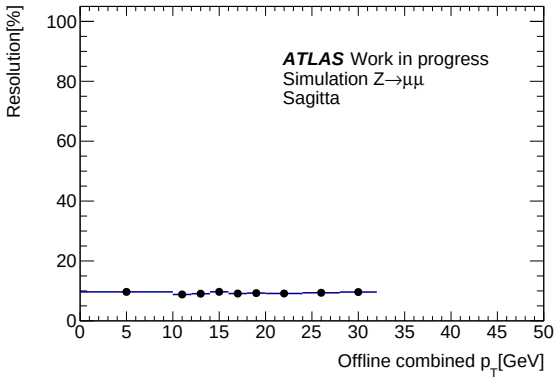

Fig. 4.14 $p_{\mathrm{T}}^{\mathrm{IP}}$ resolution with sagitta (s) using the $Z \to \mu\mu$ test sample.

4.3.4 Combined Result under the HL-LHC environment

The combined result of performance on muon selection using the $Z \to \mu\mu$ test sample is shown in Fig. 4.16. The acquisition efficiency in the region of offline combined $p_{\mathrm{T}} > 20$ GeV is 95.9%,

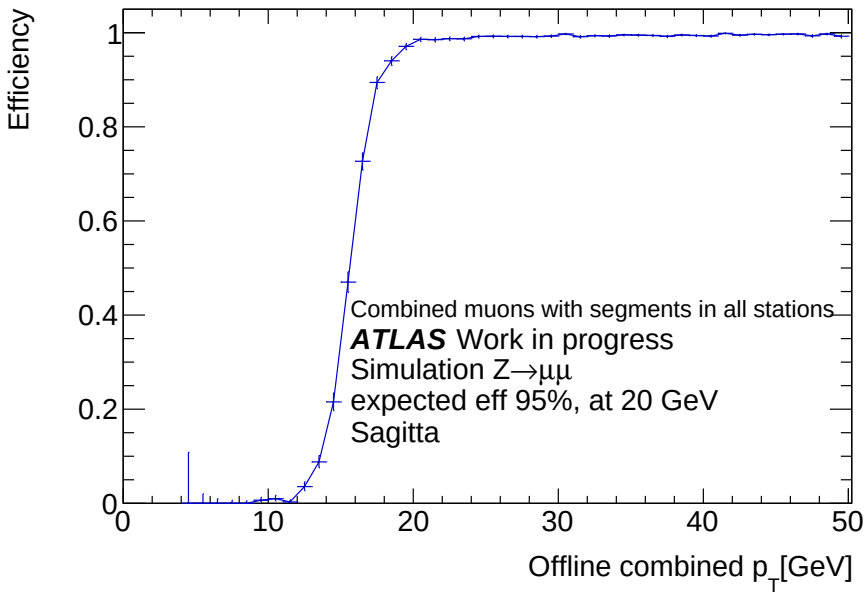

Fig. 4.15 Turn-on curve with only parameter sagitta (s) using $Z \to \mu\mu$ test sample.

and low-p_{T} muons are efficiently discarded except for a small rise of efficiency in the region of offline combined $p_{\mathrm{T}} < 5$ GeV. By checking the components of offline combined muons contained in the $Z \to \mu\mu$ test sample, as shown in Fig. 4.17, about 2% of muons have only one segment in the Inner station or no matched segment. The remaining inefficiency is the intrinsic inefficiency caused by the correction of energy loss in the Calorimeter. The details about the intrinsic inefficiency is described in Appendix B. The small rise of efficiency in the low-p_{T} region comes from the components accidentally passing the selection using parameter α or parameter β. As the number of muons accidentally passing the selection is very small, they do not impact the total performance. As a consequence of the tests using $Z \to \mu\mu$ test sample, the AM-MDT muon trigger works well and has good robustness to the particles produced by the pileups even under the HL-LHC environment. High acquisition efficiency is achieved for the muons with $p_{\mathrm{T}}^{\mathrm{IP}}$ larger than the p_{T} threshold.

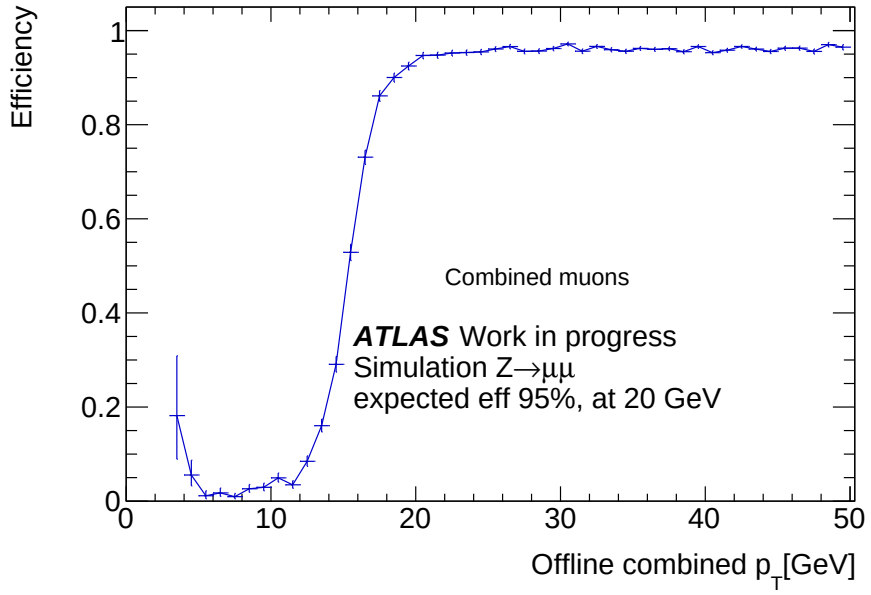

Fig. 4.16 Combined performance using the online algorithm with prioritised parameters using the $Z \to \mu\mu$ test sample.

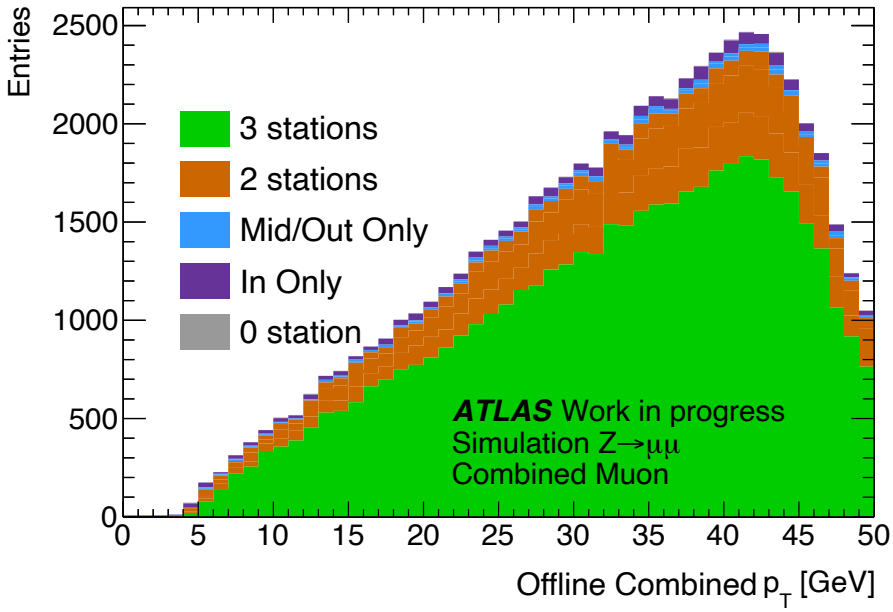

Fig. 4.17 Components of offline combined muons contained in the $Z \to \mu\mu$ test sample. The colour shows the number of AM reconstructed segments matched with the offline combined muons.

Chapter 5

Performance Test with ATLAS Run 2 Dataset

The results of tests using Monte Carlo samples show that the AM-MDT muon trigger has good $p_{\mathrm{T}}^{\mathrm{IP}}$ resolution and strong ability on muon selection at the HL-LHC environment. However, only performance against true muons was estimated. The rejection efficiency against hadrons faking muons was not estimated. In addition, even for true muons, the factors that can influence the performance, such as the misalignment of the MDT detectors were not considered. Furthermore, the granularity of the actual RoIs issued by the RPC trigger is much more coarse than the η, ϕ information of offline combined muons that we used as the centre of RoIs. As a result, the accuracy of the matching between RoIs and reconstructed muon segments is probably overestimated. The absence of the RPC trigger simulation also makes it hard to estimate the rate reduction ability of the AM-MDT muon trigger. Hence performance test using real data is necessary.

In this Chapter, the results of performance test using real data sample will be shown.

5.1 Test Conditions

The performance test uses real data sample in 32 physics runs during the ATLAS Run 2. The test area is limited to the barrel A-side ($0 < |\eta| < 1.05$) which is the same as the tests with Monte Carlo samples. Events in the test sample are required to pass the Run 2 Level 1 single muon trigger with threshold of 20 (10) GeV, called L1_MU20 (L1_MU10). Since no HLT algorithm is applied, the components of the test sample are not biased at all against HLT algorithm, thus an estimation of rate reduction ability of the AM-MDT muon trigger can be performed.

Two p_{T} thresholds are tested using the real data sample. The same $p_{\mathrm{T}}^{\mathrm{IP}}$ thresholds of 20 GeV as the Monte Carlo sample tests are used. On the other hand, the parameter thresholds corresponding to a $p_{\mathrm{T}}^{\mathrm{IP}}$ threshold of 10 GeV are additionally trained using muons with offline combined 8 GeV $< p_{\mathrm{T}} <$ 12 GeV contained in the training sample.

The performance test starts from checking the $p_{\mathrm{T}}^{\mathrm{IP}}$ resolution and the ability of muon selection to understand the effects from the misalignment of the MDT detectors and from the RPC trigger. The acquisition efficiency is calculated using the RoIs issued by the L1 muon trigger. The RoIs are required to match with offline combined muons. All the RoIs where no valid parameter is calculated are discarded. Then the test of rate reduction ability is conducted with all the RoIs issued by the L1 RPC trigger. For convenience, the RoIs that do not match an offline combined muon will be assigned a p_{T} of -1 GeV and counted in the RoIs with $p_{\mathrm{T}}^{\mathrm{IP}}$ smaller than the p_{T} threshold.

5.2 Muon Selection Efficiency at p_{T} threshold of 20 GeV

In this section real data sample obtained by L1_MU20 trigger is used.

5.2.1 Results with Parameter α only

The results of the $p_{\mathrm{T}}^{\mathrm{IP}}$ resolution are shown in Fig. 5.1 and the individual performance of muon selection with parameter α is shown in Fig. 5.2. Compared with the results using the Monte Carlo samples, the $p_{\mathrm{T}}^{\mathrm{IP}}$ resolution gets worse in the low-p_{T} region for about 5% but does not change so much at 30 GeV. The slope of the turn-on curve becomes wild, and an inefficiency is observed in the region of offline combined $p_{\mathrm{T}} > 20$ GeV. More muons with small $p_{\mathrm{T}}^{\mathrm{IP}}$ pass the AM-MDT muon trigger, and the rise of efficiency in the low-p_{T} region is more obvious. The change in the performance is probably not caused by the pileups because the average number of pileups is much smaller than the HL-LHC environment. The misalignment of detectors is also not the cause since the misalignment mainly affects the accuracy of the segment positions but has a small impact on the angular resolution of segments directions. As a result, the change in the performance is considered to be caused by the coarse granularity of the RPC trigger or fake muon contamination.

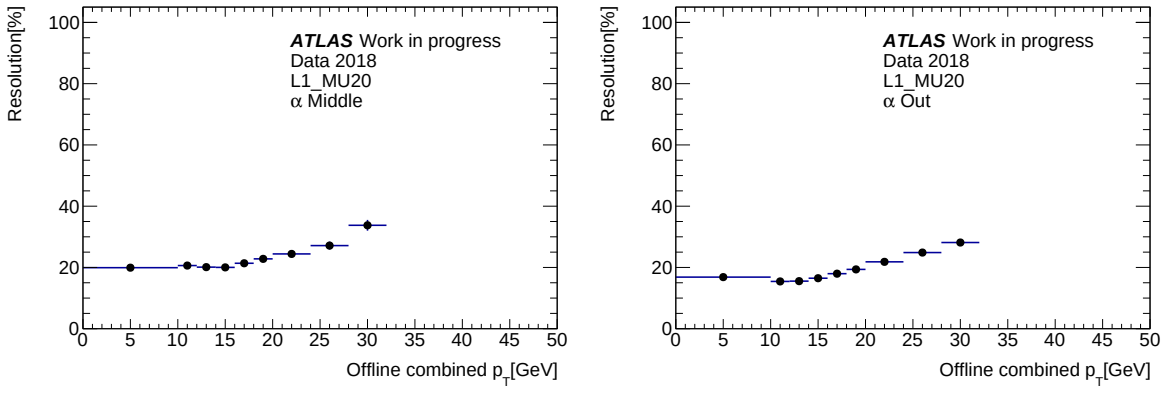

Fig. 5.1 $p_{\mathrm{T}}^{\mathrm{IP}}$ resolutions with α_{mid} (left) and α_{out} (right) in the real data sample.

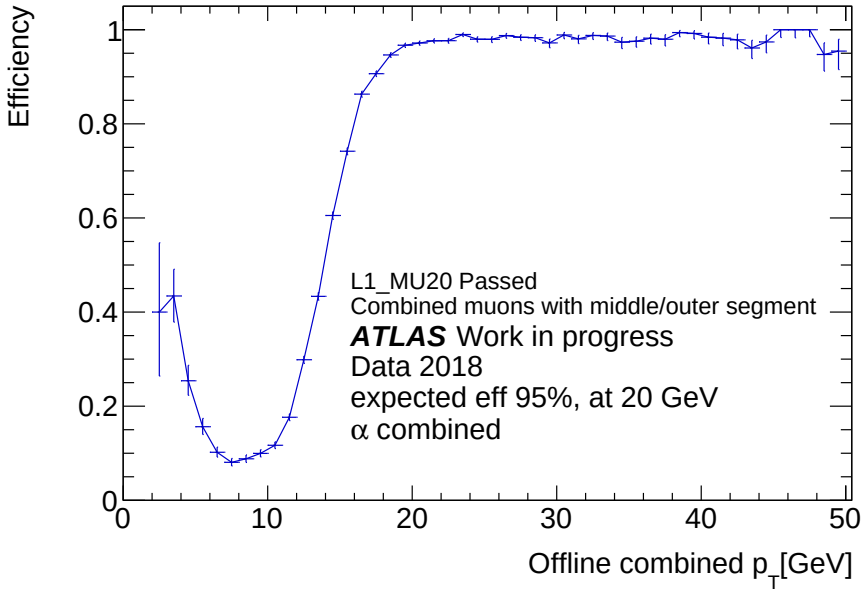

Fig. 5.2 Turn-on curve with only parameter α with α_{out} prioritised using the real data sample.

5.2.2 Results with Parameter β only

The p_{T}^{IP} with parameter β calculated in the real data sample is shown in Fig. 5.3. No change in overall trend is observed, and only changes of about 1% in each bin are confirmed. With these results, the fact that the misalignment of detectors does not impact the angular resolution of segment directions can be reconfirmed. Fig. 5.4 shows the turn-on curve calculated only using parameter β with the parameter prioritised algorithm in the real data sample. The shape of the turn-on curve does not change much, but the acquisition efficiency of muons in the low-p_{T} region increases. The cause of the rise of acquisition efficiency in the low-p_{T} region is the same as the rise observed in the results of parameter α. As the coarse granularity of the Run 2 RPC trigger causes the accidental pass of low-p_{T} muons, matching conditions between the RoIs and reconstructed segments may still have rooms to be improved.

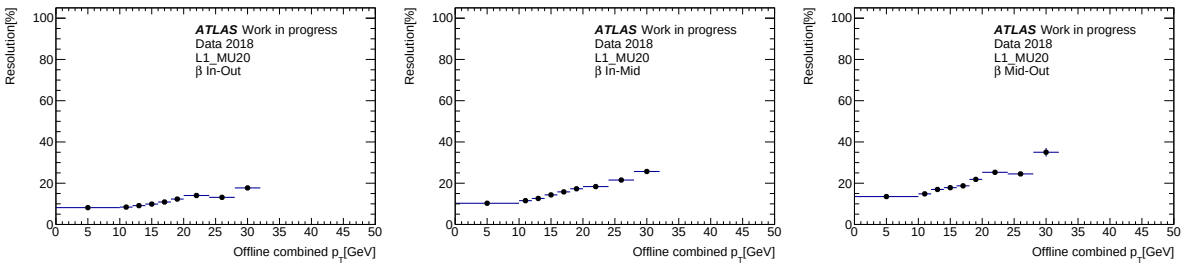

Fig. 5.3 p_{T}^{IP} resolutions with β_{IO} (left), β_{IM} (middle) and β_{MO} (right) using the real data sample.

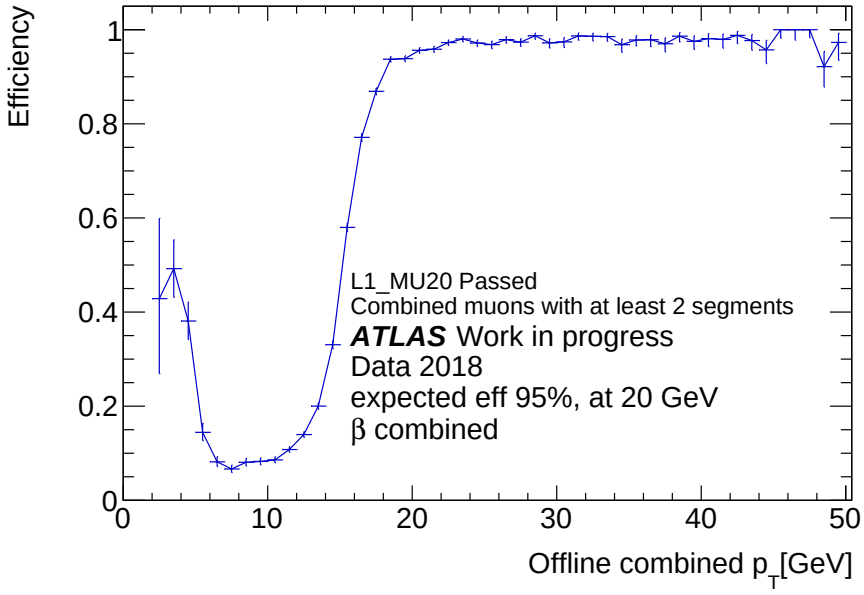

Fig. 5.4 Turn-on curve with only parameter β, with parameters prioritised in the order of β_{IO}, β_{IM} and β_{MO} using the real data sample.

5.2.3 Results with Parameter sagitta (s) only

Fig. 5.6 shows the $p_{\mathrm{T}}^{\mathrm{IP}}$ resolution with parameter sagitta (s) in the real data sample. Different from the results with Monte Carlo samples, the resolution gets worse for larger $p_{\mathrm{T}}^{\mathrm{IP}}$. In the low-$p_{\mathrm{T}}$ region, s maintains a resolution of about 10%, but the resolution drops to 20% at offline combined p_{T} of 30 GeV. The turn-on curve drawn with s only is shown in Fig. 5.6. The curve is steep but inefficiency in the region of offline combined $p_{\mathrm{T}} > 20$ GeV is seen. In the low-p_{T} region, a rise of the acquisition efficiency can be observed.

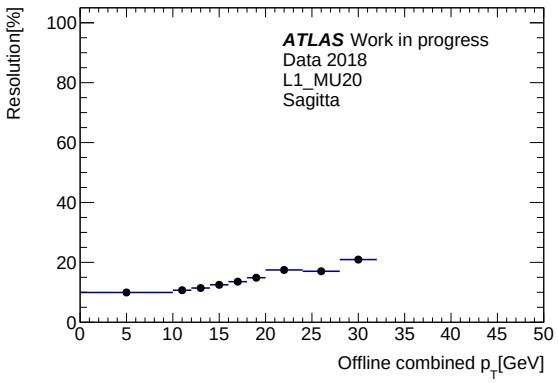

Fig. 5.5 $p_{\mathrm{T}}^{\mathrm{IP}}$ resolutions of sagitta (s) using the real data sample.

Since we have already confirmed that the conditions for the section of segment combinations of s have excellent accuracy even under the toughest HL-LHC environment, these differences are probably considered as the effect of the misalignment of the detectors. The typical order of the misalignment is about 3 mm on average and random in z-directions for each MDT unit. The effect is possible to be cancelled by a correction on the positions of reconstructed segments with the feedback from the measurements of the misalignment of MDT detectors.

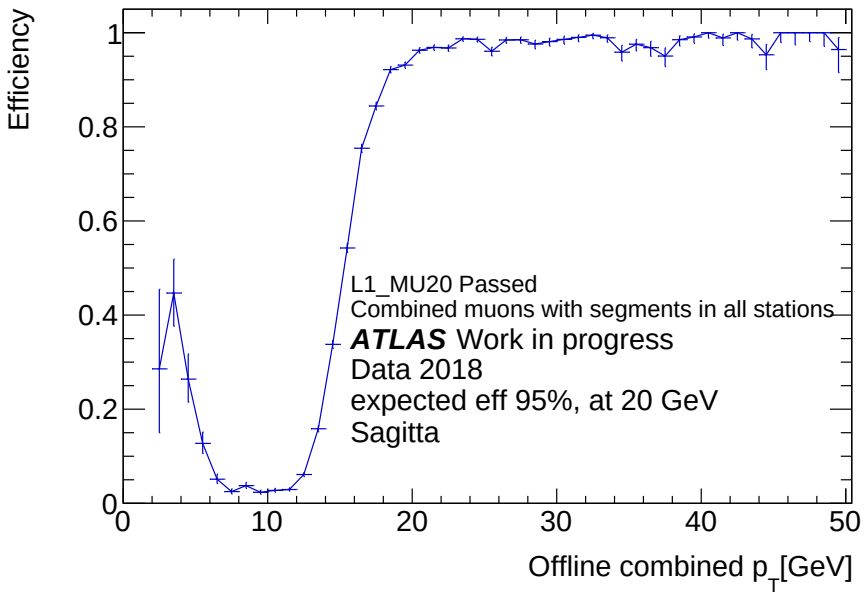

Fig. 5.6 Turn-on curve with only parameter sagitta (s) using the real data sample.

5.2.4 Combined Results with ATLAS Run 2 Dataset

The combined result of the performance test of muon selection ability with the real data sample is shown in Fig. 5.6. The shape of the turn-on curve is similar to the results with the $Z \to \mu\mu$ test sample described in the previous chapter. The acquisition efficiency of muons in the region of offline combined $p_{\mathrm{T}} > 20$ GeV is 97.2%. With the effect from the misalignment of detectors, the coarse granularity of RoIs issued by the Run 2 RPC trigger, and the contamination of fake muons, the rise of acquisition efficiency in the low-p_{T} region is more obvious.

The component of the RoIs matched with offline combined muons are shown in Fig. 5.8. Compared with the components of the Monte Carlo test samples, the ratio of muons matched with only one segment or no segment is very small and s, and parameter β can be calculated for most of the muons for trigger decision. Hence the inefficiency observed in the region of offline combined $p_{\mathrm{T}} > 20$ GeV comes from the inefficiency described in Appendix B.

In summary, with the real data sample, the AM-MDT muon trigger still has a good muon selection ability, and high acquisition efficiency is achieved for the muons with offline combined $p_{\mathrm{T}} > 20$ GeV. The effects of the coarse granularity of the RoIs issued by the Run 2 RPC trigger, the misalignment of detectors and the contamination of fake muons are observed, but the effects do not impact the performance of muon selection much. The results show that the current algorithm of AM-MDT muon trigger is robust to pileups and also the misalignment of detectors. Further optimisation of the matching conditions between the RoIs and reconstructed segments and the introduction of corrections on the misalignment are important for the improvement of the muon selection performance of AM-MDT muon trigger.

5.3 Trigger Rate Reduction at p_{T} threshold of 20 GeV

The performance studies described in this section use the same data sample as Sec. 5.2. Fig. 5.9 shows the $p_{\mathrm{T}}^{\mathrm{IP}}$ distribution associated with the RoIs before and after the AM-MDT muon trigger. Only RoIs that matched with offline combined muons are shown. The distribution is consistent

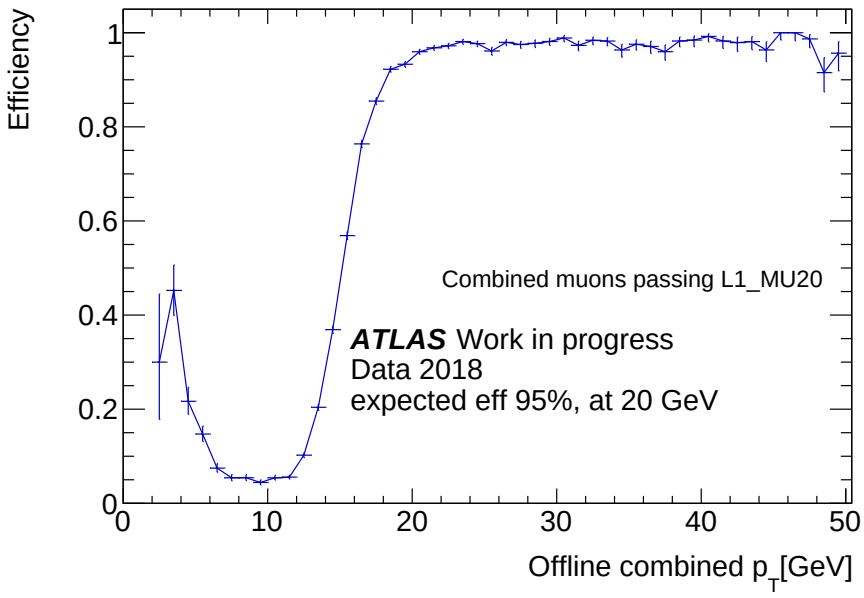

Fig. 5.7 Combined performance using the online algorithm with prioritised parameters in the real data sample.

with the results of the performance tests of muon selection. The muons discarded by the AM-MDT muon trigger are mainly in the region of offline combined $p_{\mathrm{T}} < 17$ GeV. In the region of offline combined $p_{\mathrm{T}} < 5$ GeV, the muons that make the rise of acquisition efficiency can be confirmed. Since no HLT algorithm was applied for the selection of the events, the total entries of the two distributions are corresponding to the trigger rate fired by muon candidates before and after the AM-MDT muon trigger. By comparing the two components, we can find that the AM-MDT muon trigger strongly suppresses the triggers fired by the muon candidates with offline combined $p_{\mathrm{T}} < 20$ GeV.

Other than the RoIs included in the distributions shown in Fig. 5.9, the RoIs that did not match with an offline muon exist. Those RoIs are mainly from fake muons. Fot those fake muons, usually any valid parameter is calculated in the AM-MDT muon trigger. Thus the AM-MDT muon trigger is also able to reject these fake muons. The η distribution of all RoIs before and after the AM-MDT muon trigger is shown in Fig. 5.10. With the current algorithm of AM-MDT muon trigger under the environment of ATLAS Run 2, a rate reduction of 51.3% is achieved with respect to the Run 2 L1 muon trigger in the barrel region while keeping a 97.2% acquisition efficiency of muons with offline combined $p_{\mathrm{T}} > 20$ GeV.

The dependency on the number of pileups is also investigated, and the result is shown in Fig. 5.11. The performance of rate reduction ability of the AM-MDT muon trigger is stable in the range of the average number of pileups from about 20 to 55. If we focus on the region of offline combined p_{T} smaller than the p_{T} threshold, the rate reduction in this region is more than 60% and stable, and in the region of offline combined $p_{\mathrm{T}} < 15$ GeV, about 80% RoIs are successfully discarded. From the result, we can expect a stable and good performance on rate reduction even in the HL-LHC environment.

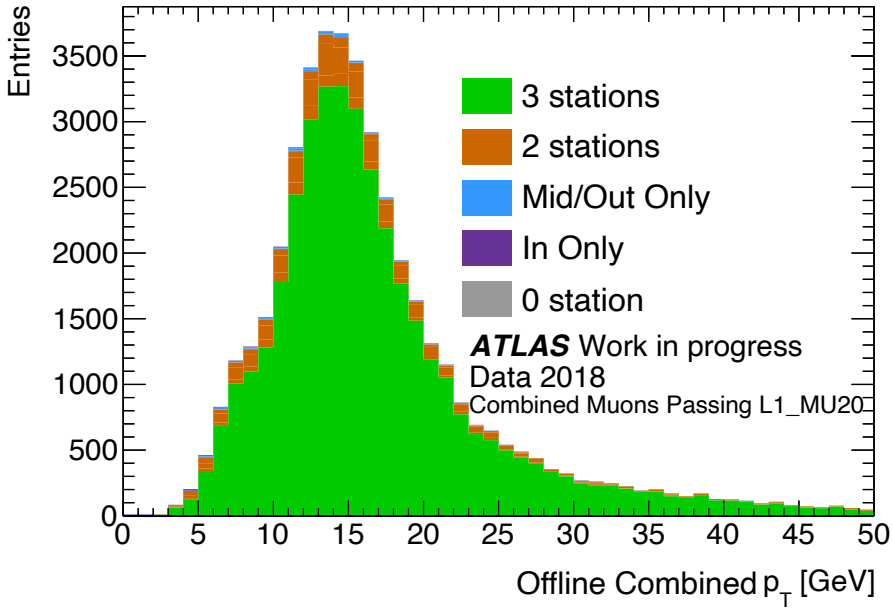

Fig. 5.8 Components of offline combined muons contained in the real data sample. The colour shows the number of AM reconstructed segments matched with the offline combined muons.

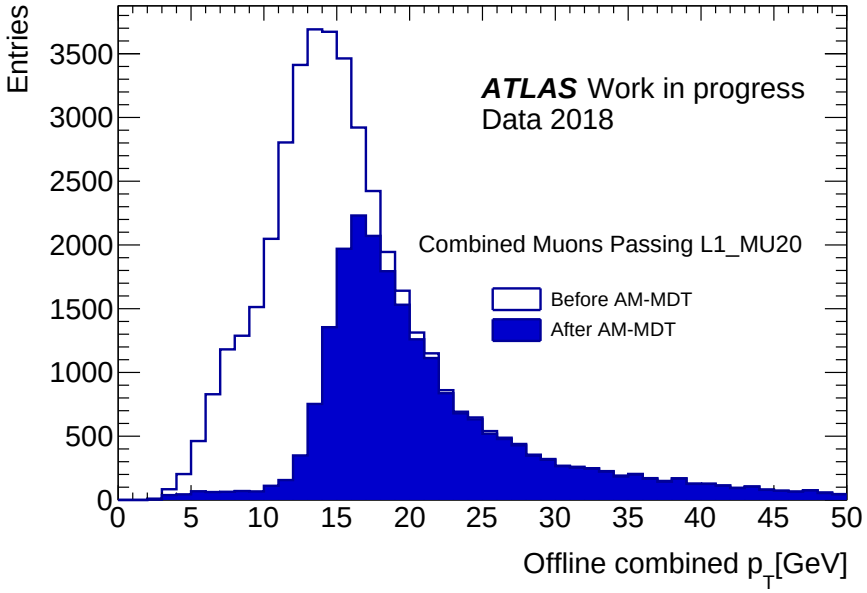

Fig. 5.9 Offline p_{T} distribution of the offline combined muons that are matched with the RoIs issued by the Run 2 RPC trigger. The white components are discarded by the AM-MDT muon trigger.

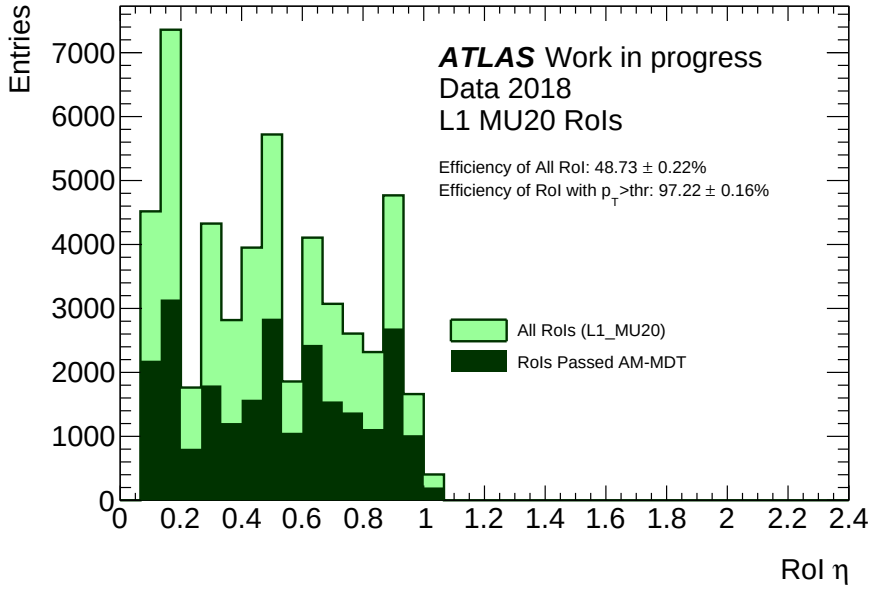

Fig. 5.10 η distribution of all RoIs contained in the real data sample. All the RoIs passed the Run 2 RPC trigger with p_{T} of 20 GeV. The RoIs that match with no offline combined muon are also included. The components that are discarded by the AM-MDT muon trigger are shown in light green.

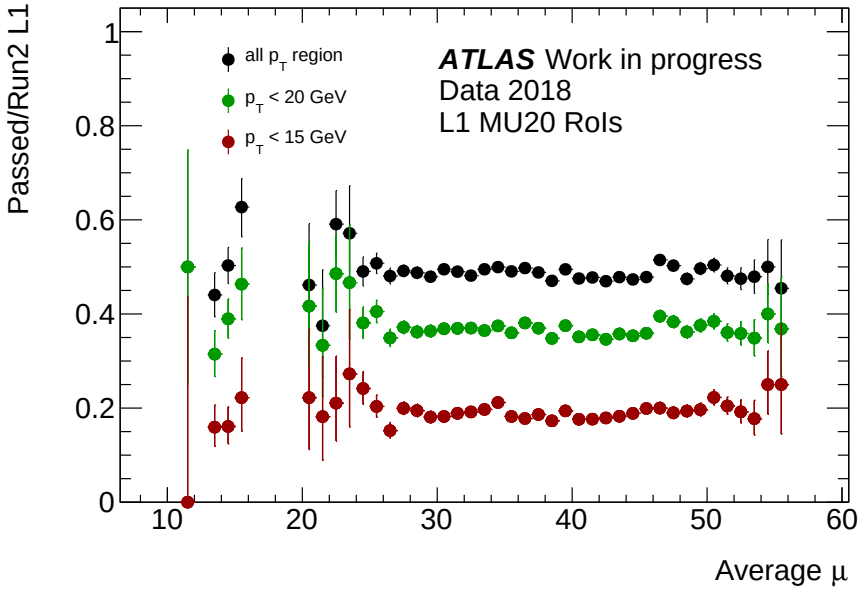

Fig. 5.11 Dependence on the number of pileups of the rate reduction performance. The ratio of how many RoIs passed the AM-MDT muon trigger is shown. The RoIs that match with no offline combined muon are included in the denominator and also in the numerator if the RoIs passed the AM-MDT muon trigger. The black dots show the total rate reduction, the green dots show the rate reduction in the region of offline combined $p_{\mathrm{T}} < 20$ GeV and the red dots show the rate reduction in the region of offline combined $p_{\mathrm{T}} < 15$ GeV.

5.4 Results with p_{T} threshold of 10 GeV

Performance tests of muon selection and rate reduction are also conducted for L1 p_{T} threshold of 10 GeV (L1_MU10) with the real data sample. Fig. 5.12 shows the result of the performance of muon selection ability. The acquisition efficiency in the region of $p_{\mathrm{T}} > 10$ GeV is 95.4%. The shape of the turn-on curve is steep, with a very small rise in the low-p_{T} region. The acquisition efficiency seems to be unstable in some of p_{T} regions. The main cause is the inefficiency described in Appendix B, with effects from statistic fluctuations due to only a small number of entries in the p_{T} regions, as shown in Fig. 5.13.

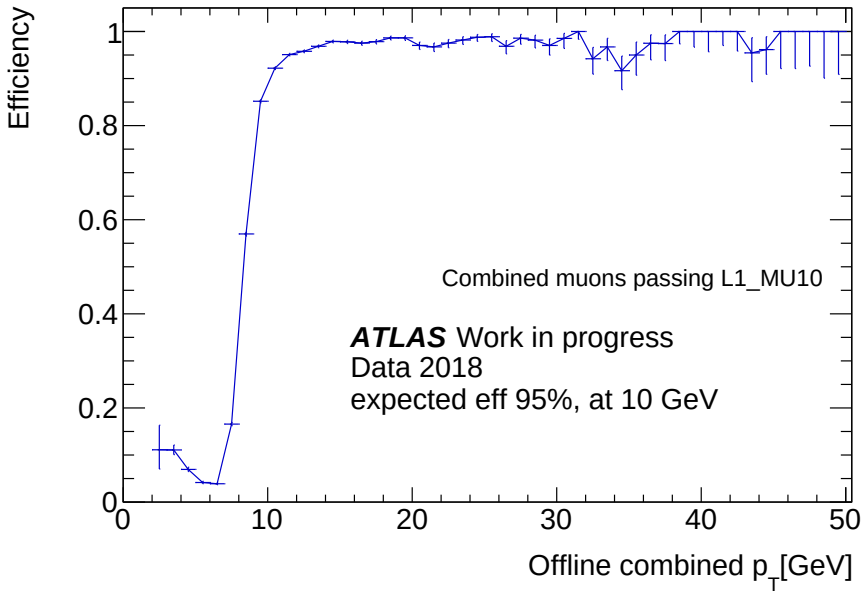

Fig. 5.12 Combined performance using the online algorithm with prioritised parameters using the real data sample for p_{T} threshold of 10 GeV.

The offline combined p_{T} distributions before and after the AM-MDT muon trigger for the case of p_{T} threshold of 10 GeV are shown in Fig. 5.13. Similar to the tests at p_{T} threshold of 20 GeV, triggers fired by the muon candidates with $p_{\mathrm{T}} < 10$ GeV are strongly suppressed. The test result of total rate reduction is shown in Fig. 5.14 and the dependence on the number of pileups is shown in Fig. 5.15. A total rate reduction of 40.0% is achieved in the case of p_{T} threshold of 10 GeV. For the RoIs with offline combined p_{T} smaller than 10 GeV and smaller than 7 GeV, about 45% of RoIs can be discarded by the AM-MDT muon trigger. The results of the two cases have very small difference because the number of RoIs that did not match an offline combined muon and assigned $p_{\mathrm{T}} = -1$ GeV is much larger than the number of muon candidates with 7 GeV $< p_{\mathrm{T}} <$ 10 GeV. Generally, the rate reduction performance with p_{T} threshold of 10 GeV is stable even when the number of pileups increases.

In conclusion, the performance tests with p_{T} threshold of 10 GeV using the real data samples, show that the AM-MDT muon trigger has high event selection ability and good performance of rate reduction.

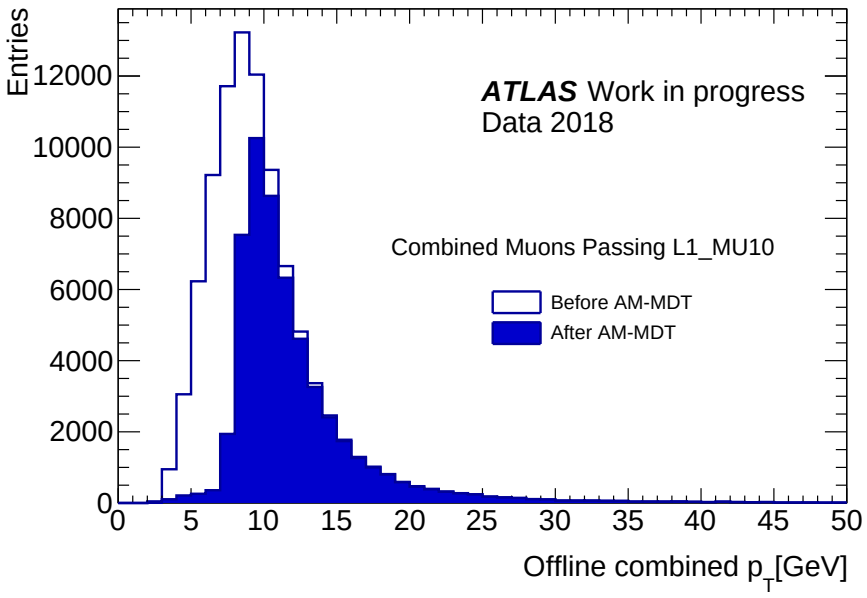

Fig. 5.13 Offline p_{T} distribution of the offline combined muons that are matched with the RoIs issued by the Run 2 RPC trigger for p_{T} threshold of 10 GeV. The white components are discarded by the AM-MDT muon trigger.

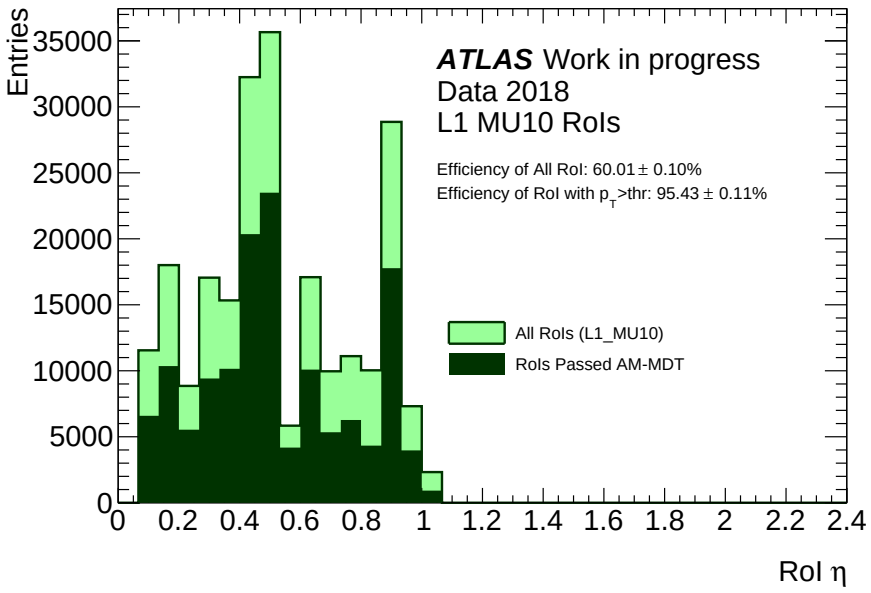

Fig. 5.14 η distribution of all RoIs contained in the real data sample. All the RoIs passed the Run 2 RPC trigger with p_{T} of 10 GeV. The RoIs that match with no offline combined muon are also included. The components of RoIs that are discarded by the AM-MDT muon trigger are shown in light green.

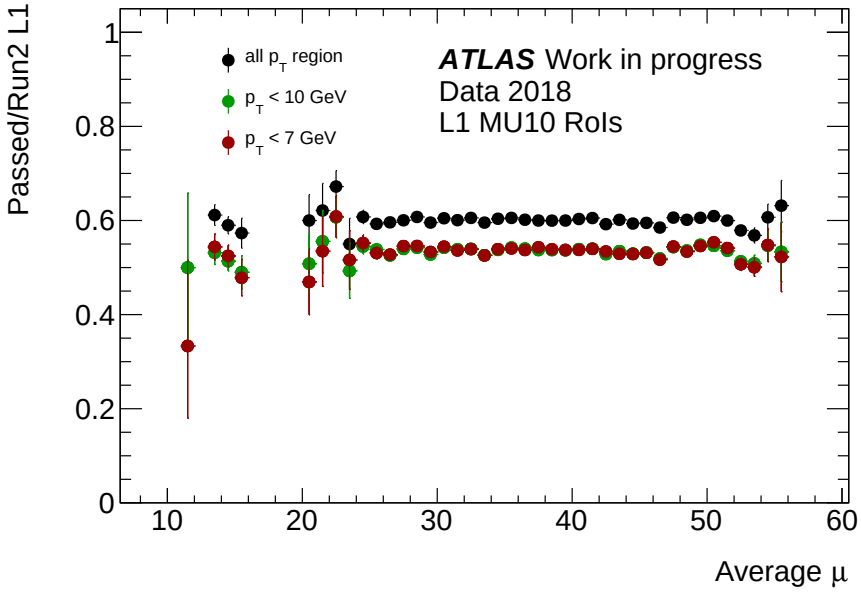

Fig. 5.15 Dependence on the number of pileups of the rate reduction performance for p_{T} threshold of 10 GeV. The ratio of how many RoIs passed the AM-MDT muon trigger is shown. The RoIs that match with no offline combined muon are included in the denominator and also in the numerator if the RoIs passed the AM-MDT muon trigger. The black dots show the total rate reduction, the green dots show the rate reduction in the region of offline combined $p_{\mathrm{T}} < 10$ GeV and the red dots show the rate reduction in the region of offline combined $p_{\mathrm{T}} < 7$ GeV.

Chapter 6

Conclusions and Outlook

To search for new physics phenomena, CERN approved to upgrade the LHC to the HL-LHC. The high-luminosity environment after the upgrade results in more particles produced by the pileup collisions. Thus the trigger system of the ATLAS experiment will face a more challenging situation to select the event related to the target new physics processes. In the case of muon trigger system, new muon trigger that has excellent p_{T} resolution and good rate reduction ability is needed to maintain high acceptance to the new physics related events. Hence the introduction of a new muon trigger using the information of the MDT detector is proposed.

The MDT detector can provide precise information of position and direction of the segments of muon trajectories. The information of the MDT detector is now used for software-based triggers only. ATLAS Japan group proposes to use a design based on Associative Memory to realise the MDT muon trigger. The AM-MDT muon trigger uses the AMChips to reconstruct muon segments with a pattern recognition technology and then calculates parameters (α, β, and sagitta s) that are related to the muon p_{T} for muon selection on the FPGA. We developed online algorithms, including all steps after the segment reconstruction in the AMChips by matching input data with pre-stored patterns. In the online algorithm, conditions for matching between the RoIs and reconstructed segments are set, and the calculation of parameters used for muon selection is performed. The conversion from the calculated parameters to an estimated p_{T} is also implemented.

We tested the online algorithm with full chain software emulation using Monte Carlo test samples and real data samples. The emulation of pattern matching in the AMChips was done with prepared bank files. The thresholds of the parameters are trained using single muon particle gun simulation samples. With the results using Monte Carlo test samples, we confirmed that all three types of parameters have the ability to select muon by p_{T}, and the performance is maintained under the toughest environment of the HL-LHC. Especially for the parameter sagitta (s), the p_{T} resolution and ability of muon selection are not affected at all. The p_{T} resolution of sagitta (s) is stable at a level of about 10% in the high-luminosity environment. With the real data sample and by using an algorithm with parameters prioritised, in the ATLAS barrel region, the AM-MDT muon trigger can discard 51.3% of trigger rates while maintaining a 97.2% acquisition efficiency of the muons with $p_{\mathrm{T}} > 20$ GeV. In the case of p_{T} threshold of 10 GeV, the AM-MDT muon trigger can discard 40.0% of total rates while maintaining a 95.4% acquisition efficiency of the muons with p_{T} larger than the threshold. The performance of rate reduction also confirmed the stability against the increase of luminosity. In conclusion, the results show that AM-MDT muon trigger has excellent ability of muon selection and rate reduction. The good performances even can be expected under the HL-LHC environment.

As discussed in Chapter 5, further optimisations of matching conditions and implementation of the correction for mis-alignment of detectors can help to achieve better performance of muon selection. If we compare the results with the estimated performance given by the TDAQ TDR of Phase-II upgrade, the performance of rate reduction still has a gap of about 15% to 20%. This fact indicates that rooms for the improvement of the current online algorithm still exist.

In the future, the final optimisations of the online algorithm is expected to finish up the design of AM-MDT muon trigger. Hardware-based implementation of the developed online algorithm is also necessary for the demonstration at the ATLAS technology selection meeting in 2020. If the AM-MDT muon trigger is selected, the production and tests of the prototype AM-MDT muon trigger will start soon. Finally, the AM-MDT muon trigger will be incorporated to the muon trigger system in the LS3.

A

The Performance of Segment Reconstruction with Associative Memory

The performance test of segment reconstruction is using a Monte Carlo sample that reproduces the environment of the HL-LHC with banks described in Table 3.2. The sample contains $Z \to \mu\mu$ events with 200 pileups and 25 cavern backgrounds.

The efficiency of reconstruction is defined with respect to good offline segments that are associated with an offline combined muon. The good offline segments have at least 4 MDT hits in the Middle Station or the Outer Station and at least 5 MDT hits in the Inner Station. The reconstructed muons are required to pass at least four-out-of-six hits in the patterns.

The angular resolution and the spatial resolution are inclusively calculated with outputs of AM Chips which require a full match, a five-out-of-six match and a four-out-of-six match. The residual distribution is assumed to be a gaussian distribution and fitted. In the fitting, the tail component is neglected, and the fitting areas are set to $[-0.05, 0.05]$ mrad and $[-1.0, 1.0]$ mm respectively.

The results of the reconstruction efficiency are shown in Fig. A.1. The results of the angular resolution and the spatial resolution are shown in Fig. A.2 and Fig. A.3, respectively.

In Fig. A.1, the reconstruction efficiencies in the Inner Stations are relatively lower than the Middle and the Outer Stations, the average efficiencies are higher than 95% though. The origin of the relatively low efficiency may be the potentially insufficient number of patterns in the small sectors, and also can be the effect of the high luminosity environment. The difference in the efficiencies of the Inner Station and the Middle/Outer Stations can be explained by the difference of distance to the IP. The Inner Station is easier to be affected by the pileup particles. However, smaller size of pattern banks of small sectors also should be seen in the case of the Middle Station, further investigations are needed to understand the inefficiency. The structure of the barrel MDT detectors can also be confirmed. The regions that are not covered by the MDT detectors have low efficiencies.

Fig. A.2 and Fig. A.3 also show the component of matched patterns. More than half of the segments have full matched patterns and most of the segments can find a pattern with five-out-of-six match. With the four-out-of-six match, almost all segments can find a pattern in the AM Chips and be reconstructed.

When a segment is matched with multi patterns, the pattern that gives minimum $\Delta\theta$ or Δz is used to draw the residual distributions. In other words, the residual distributions show the case of best performance. Since all the matched patterns will be passed to muon track reconstruction step, the best performance is possible to be achieved by introducing a segment selection algorithm.

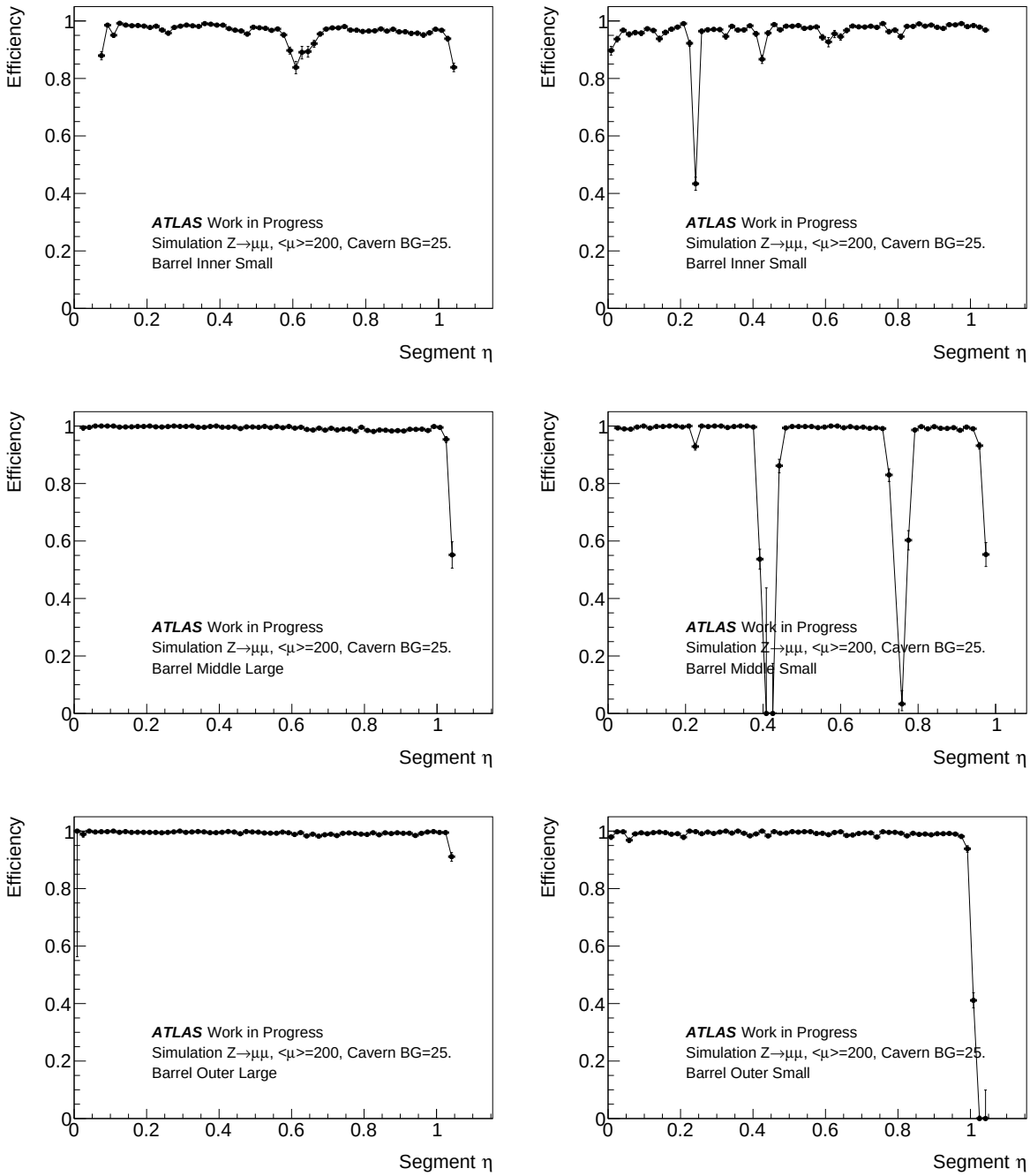

Fig. A.1 The reconstruction efficiency of muon segments in each station against the good offline segments. Inclusive results of all sectors exclude the special sectors of Barrel A-side. The reconstructed segments are required to match at least four-out-of-six hits.

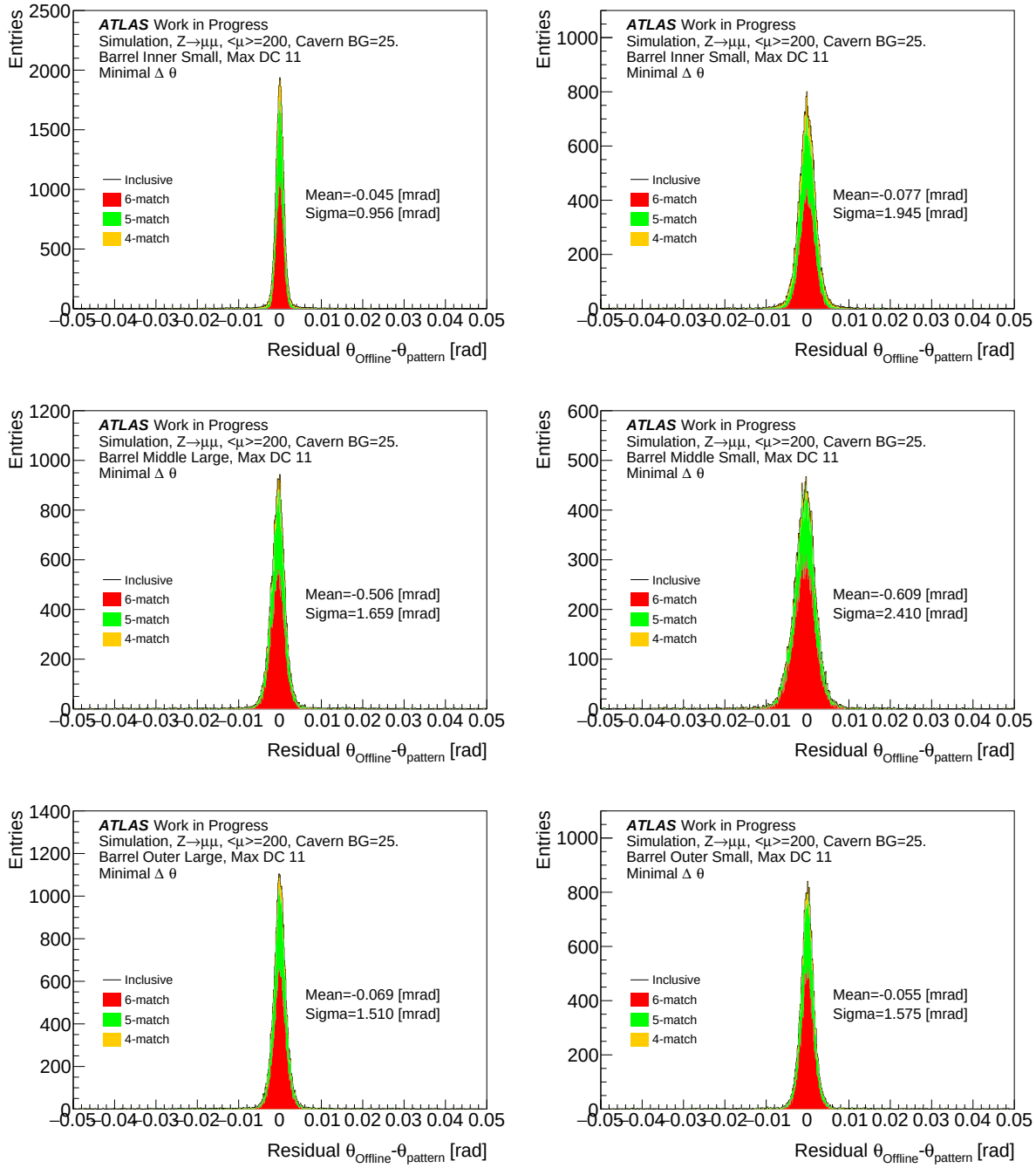

Fig. A.2 Angular resolution of muon segments in each station. Inclusive results of all sectors exclude the special sectors of Barrel A-side. The black line shows the inclusive distribution of segments passed the six-out-of-six match, five-out-of-six match and four-out-of-six match.

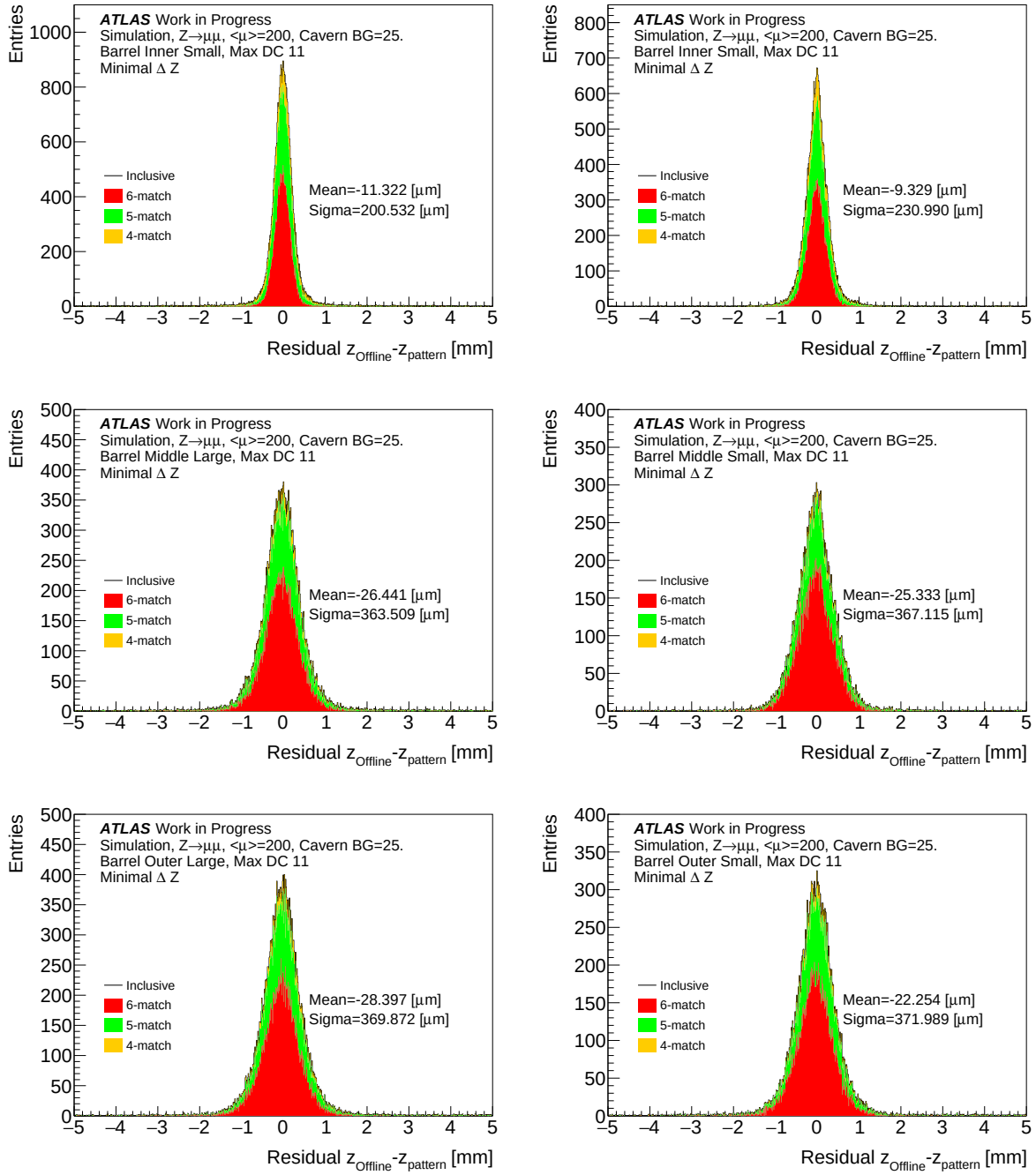

Fig. A.3 Spatial resolution of muon segments in each station. Inclusive results of all sectors exclude the special sectors of Barrel A-side.

B

Inefficiency in the High-p_{T} Region

The inefficiency of muon acquisition observed of high-p_{T} is an inefficiency caused by the condition of the performance test. From conclusion, the muons with high offline combined p_{T} discarded by the AM-MDT muon trigger are probably not muons produced in the proton-proton collisions but fake muons such as a strong hadron jet punches through the Calorimeter.

The muons in the samples used for tests are reconstructed with the offline reconstruction algorithms by a reproduction after the data taking. Muons that are successfully reconstructed by combining the information of the ID, the Calorimeter and the MS are called offline combined muons. The offline combined p_{T} and the offline muon spectrometer p_{T} are both calculated in the reconstruction. The muons are also evaluated by many conditions and given a tag of muon quality. Four levels of muon quality, Tight, Medium, Loose and Very Loose are defined by different conditions, for example the number of hits in the MDT detectors [49]. In the performance tests described in Chapter 4 and Chapter 5, all the offline combined muons in the samples are used. In the case of the Monte Carlo samples, most of the offline combined muons have a quality better than Medium. However, in the case of the real data sample, the ratio of offline combined muons with low qualities is much higher than the Monte Carlo samples. Fig. B.1 shows the relation between the offline combined p_{T} and the offline muon spectrometer p_{T}. From Fig. B.1 (a), we can find that most of the muons have similar offline combined p_{T} and offline muon spectrometer p_{T}[*1], but in the low offline muon spectrometer p_{T} region, many offline combined muons have a much larger offline combined p_{T} compared to their offline muon spectrometer p_{T}. Since the developed online algorithm of the AM-MDT muon trigger converts the parameters to an estimated muon spectrometer $p_{\mathrm{T}}^{\mathrm{MS}}$, the $p_{\mathrm{T}}^{\mathrm{IP}}$s of these muons are much smaller than their actual offline combined p_{T}. As a result, these muons are discarded by the AM-MDT muon trigger and an inefficiency is observed. If we require that the offline combined muons should have a quality better than Medium, the distribution changed, as shown in Fig. B.1 (b). The muons with largely deviated offline combined p_{T} and offline muon spectrometer p_{T} disappear and only the linear component in the central remains.

To check the scale of impacts of the component causing the inefficiency, we drew turn-on curves against the offline combined p_{T} with a cut of the offline muon spectrometer p_{T}, as shown in Fig. B.2. The denominators are the offline combined muons shown in Fig. B.1 (a), (b) respectively, and the numerators are offline combined muons meeting the condition of offline muon spectrometer $p_{\mathrm{T}} + 2.77 > 15$ GeV. No online algorithm for p_{T} estimation is applied and the offline information is directly used. By comparing the two turn-on curves shown in Fig. B.2, the inefficiency is about 5% to 10% depending on the offline combined p_{T}, and if Medium quality of muon is required, the inefficiency disappears.

In the results of performance test with the real data sample, the observed inefficiency is about 2.5% which is smaller than the scale shown in Fig. B.2. This difference possibly comes from the accidentally matched segments created by the pileups as discussed in Chapter 4. The low-

[*1] The difference is almost constant, 2.77 GeV, as described in Chapter 3.

qualities muons in the real data sample accidentally passed the threshold just as the muons caused the rise of acquisition efficiency in the low-p_{T} region. By checking the details of low-quality muons with other data samples, they are probably fake muons from a high-energy hadron jet punching through the calorimeter and reaching the muon spectrometer. A simple image of the punch-through event is shown in Fig. B.3. High-p_{T} charged hadron leaves a high-p_{T} track in the ID. Then in the Hadron Calo, the hadron creates a hadron shower. If the energy of the hadron is high enough, that the Hadron Calo can not absorb the energy of all the shower particles, some of the particles produced in the shower may go through the Hadron Calo and reach the MS. In the particles, low-p_{T} muons probably exist and thus give a small p_{T} in the MS. Consequently, the offline MS p_{T} is much smaller than the offline combined p_{T} for these muons.

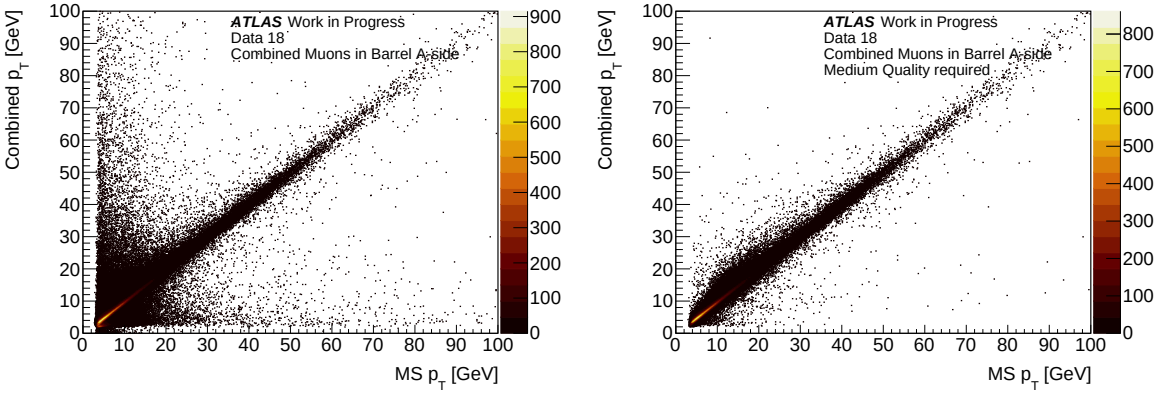

(a) (b)

Fig. B.1 Distributions of the offline combined p_{T} and the offline muon spectrometer p_{T}, without (a) and with (b) the requirement on muon quality. The offline muon spectrometer p_{T} shown in the figure is shifted by 2.77 GeV.

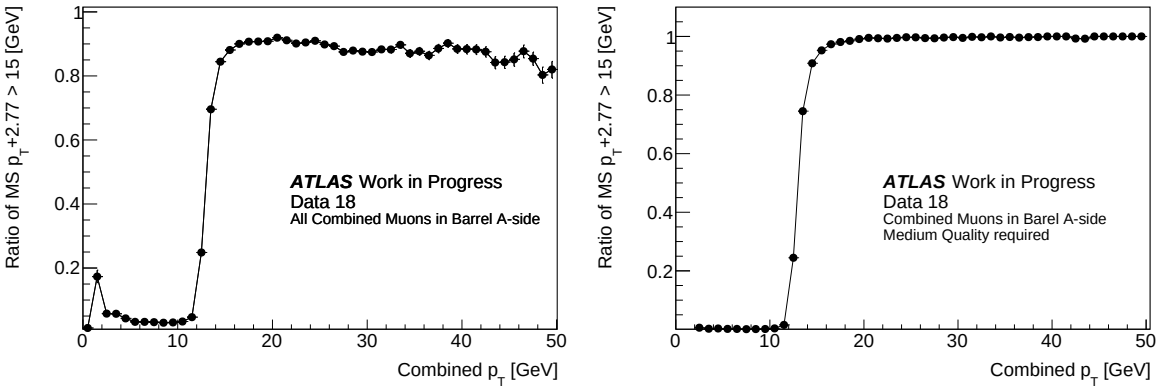

(a) (b)

Fig. B.2 Turn-on curves with cut on offline muon spectrometer p_{T} drawn against offline combined p_{T}. The left (a) one is drawn with all combined muons in the real data sample and the right (b) with a requirement on muon quality.

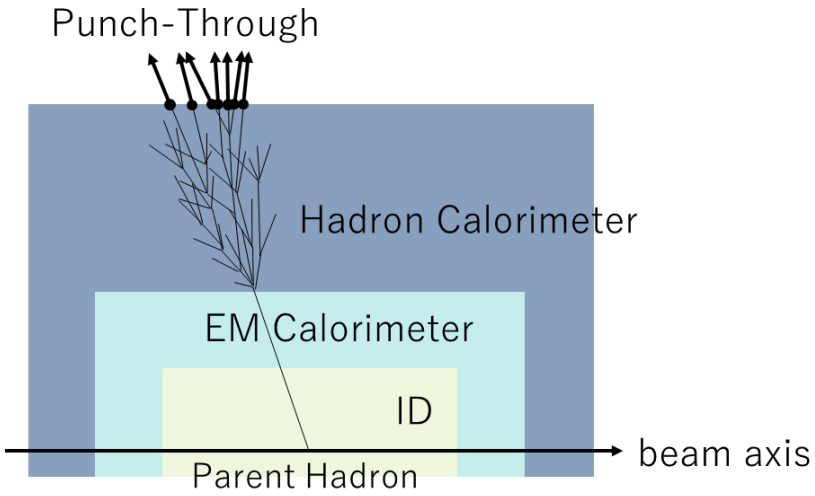

Fig. B.3 An image figure of the puch-through of a hadron jet.

Bibliography

[1] J. J. Thomson, Xl. cathode rays, *Lond.Edinb.Dubl.Phil.Mag.*, Vol. 44, No. 269, pp. 293–316, 1897.

[2] A. Purcell, Go on a particle quest at the first CERN webfest, No. BUL-NA-2012-269, p. 10, 2012.

[3] Y. Fukuda, et al., Evidence for oscillation of atmospheric neutrinos, *Phys. Rev. Lett.*, Vol. 81, pp. 1562–1567, 1998.

[4] Q. R. Ahmad, et al., Measurement of the rate of $\nu_e + d \to p + p + e^-$ interactions produced by ^8B solar neutrinos at the Sudbury Neutrino Observatory, *Phys. Rev. Lett.*, Vol. 87, p. 071301, 2001.

[5] Z. Maki, M. Nakagawa, and S. Sakata, Remarks on the Unified Model of Elementary Particles, *Prog. Theor. Phys.*, Vol. 28, No. 5, pp. 870–880, 1962.

[6] ATLAS Collaboration, Observation of a new particle in the search for the Standard Model Higgs boson with the ATLAS detector at the LHC, *Phys. Lett.*, Vol. B716, pp. 1–29, 2012.

[7] CMS Collaboration, Observation of a New Boson at a Mass of 125 GeV with the CMS Experiment at the LHC, *Phys. Lett.*, Vol. B716, pp. 30–61, 2012.

[8] G. Aad, et al., Measurements of the Higgs boson production and decay rates and constraints on its couplings from a combined ATLAS and CMS analysis of the LHC pp collision data at $\sqrt{s} = 7$ and 8 TeV, *JHEP*, Vol. 08, p. 045, 2016.

[9] N. Aghanim, et al., Planck 2018 results. VI. Cosmological parameters, 2018.

[10] J. Ellis, Higgs Physics, No. CERN-PH-TH-2013-315, pp. 117–168, 2013.

[11] Yu. A. Golfand and E. P. Likhtman, Extension of the Algebra of Poincare Group Generators and Violation of p Invariance, *JETP Lett.*, Vol. 13, pp. 323–326, 1971.

[12] D.V. Volkov and V.P. Akulov, Is the neutrino a goldstone particle?, *Phys. Lett. B*, Vol. 46, No. 1, pp. 109 – 110, 1973.

[13] J. Wess and B. Zumino, Supergauge transformations in four dimensions, *Nucl. Phys. B*, Vol. 70, No. 1, pp. 39 – 50, 1974.

[14] J. Wess and B. Zumino, Supergauge invariant extension of quantum electrodynamics, *Nucl. Phys. B*, Vol. 78, No. 1, pp. 1 – 13, 1974.

[15] S. Ferrara and B. Zumino, Supergauge invariant yang-mills theories, *Nucl. Phys. B*, Vol. 79, No. 3, pp. 413 – 421, 1974.

[16] A. Salam and J. Strathdee, Super-symmetry and non-abelian gauges, *Phys. Lett. B*, Vol. 51, No. 4, pp. 353 – 355, 1974.

[17] S. P. Martin, A Supersymmetry primer, *Adv. Ser. Direct. High Energy Phys.*, Vol. 18, pp. 1–98, 1997.

[18] G. R. Farrar and P. Fayet, Phenomenology of the production, decay, and detection of new hadronic states associated with supersymmetry, *Phys. Lett. B*, Vol. 76, No. 5, pp. 575 – 579, 1978.

[19] H. Goldberg, Constraint on the photino mass from cosmology, *Phys. Rev. Lett.*, Vol. 50, pp. 1419–1422, 1983.

[20] J. Ellis, J.S. Hagelin, D.V. Nanopoulos, K. Olive, and M. Srednicki, Supersymmetric relics from the big bang, *Nucl. Phys. B*, Vol. 238, No. 2, pp. 453 – 476, 1984.

[21] H. K. Dreiner, An Introduction to explicit R-parity violation, *Adv. Ser. Direct. High Energy*

Phys., Vol. 21, pp. 462–479, 1997.
[22] R. Barbier, et al., R-parity violating supersymmetry, *Phys. Rept.*, Vol. 420, pp. 1–202, 2005.
[23] SUSY October 2019 Summary Plot Update, Technical Report ATL-PHYS-PUB-2019-044, CERN, 2019.
[24] G. Aad, et al., ATLAS data quality operations and performance for 2015-2018 data-taking, Technical report, CERN, 2019.
[25] ATLAS Collaboration, Technical Design Report for the Phase-II Upgrade of the ATLAS TDAQ System, Technical Report ATLAS-TDR-029, CERN, 2017.
[26] N. Arkani-Hamed, A. Delgado, and G.F. Giudice, The well-tempered neutralino, *Nucl. Phys. B*, Vol. 741, No. 1, pp. 108 – 130, 2006.
[27] K. Ntekas, et al., Fast track segment finding in the Monitored Drift Tubes of the ATLAS Muon Spectrometer using a Legendre transform algorithm, Technical Report ATL-DAQ-PROC-2018-008, CERN, 2018.
[28] P. P. Gadow, Development of a Concept for the Muon Trigger of the ATLAS Detector at the HL-LHC, Master's thesis, TUM, 2016.
[29] S. Kawaguchi, 高輝度 LHC に向けた ATLAS 実験における新しいミューオントリガーの開発, Master's thesis, Tokyo Tech, 2018.
[30] Y. He, 高輝度 LHC の ATLAS 実験に向けた MDT ミューオントリガーの開発, Bachelor's Thesis, Toko Tech, 2018.
[31] E. Mobs, The CERN accelerator complex - 2019., 2019, General Photo.
[32] The High-Lumi LHC Project, Hl-lhc-plan-2019-plan-1, 2019.
[33] G. Aad, et al., The ATLAS Experiment at the CERN Large Hadron Collider, *JINST*, Vol. 3, p. S08003, 2008.
[34] J. Pequenao, Event Cross Section in a computer generated image of the ATLAS detector., 2008.
[35] M. Schott and M. Dunford, Review of single vector boson production in pp collisions at $\sqrt{s} = 7$ TeV, *Eur. Phys. J.*, Vol. C74, p. 2916, 2014.
[36] J.J. Goodson, *Search for Supersymmetry in States with Large Missing Transverse Momentum and Three Leptons including a Z-Boson*, PhD thesis, Stony Brook University, 2012.
[37] T Kawamoto, ATLAS : status, limitations and upgrade plans, 2011.
[38] A. Ruiz-Martinez and ATLAS Collaboration, The Run-2 ATLAS Trigger System, Technical Report ATL-DAQ-PROC-2016-003, CERN, 2016.
[39] Y. Noguchi, LHC-ATLAS 実験のミューオントリガーにおける飛跡再構成アルゴリズムの改良, Master's thesis, Kyoto University, 2017.
[40] T. Kawamoto, et al., New Small Wheel Technical Design Report, Technical Report ATLAS-TDR-020, 2013, ATLAS New Small Wheel Technical Design Report.
[41] Marco Vanadia, Study of the performance of the micromegas chambers for the atlas muon spectrometer upgrade, *IEEE Trans. Nucl. Sci.*, Vol. 64, pp. 867–873, 2017.
[42] A. Abusleme, et al., Performance of a full-size small-strip thin gap chamber prototype for the atlas new small wheel muon upgrade, *Nucl. Instrum. Methods Phys. Res. A*, Vol. 817, pp. 85 – 92, 2016.
[43] G. Aad, et al., Technical Design Report for the Phase-I Upgrade of the ATLAS TDAQ System, Technical Report ATLAS-TDR-023, 2013.
[44] ATLAS Collaboration, Technical Design Report for the Phase-II Upgrade of the ATLAS Muon Spectrometer, Technical Report ATLAS-TDR-026, CERN, 2017.
[45] S.R. Amendolia, S. Galeotti, F. Morsani, D. Passuello, L. Ristori, and N. Turini, The amchip: a vlsi associative memory for track finding, *Nucl. Instrum. Methods Phys. Res. A*, Vol. 315, No. 1, pp. 446 – 448, 1992.
[46] A. Stabile, et al., Phase-II Associative Memory ASIC Specifications, Technical Report CERN-OPEN-2018-003, INFN, CERN; LPNHE; University, 2018.

[47] C. Gentsos, et al., Track finding mezzanine for Level-1 triggering in HL-LHC experiments, p. 4, 2017.
[48] Y. Okumura, et al., Specification note: Associative Memory application for L0 MDT trigger, Internal note under preparation.
[49] G. Aad, et al., Muon reconstruction performance of the ATLAS detector in proton - proton collision data at $\sqrt{s}$ =13 TeV, *Eur. Phys. J.*, Vol. C76, No. 5, p. 292, 2016.

Acknowledgements

First of all, I would like to express my gratitude to my supervisor, Prof. Masahiro Kuze. He provided me with the opportunity to join the ATLAS experiment and to get involved with the project of the AM-MDT muon trigger. Without his helpful advice on my research and strong support from all degrees, this study could not be conducted so smoothly. I learnt a lot from Prof. Kuze, not only the knowledge of particle physics and also the philosophy of life.

Then, I wish to thank Assoc. Prof. Yasuyuki Okumura and Assist. Prof. Yohei Yamaguchi, who directly supported the progress of my study. Assoc. Prof. Okumura managed the project of AM-MDT muon trigger. We exchanged ideas and opinions of the study at the group meeting during the development process. He also helped my life when I was travelling at CERN, especially for telling me the delicious Chinese restaurant in the city of Geneva. Assist. Prof. Yamaguchi supported me a lot in Tokyo. He noticed many crucial points of the study and offered me a lot of useful instructions to solve the difficulties found in the process. The daily chats and discussions in the laboratory of the Kuze Group with Assist. Prof. Yamaguchi also give me a lot of fun during the time of my master course.

I would like to thank Prof. Masaya Ishino. Prof. Ishino firmly supported the AM-MDT muon trigger project by giving lots of essential comments with his years of experience of the ALTAS trigger system. I also want to thank Assist. Prof. Yasuyuki Horii, who conducted parts of the previous research and in management of the Phase II upgrade meeting of ATLAS Japan. Much relevant information on the concept of the AM-MDT muon trigger was provided by Assist. Prof. Horii. Special thanks to Mr Takafumi Kodama for conducting the study of pattern matching performance in the AMchips and to Mr Yuya Mino for providing the training sample used in the study.

I am genuinely thankful to the other members of Kuze groups, Assist. Prof. Kenichi Nakano, Ms Tomoyo Yoshida, Mr Lukas Berns, Mr Yuuhi Fukuhara, Mr Shota Izumiyama, Mr Isao Sashima, Mr Shuhei Kanayama, and Mr Shunsuke Fujigami. They gave me a pleasant time in the laboratory.

Moreover, heartful gratitude to all the people whom I had a delightful time with. The experience in the time of my master course will be a lifetime treasure for me.

Last, I want to express my sincere thanks to my parents, who have always encouraged me with their deepest loves. I have no return at this time for their selfless support over the years, but I hope one day I can do so.

List of Figures

List of Tables